Diss. ETH No. 17902

ADVANCES IN WHOLE-HEART MRI TAGGING FOR THE ASSESSMENT OF MYOCARDIAL MOTION

A dissertation submitted to the
SWISS FEDERAL INSTITUTE OF TECHNOLOGY ZURICH
for the degree of
DOCTOR OF SCIENCES

presented by

Andrea K. Rutz
Dipl. El.-Ing. ETH
born March 14th, 1977
citizen of Teufen (AR), Switzerland

accepted on the recommendations of
Prof. Dr. Peter Bösiger, examiner
Prof. Dr. Matthias Stuber, co-examiner
PD. Dr. Sebastian Kozerke, co-examiner

Zurich 2008

Meinen Eltern gewidmet

Contents

Zusammenfassung

Die Quantifizierung kontraktiler Fehlfunktion des Herzens ist von grosser klinischer Bedeutung in Bezug auf Diagnose und verbesserte Behandlung verschiedener kardiovaskulärer Erkrankungen. Mit der Bestimmung regionaler Herzwandbewegung können wertvolle Erkenntnisse über die Herzmechanik in Gesunden und in Patienten gewonnen werden. Änderungen kardialer Bewegungsmuster sind in vielen Fällen frühe und sensitive Merkmale einer Herzerkrankung. Die Magnetresonanzbildbebung (MRI) bietet die Möglichkeit, Herzanatomie und –funktion nicht-invasiv zu messen, ohne dabei den Patienten ionisierender Strahlung auszusetzen. MRI-Tagging ist eine Methode, um regionale Herzbewegung genau und schnell zu quantifizieren. Mittels Tagging wird die Gewebemagnetisierung vor der Bildaufnahme moduliert. Die daraus resultierenden Linien- oder Gittermuster bewegen sich mit dem dazugehörigen Gewebe mit, wodurch eine Quantifizierung der Herzbewebung ermöglicht wird. Studien haben das herausragende Potential dieser Technik in der vorklinischen Herzforschung unter Beweis gestellt.

Ziel der vorliegenden Arbeit war die Entwicklung und Anwendung beschleunigter MRI Tagging-Aufnahme- und Auswertetechniken zur Charakterisierung regionaler Herzwandbewegung im gesunden und erkrankten Zustand.

Für die Aufnahme und Auswertung von Tagging-Daten steht eine Vielzahl unterschiedlicher Techniken bereit, wobei viele Verfahren sehr ähnliche Ansätze verfolgen. Vorteile der verschiedenen Methoden und deren optimale Anwendung in der Praxis wurden in dieser Arbeit evaluiert.

Die komplexe dreidimensionale Bewegung der Herzwand erfordert eine vollständige Abdeckung des Herzens in der Bildgebung sowie die Messung dreidimensionaler Bewegungstrajektorien. Diesbezüglich wurde ein neues Tagging-Aufnahmeverfahren entwickelt, mit dessen Hilfe die Aufnahme dreidimensionaler, bewegungskodierter Daten in schneller und effizienter Weise möglich ist. Die dazu benutzte Tagging-Technik kompensiert das Verblassen der Tags über die Zeit durch die Aufnahme zweier komplementärer Datensätze, welche voneinander subtrahiert werden (Complementary Spatial Modulation of

Magnetization, CSPAMM). Für die Akquisition der dreidimensionalen Tagging-Daten wurden drei Datensätze aufgenommen, welche je in eine Raumrichtung bewegungskodiert wurden. Die Aufnahmezeit konnte deutlich verringert werden, indem die Tagging-Modulation selektiv implementiert wurde, was eine Verkleinerung des abgebildeten Volumens auf die Grösse des Herzens ermöglichte. Zusätzlich wurde eine schnelle, segmentierte Echo-Planar MRI-Sequenz mit mehreren RF-Anregungen pro Herzphase verwendet. Für die Datenauswertung dreidimensionaler Tagging-Daten wurde eine existierende Technik, die sich in früheren Studien als schnell und zuverlässig erwiesen hat, erweitert.

Im Rahmen dieser Arbeit wurden neben dreidimensionalen Tagging-Techniken auch konventionelle, zweidimensionale Methoden weiterentwickelt und in gesunden Probanden und Patienten mit unterschiedlichen Herzkrankheiten angewendet. Neue Strategien wurden entwickelt, um die Herzbewegung mittels aussagekräftigen Parametern zu quantifizieren. Die in den Patientenstudien entwickelten Methoden erlauben auch, Schlüsse für individuell notwendige Therapien zu ziehen.

Die entwickelten Methoden erlaubten die Anwendung von drei- und zweidimensionalen Tagging-Techniken in grösseren Patientenstudien. Zweidimensionale Tagging-Verfahren wurden optimiert, um die Herzbewegung in Patienten mit Morbus Fabry zu messen. Morbus Fabry ist eine seltene, vererbbare Stoffwechselkrankheit, welche eine Vielzahl von Organen betrifft und auch eine schwere Veränderung des Herzens bewirkt, welche mit dem Alter fortschreitet und zum Tode führen kann. Eine Schichtverfolgungstechnik kam zum Einsatz, um Gewebebewegung durch die abgebildete Schicht zu eliminieren. Um den gesamten linken Ventrikel abzudecken, wurden mehrere Schichten in unterschiedlichen Orientierungen aufgenommen. Veränderungen in der Herzbewegung konnten nicht nur in Patienten mit makroskopischen Pathologien der Herzanatomie nachgewiesen werden, sondern auch in Patienten, welche nur frühe Anzeichen einer Herzkrankheit zeigten. Während sowohl die zirkumferentielle Kontraktion als auch die Verkürzung in Längsachsen-Richtung erst in Patienten mit hypertrophen Herzen verändert war, konnten für die apikale Rotation sowie die linksventrikuläre Torsion bereits im frühen Krankheitsstadium signifikante Veränderungen gemessen werden.

Die dreidimensionale Tagging-Technik wurde erstmals in einer grösseren Studie angewendet. In dieser Studie wurde die linksventrikuläre Kontraktion und Dissynchronie in Patienten mit Linksschenkelblock (Erregungsleitungsstörung) und in Patienten kurz nach erfolgtem Herzinfarkt gemessen. Eine Vielzahl von Herzbewegungsparametern wurde untersucht und die Reproduzierbarkeit der Ergebnisse evaluiert. Es konnten signifikante Unterschiede in der

Herzbewegung zwischen beiden Patientengruppen und gesunden Probanden festgestellt werden. Die Studie konnte ausserdem zeigen, dass eine schnelle und genaue Untersuchung der linksventrikulären Dissynchronie die Patientenselektion und individuelle Behandlung im Hinblick auf eine Herzschrittmacherimplantation im Rahmen der Herzresynchronisationstherapie möglicherweise verbessern kann. Als Ergebnis der Studie wurde eine neue Strategie erarbeitet, welche eine schnelle Identifizierung von Regionen mit dissynchroner Herzbewegung erlaubt. Diese Methode, zusammen mit MRI Vitalitätsmessungen, ist von grossem Interesse, um die Implantation einer linksventrikulären Elektrode zu planen. Dies ist ein wichtiger Faktor für eine optimale Herzschrittmacher-Therapie.

Zusammenfassend wird festgestellt, dass die Entwicklung und Anwendung beschleunigter Tagging-Techniken die MRI-basierte Herzbewegungsmessung in die Nähe klinischer Anwendung bringen konnte. Messungen regionaler Herzbewegungsparameter sind kombinierbar mit weiteren Untersuchen wie Perfusions- und Vitalitätsmessungen, mit deren Hilfe die Herzfunktion umfassend charakterisiert werden kann.

Summary

Quantification of mechanical dysfunction of the heart is of great importance for improving medical diagnosis and treatment in a range of cardiovascular diseases. The assessment of regional myocardial motion can give valuable insights into cardiac mechanics in healthy and diseased states. Alterations in cardiac deformation patterns can be early and sensitive indicators of cardiac disease. Magnetic resonance imaging (MRI) offers the possibility to non-invasively assess heart anatomy and function without exposing the patient to ionizing radiation. Myocardial tagging is a dedicated method for accurate and fast quantification of regional cardiac motion. With MRI tagging, tissue magnetization is modulated prior to image acquisition and the resulting line-, grid- of lattice-patterns stay with the underlying tissue, allowing tracking and quantifying of cardiac motion. Previous studies have demonstrated the outstanding potential of this technique in preclinical cardiac research.

The objective of the present thesis was the development and application of accelerated MRI tagging acquisition and post-processing techniques to characterize regional heart wall dynamics in healthy and diseased hearts.

Acquisition and post-processing of motion encoded data can be accomplished using a variety of different techniques. Most of them are closely related with each other and show high similarities. Advantages and optimal implementations of the different methods in a practical setting were evaluated and are discussed in this thesis.

The complex three-dimensional nature of cardiac motion requires complete coverage of the heart during data acquisition and the assessment of three-dimensional displacement trajectories. A novel tagging acquisition scheme was developed to allow acquiring three-dimensional, motion encoded data fast and efficiently. The applied tagging technique compensates tag fading over time by the acquisition of two complementary data sets which are subtracted of each other (Complementary Spatial Modulation of Magnetization, CSPAMM). For the acquisition of three-dimensional tagging data, three data sets were acquired which were each motion encoded in one spatial direction. Scan time could significantly be reduced by implementing the tagging modulation selectively, what allowed

reduction of the imaged volume to the dimensions of the heart. A fast, segmented echo-planar imaging MRI sequence with multiple RF-excitations per heart phase was employed for data read-out. For post-processing of three-dimensional tagging data, an existing technique that proved to be fast and reliable in previous studies was extended to enable analysis of volumetric data.

Two- and three-dimensional tagging techniques were developed in this thesis and both validated and applied in healthy volunteers and patients with various cardiac diseases. Novel calculation methods were worked out to express and quantify a possible dysfunction in heart wall motion. New strategies developed in patient studies allow drawing conclusions with regard to individual therapy planning.

The methods developed have permitted the application of three- and two-dimensional tagging techniques not only in healthy volunteers but also in larger patient cohorts. Two-dimensional tagging was utilized to measure cardiac motion in patients with Fabry disease. Fabry disease is a rare genetic metabolic disorder affecting most of the organs including the heart. The disease is progressive with age and often leads to death due to heart failure. A slice following technique was applied to eliminate through-plane motion effects, and multiple slices were acquired in different orientations to cover the entire left ventricle. Alterations of cardiac motion could not only be observed in patients with macroscopic cardiac involvement, but also in patients showing early signs of cardiac disease. While both circumferential contraction and longitudinal shortening were only altered in patients with hypertrophic hearts, significant alterations in apical rotation and left ventricular torsion could also be measured at an early stage of disease.

The three-dimensional tagging technique was applied in a large study to measure left ventricular contraction and dyssynchrony in patients with left bundle branch block (impairment of the cardiac electrical conduction system) and in patients after myocardial infarction. A variety of cardiac motion parameters was assessed and reproducibility of the obtained results was validated. Significant differences in cardiac motion between each group of patients and healthy volunteers could be measured. The study has demonstrated that fast and accurate assessment of left ventricular dyssynchrony has the potential to improve patient selection and individual treatment of these patients with regard to biventricular pacing as part of cardiac resynchronization therapy. As a result, a novel strategy was proposed allowing for fast detection of areas exhibiting dyssynchronous myocardial motion. This method can be used in combination with MRI viability measurements for planning of left ventricular lead placement, an important factor concerning optimal therapy implementation.

In conclusion, the development and application of accelerated tagging techniques has brought MRI based cardiac motion quantification within reach of clinical applicability. Assessment of cardiac deformation can be combined with further measurements such as perfusion and viability imaging to characterize cardiac function in a comprehensive manner.

Introduction

The heart is a muscular organ that is responsible for moving blood through the vessels in order to ensure blood circulation in all organs. By regular, rhythmic contractions of the left ventricle oxygenated blood is pumped into the aorta and through the systemic circulation (1). From the capillaries in the organs and in the periphery of the body, deoxygenated blood returns to the right ventricle of the heart. The right ventricle pumps the blood into the pulmonary circulation and into the lungs where blood is oxygenated. Pulmonary veins return the oxygen-rich blood to the heart, where it enters the left atrium before flowing into the left ventricle. The unidirectional flow of the blood is maintained by the mitral and the aortic valve of the left ventricle, the tricuspid and the pulmonary valve of the right ventricle and additional valves in the veins. The simultaneous and uniform contraction of the healthy heart is triggered by means of electrical impulses sent to the myocardial fibers through the excitation and conduction system.

The description and understanding of cardiac anatomy and function are challenging tasks due to the complexity of the heart and the cardiovascular system. A deeper knowledge of the heart functionality is, however, of great importance for improving medical diagnosis and treatment of cardiovascular diseases. Alterations in the myocardial motion pattern are often early and sensitive indicators for cardiac disease such as reduced myocardial perfusion due to coronary artery stenosis (2) or acute allograft rejection after heart transplantation (3). Moreover, assessment of left ventricular dyssynchrony can be an important factor for determining long-term prognosis and optimal treatment after myocardial infarction (4) and can give valuable insights with regard to cardiac resynchronization therapy (5).

Non-invasive techniques are therefore required, that are not only capable of imaging cardiac anatomy but also ventricular function. Echocardiographic methods are widely used to assess myocardial function in healthy and diseased states. Using tissue Doppler imaging (6) and speckle tracking echocardiography (7), it is possible to perform quantitative assessment of regional cardiac function and synchronicity both at rest and under stress conditions. However,

echocardiographic measurements present with several limitations, mainly with regard to through-plane motion and poor acoustic windows.

Magnetic resonance imaging (MRI) offers the possibility to quantify regional myocardial motion in great detail and stands out for its versatility. Imaging planes can be oriented arbitrarily and motion measurements can be combined with further examinations, such as myocardial perfusion (8), coronary flow (9), viability imaging (10) and cardiac valve function (11).

Using MRI tagging (12), tissue magnetization is saturated on selected locations in the myocardium prior to the imaging process. With Spatial Modulation of Magnetization (SPAMM) (13) a regular line or grid pattern is produced that moves with the underlying tissue and allows quantifying regional displacements of the myocardium. The technique was further developed to improve tag persistence over the cardiac cycle using Complementary SPAMM (CSPAMM) (14). CSPAMM can be combined with a slice-following technique (15) to overcome problems with regard to through-plane motion. The post-processing of tagged image data sets is a fundamental task to extract quantitative motion parameters. With the introduction of Harmonic Phase (HARP) processing (16), fast and reliable tracking of arbitrary landmark points has become possible and user interaction could be drastically reduced compared to previous techniques.

During the cardiac cycle the heart performs a complex three-dimensional motion pattern caused by the particular arrangement of myocardial fibers. The overall uniform circumferential contraction of the healthy left ventricle with more endo- and less epicardial deformation is accompanied by longitudinal shortening and a wringing motion between base and apex during systole. In the diseased state, this contraction pattern often presents with significantly altered properties (17). In order to assess the motion of the entire left ventricle and to capture possible regional motion defects, multiple tagged slices need to be acquired in different orientations. This combination of two-dimensional techniques does, however, lead to slice misregistration problems and long acquisition times. Alternatively, tagging preparation can be applied in three dimensions and a volume of the whole heart can directly be acquired (18). This technique successfully addresses slice registration issues but overall scan times are too long for application in patients and in larger clinical studies.

Further development of tagging acquisition and post-processing methods along with their applications in clinical studies is of great interest in clinical cardiology. The requirement to fit the entire tagging examination within a few short breath-holds is of particular importance as many of the patients are unable to sustain breath-holds over extended periods.

Objectives

The focus of this thesis lies in the characterization of cardiac motion in healthy and diseased hearts by developing and applying new strategies for MRI data acquisition and post-processing.

For the acquisition of motion encoded data, effective and fast techniques are required in order to allow for a comprehensive analysis of whole-heart wall motion. Fast and reliable post-processing of motion encoded data is needed and quantitative results should be both objective and reproducible. Accordingly, an optimized acquisition scheme is developed demonstrating that three-dimensional tagging data covering the entire left ventricle can be acquired in extremely short scan times. Patients have to sustain three breath-hold periods of 18 heart beats duration only for acquisition of a complete data set. An existing tagging post-processing method that was successfully applied in previous studies is applied and extended to enable the analysis of volumetric motion encoded data with minimal user interaction.

Application and validation of developed methods in patient studies are prerequisites to transfer new techniques into clinical research and diagnostics. Two- and three-dimensional tagging methods are therefore applied in healthy volunteers and in different patient groups. Regional motion parameters are measured over the entire left ventricle in order to validate the methods and to characterize and compare left ventricular function in these subjects. For an improved quantification of the complex left ventricular motion pattern, new parameters are proposed and evaluated. Important aspects of cardiac deformation are examined, such as left ventricular contraction, torsion and synchronicity.

Outline

Chapter 1

The introductory chapter gives an overview over different methods to measure tissue motion using MRI. Data acquisition techniques which encode displacement, velocity and strain are presented and discussed. The concepts of SPAMM and CSPAMM are introduced. By applying CSPAMM in its generalized formulation, N-SPAMM, it is possible to eliminate additional artifact-generating echoes. Furthermore, the post-processing technique HARP and its implications on image acquisition are discussed. In the following, Displacement Encoding with Stimulated Echoes (DENSE) is introduced and discussed in order to devise similarities between HARP and DENSE along with practical implications. At the end of the chapter, a

general overview over strain calculation is provided to establish the theoretical background for describing tissue motion.

Chapter 2

An optimized acquisition scheme is introduced which allows acquiring three-dimensionally tagged CSPAMM data covering the entire left ventricle in extremely short acquisition times. Three breath-hold cycles of 18 heart beats duration only are required for the acquisition of a complete three-dimensional, motion encoded data set. Each breath-hold is used to acquire a volumetric data set with motion encoding in one spatial direction. An optimized data acquisition sequence is applied in combination with localized tagging preparation to allow for faster acquisition within a limited field-of-view. Navigator control ensures similar diaphragm positions in all breath-holds. An enhanced variant of the HARP algorithm is extended to three dimensions for the measurement of true three-dimensional motion parameters of the heart. The feasibility of the method is tested in healthy volunteers and in patients with myocardial infarction.

Chapter 3

Two-dimensional tagging using slice-following CSPAMM combined with HARP post-processing is applied to measure left ventricular shortening and contraction in controls and in patients with Fabry disease. Multiple slices are acquired in different orientations to characterize motion on different cardiac levels and in long-axis direction. Additionally, left ventricular rotation and global left ventricular torsion are examined. The study demonstrates that tagging acquisition and analysis methods are not only applicable in hypertrophic patients with myocardial motion abnormalities but can also be used to study patients without macroscopic cardiac involvement such as in an early stage of Fabry disease.

Chapter 4

Accelerated three-dimensional tagging is applied to measure left ventricular dyssynchrony and cardiac mechanical function in patients with left bundle branch block, patients after myocardial infarction and controls. Different parameters that have been suggested in previous animal studies to measure left ventricular dyssynchrony are validated in patients and controls. Results from 3D tagging are correlated with the amount of scar tissue as measured by MRI viability imaging. Finally, a new strategy is developed to select patients for cardiac resynchronization therapy and to guide individual treatment.

Chapter 1:

Measuring Tissue Displacement with MRI

1.1 Overview

Several techniques exist to measure tissue motion with MRI. Most of them are closely related with each other and can similarly be applied to quantify tissue displacement of various organs including the heart. Nevertheless, there are a few differences between the methods with practical consequences, which are discussed herein.

Tagging MRI (12,13) modulates the longitudinal magnetization prior to data acquisition (section 1.2). The resulting tagging pattern moves with the underlying tissue and allows the assessment of regional motion characteristics over the cardiac cycle. During the first years after introduction of the tagging method, extraction of quantitative motion parameters from tagging data sets was achieved by dedicated post-processing tools based on the detection of the tagging lines in the images. Harmonic Phase (HARP) (16) analysis has greatly facilitated this crucial post-processing step by splitting signal components with opposed angular velocity into a single circularly polarized vector to track landmark points on the basis of signal phase through multiple heart phases (section 1.3).

Displacement encoded phase images can directly be obtained during image acquisition using Displacement Encoding with Stimulated Echoes (DENSE) (section 1.5). The technique employs the same encoding principle as the tagging method, but instead of applying a k-space filter during (HARP) post-processing, decoding is already performed during data acquisition. Even though the two approaches are very similar, there are a few limitations and advantages inherent to both of them (section 1.6).

Further methods to assess cardiac mechanical function by MRI include phase-contrast velocity encoding and strain-encoding (SENC). With phase-contrast velocity encoding (19,20) bipolar gradients are employed prior to data read-out, in order to obtain phase-values that are proportional to blood/tissue velocities in the measured spatial direction. Displacement fields can then be calculated by integrating the obtained velocity data over time. Similar to DENSE, SENC (21) applies both encoding and decoding gradients. However, with SENC tagging preparation is applied in a direction orthogonal to the imaging plane and two data sets with different demodulation frequencies are acquired. The resulting image intensities are dependent on the compression and stretching of the tissue in through-plane direction due to intra-voxel dephasing. Accordingly, maps characterizing strain in through-plane direction can be computed from these images. Both methods, phase-contrast velocity encoding and SENC,

are well suited for various applications but they exhibit intrinsic disadvantages when used for quantification of whole-heart mechanics. While the phase-contrast method determines tissue displacement only indirectly by measuring velocity values, through-plane strain is exclusively measured with SENC and no tracking of tissue points is possible. Additionally, SENC does not allow for a three-dimensional data acquisition scheme as knowledge about the excitation slice profile is needed for strain calculation.

1.2 Tagging Acquisition Methodology

Tagging of myocardial tissue using MRI was first introduced by Zerhouni et al. (12). The basic idea was to non-invasively create markers in the moving tissue in order to observe and assess myocardial motion. Thereby, the magnetization of the tissue is labeled or tagged by applying a spatially modulated saturation RF pulse before the actual MR imaging procedure. In practice, the tagging preparation sequence is played out upon detection of the ECG R-wave in planes perpendicular to the imaging plane. Since magnetization represents a characteristic tissue property, saturated regions are moving with the underlying tissue and can be used to quantify regional cardiac motion. Due to T1 relaxation the tags are only visible during a limited time period. However, at 1.5 T, the T1 relaxation time of healthy myocardium is about 850ms and therefore long enough to study cardiac contraction during the entire duration of a cardiac cycle.

Spatial Modulation of Magnetization (SPAMM)

An effective way to periodically modulate longitudinal magnetization was introduced by Axel et al. (13). By applying a sequence of two nonselective RF pulses separated by a dephasing gradient (Figure 1.1), periodic Spatial Modulation of Magnetization (SPAMM) is created. Thereby, the originally longitudinal magnetization (Figure 1.1a) is flipped by the first RF pulse into the transversal plane (Figure 1.1b). The subsequent gradient dephases the spins in a direction perpendicular to the normal axis of the imaging slice (Figure 1.1c) and a second RF pulse flips the magnetization back into longitudinal direction. All of the remaining transversal magnetization decays fast with T2* and can additionally be spoilt using further gradients in through-plane direction. A sinusoidal modulation pattern of M_z magnetization remains after completion of the tagging preparation sequence (Figure 1.1d). The tagging modulation

manifests itself in *k*-space by two conjugate harmonic peaks at the locations of the tagging modulation frequency.

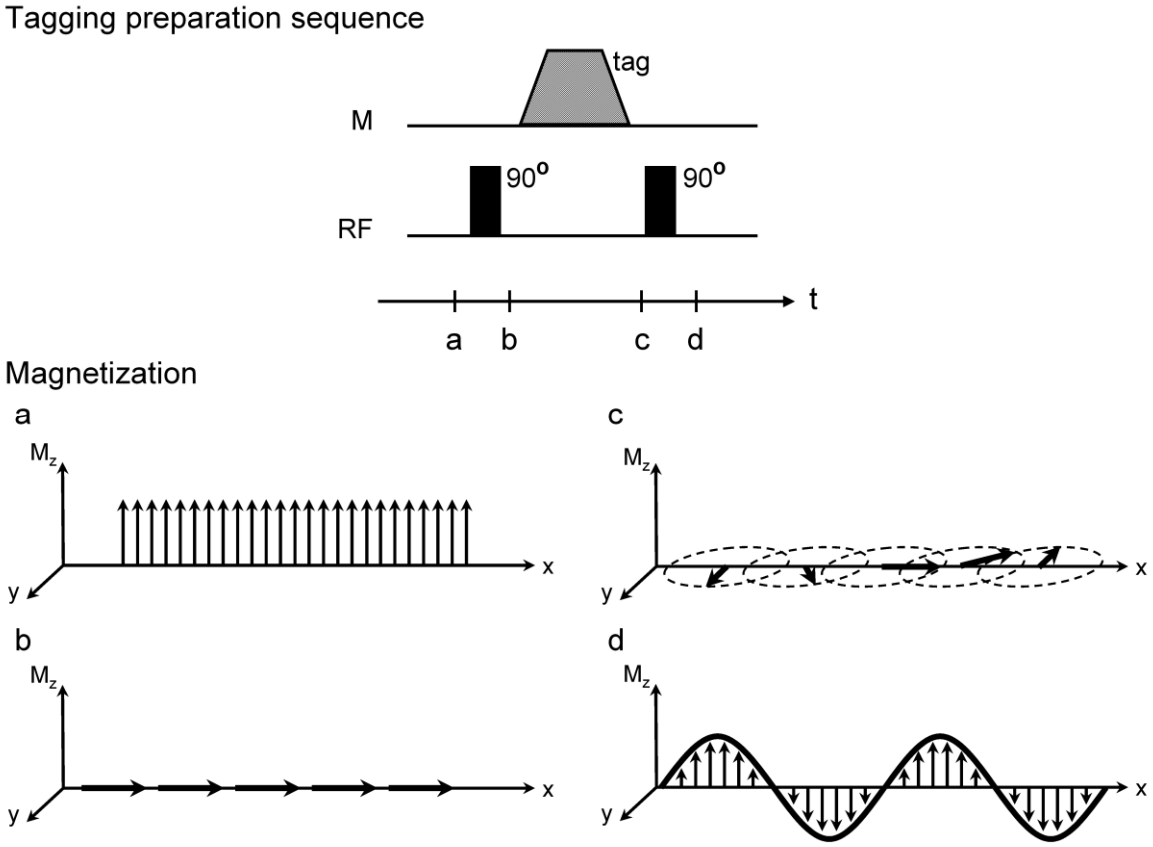

Figure 1.1: *Tagging preparation. The tagging preparation sequence is shown, consisting of two RF block pulses interspersed by a dephasing gradient in measurement (M) direction. The state of the magnetization is shown for the time points a, b, c and d in the sequence. The magnetization is flipped from the longitudinal axis (a) into the transversal plane (b), dephased along the measurement direction (c) and flipped back, resulting in a sinusoidal modulation of the longitudinal magnetization (d).*

The modulated magnetization is then imaged and the resulting tagging pattern moves with the underlying tissue. Due to T1 relaxation effects, however, tag fading occurs and the contrast-to-noise ratio decreases rapidly over time (Figure 1.2, top row). In *k*-space, tag fading is represented by an emerging signal at zero spatial frequency (DC). Another drawback with SPAMM is considerable through-plane motion that can occur especially when imaging

cardiac short-axis slices. Consequently, accuracy and precision of the obtained motion parameters are limited.

By using more RF pulses that are each separated by dephasing gradients and by binomially distributing the amplitudes of the RF pulses, sharper tagging stripes can be obtained (22). As a consequence, higher order harmonic peaks are created in *k*-space. Additionally, a two-dimensional grid of tagging lines can be produced by adding a second tagging preparation sequence immediately after the first one and orienting the gradients in orthogonal directions (22).

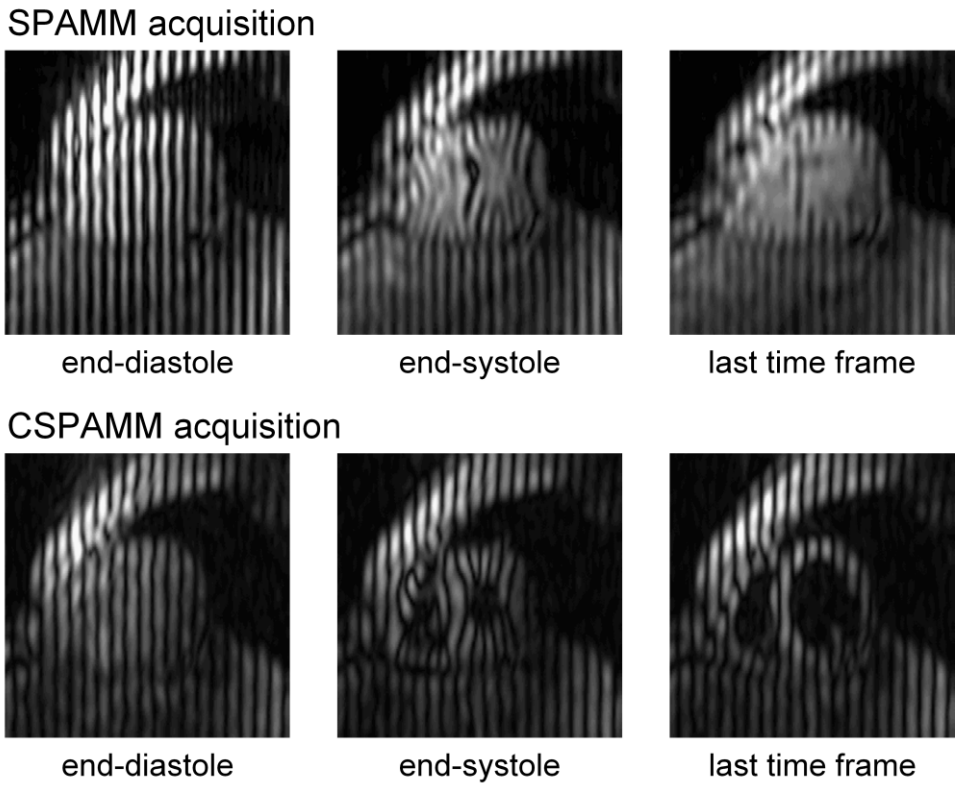

Figure 1.2: *Exemplary SPAMM and CSPAMM short-axis images from a healthy volunteer. The end-diastolic images represent the first time frames acquired immediately after the ECG R-wave. Additionally, the time frames at maximum contraction, i.e. at end-systole, and the last acquired time frames are shown. While there is significant tag fading with the SPAMM acquisition due to T1 relaxation, a constant contrast-to-noise ratio can be observed throughout the cardiac cycle using the CSPAMM acquisition method.*

Complementary Spatial Modulation of Magnetization (CSPAMM)

Complementary SPAMM (CSPAMM) was introduced (14) to improve the tagging contrast in later heart phases. With CSPAMM, a second SPAMM acquisition is performed with inverted tagging modulation. The 180° phase shift of the tagging modulation can be achieved by adding a phase shift of 180° to the second RF pulse in the tagging preparation sequence. By subtracting the second, complementary SPAMM data set from the first scan, the DC signal component is canceled. Thus, signals not carrying any motion information are suppressed.

The signal intensity I_{Tk} for the k^{th} (k=1…n) heart phase image of a CSPAMM acquisition can be described as (14):

$$I_{Tk} \propto M_{SS} TAG(x,y) \exp\left(-\Delta t / T_1\right) \left(\prod_{j=1}^{k-1} \cos\left(\alpha_j\right) \right) \sin\left(\alpha_k\right), \qquad [1.1]$$

where M_{SS} denotes the steady state magnetization, $TAG(x,y)$ the spatial modulation of the magnetization, Δt the time interval between the heart phase images and $\alpha_1 \ldots \alpha_k$ the variable RF excitation angles. By careful design of the imaging sequence, it is possible to apply an optimized flip angle train such that a constant tagging signal is generated throughout the cardiac cycle for a tissue with known T1. The optimized flip angles can be calculated according to (14,23):

$$\alpha_{k-1} = \arctan\left(\sin\left(\alpha_k\right) \exp\left(-\Delta t / T1\right)\right). \qquad [1.2]$$

The optimal final flip angle α_n can be calculated numerically as described in (23), depending on T1, cardiac frequency and imaging parameters (number of heart phases, temporal resolution). Therefore, when combining the CSPAMM method with ramped flip angles for data acquisition, a constant contrast-to-noise ratio through all heart phases can be achieved (Figure 1.2, bottom row).

To address the problem of through-plane motion, the CSPAMM technique can be enhanced by a slice following procedure (15). By implementing the first RF pulse of the tagging preparation sequence slice-selectively, the tagging modulation is restricted to a thin slice only. A larger volume is read out that encompasses the largest expected displacement of the tagged slice. After the subtraction of the complementary CSPAMM data sets all signal parts without tagging modulation are suppressed. Thus, in all heart phases a signal projection of only the (displaced) tagged tissue can be observed in the final CSPAMM image.

Suppression of multiple harmonic peaks using N-SPAMM

For the post-processing of tagging data, it is important to isolate displacement encoded peaks (section 1.3) either by filtering or during data acquisition. With CSPAMM the DC peak is suppressed by acquiring a second measurement with phase-shifted tagging modulation and subtracting this second scan from the first measurement. A generalized concept of the CSPAMM technique is N-SPAMM (24,25). The N-SPAMM concept states that it is possible to separate N harmonic peaks by acquiring N SPAMM measurements with different tagging modulations.

The N-SPAMM method is illustrated in Figure 1.3 for N=3. Due to the Fourier shift theorem, the harmonic peaks in *k*-space exhibit different phases depending on the shift of the tagging modulation in image space, whereby the corresponding harmonic peaks at negative spatial frequency are complex conjugated. If N data sets are acquired each phase shifted by 1/N of the tagging modulation period, the harmonic peaks can be separated by applying the Fourier transformation across all N scans.

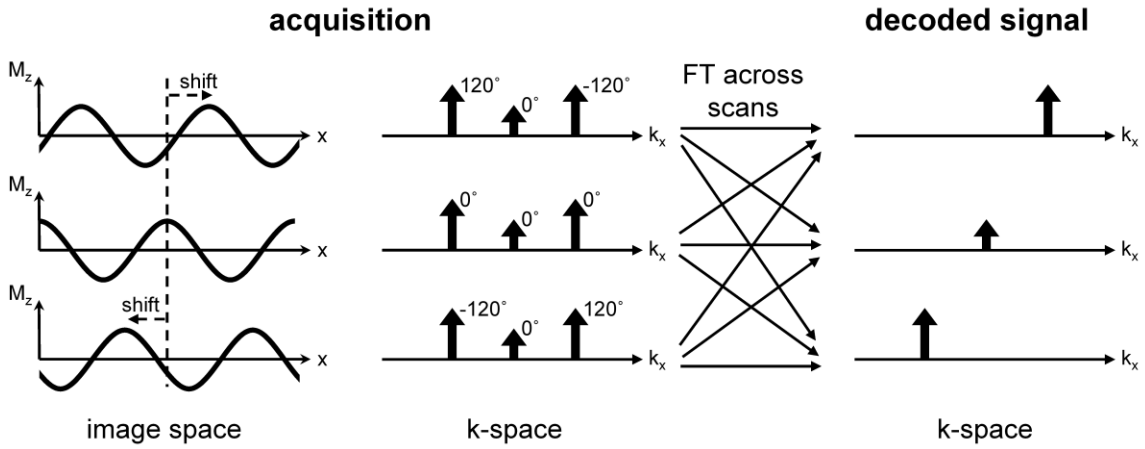

Figure 1.3: *N-SPAMM method for N=3. Three tagging data sets are acquired each phase shifted by 1/3 of the tagging modulation period. Due to the Fourier shift theorem, the harmonic peaks are phase shifted accordingly. By applying the Fourier transformation (FT) across the acquired scans, the harmonic peaks can be separated.*

The concept can be extended to two- and three-dimensional tagging (e.g. grid and lattice tagging). For N>1, a slice following technique as described above can be incorporated. The

advantage of isolating the harmonic peaks during data acquisition without applying bandpass filters is that signal loss due to intra-voxel dephasing (26) can be minimized by applying a larger tagging distance. Hence, the image signal-to-noise ratio (SNR) is increased. On the other hand, while weaker motion encoding increases the image SNR, the sensitivity to measured displacements is decreased with large tagging distances (27). For a given examination, the tagging sequence needs to be chosen carefully, in order to optimize the two contradicting requirements of high SNR and high sensitivity to displacements. Additionally, the increased amount of scan time needs to be considered when acquiring additional data sets with N-SPAMM.

1.3 Harmonic Phase (HARP) Post-Processing

While major alterations in cardiac motion can be observed visually on tagging images, post-processing techniques are needed in order to obtain quantitative and reproducible results fast and with a minimal amount of user interaction.

Harmonic Phase (HARP) post-processing was introduced by Osman et al. (16) as a fast and robust method to automatically analyze tagging data. Figure 1.4 illustrates the underlying principle of the HARP method. With HARP, a bandpass filter is used in *k*-space to extract one of the harmonic peaks that appear at conjugate locations of the tagging modulation frequency. The bandpass filter usually has a circular shape with rounded edges to reduce Gibbs ringing. As a result, a low pass filtered magnitude image without tagging modulation is obtained in image space. The corresponding (harmonic) phase is increasing along the tagging direction with phase wraps parallel to the tagging lines. It can be shown (16), that the harmonic phase is characteristic for the underlying tissue elements. Therefore, tissue tracking becomes possible by simply following the same phase values through consecutive time frames. Arbitrary landmark points can be defined and automatically tracked through all heart phases. To measure displacements in a two-dimensional plane, two harmonic phase images with motion encoding in two independent spatial directions are needed for reliable and accurate motion tracking.

The employment of a bandpass filter in *k*-space results in a reduced spatial resolution of the obtained motion parameters, which demands careful considerations when interpreting the results. Furthermore, since the harmonic peaks change their positions in *k*-space during

cardiac contraction and rotation (28), limitations for the maximal detectable strain values are defined by the HARP filter.

HARP allows for fast and user independent tagging post-processing. In contrast to previous techniques, HARP is not restricted to the (time consuming and error-prone) detection of tag lines using grey value images. Not only tracking of material points is possible, but also direct strain determination by calculation of the spatial derivatives of the HARP images (29) (section 1.7).

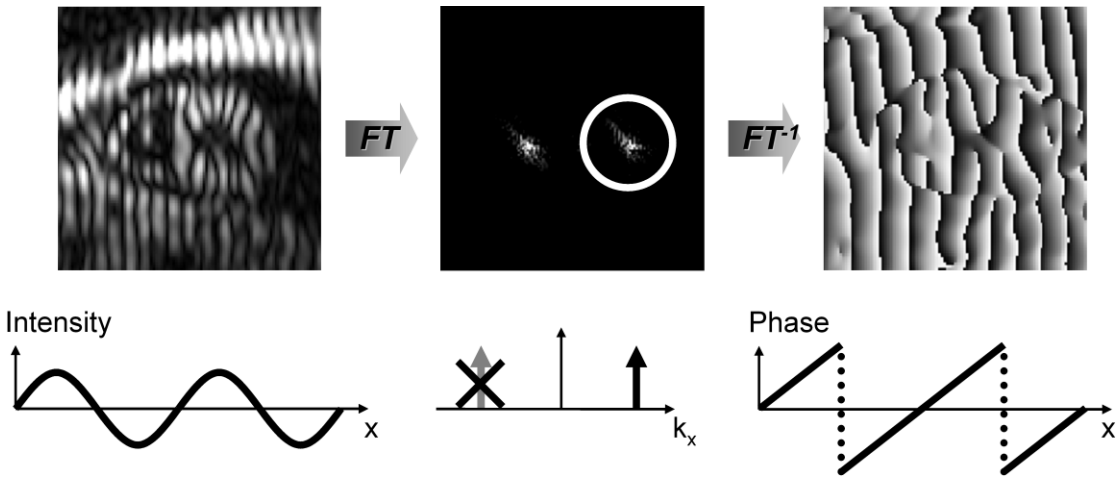

Figure 1.4: *Harmonic phase (HARP) post-processing of a tagged short-axis image acquired at end-systole (first row) and a schematic illustration of the method (second row). With HARP, one of the two harmonic peaks that appear at conjugate locations of the tagging modulation frequency is extracted using a circular bandpass filter. The resulting (harmonic) phase in image space is fixed with respect to the underlying tissue and can be used for motion tracking.*

Peak-combination HARP

HARP images do not only contain the displacement-encoded phase, but also additional phase contributions from the receiver and the receiver coil as well as from non-idealities such as B_0 inhomogeneity, chemical shift and flow. Motion quantification with HARP is adversely affected by any spatially and particularly temporally varying spurious phases. Tracking errors and non-accurate myocardial motion estimation might result. Furthermore, when acquiring

both first harmonic peaks and applying a HARP filter (as shown in Figure 1.4), the displacement information contained in the conjugate peak is discarded.

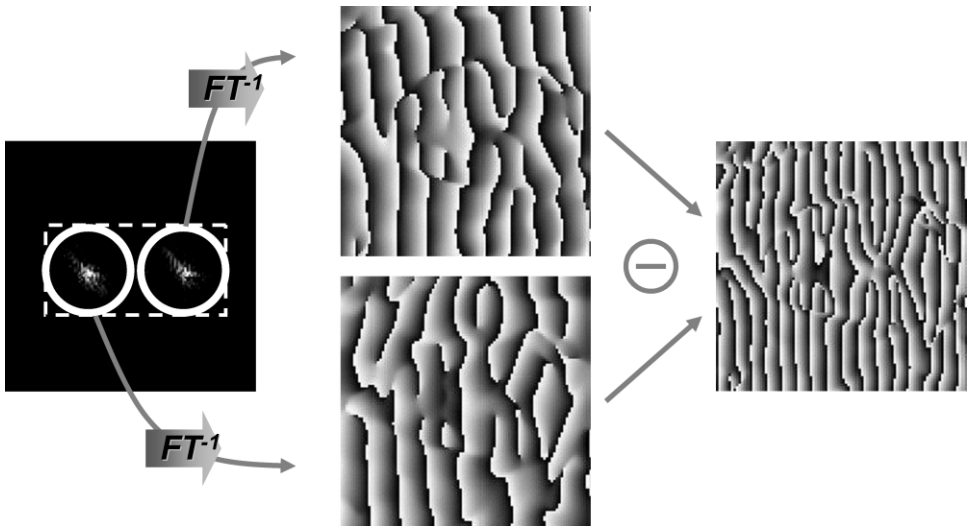

Figure 1.5: *Peak-combination HARP. Both harmonic peaks are extracted and the resulting HARP images are subtracted from each other. As a result, phase contributions due to B_0 inhomogeneities are eliminated in the peak-combined HARP image, but the number of phase wraps is doubled. For tagging acquisition, only the fraction of k-space delineated by dashed lines needs to be sampled.*

Peak-combination HARP was introduced (30) (Figure 1.5), in order to suppress artifacts from non-idealities such as B_0 inhomogeneity and to increase the SNR of the motion information,. In contrast to conventional HARP, the peak-combination method extracts both harmonic peaks in *k*-space. The corresponding harmonic phases of the positive ($P^+(x)$) and the negative peaks ($P^-(x)$) are:

$$P^{\pm}(x) = \pm\varphi(x) + \beta(x)\,, \qquad [1.3]$$

where $\varphi(x)$ describes the displacement-encoded phase contrast resulting from tagging. $\beta(x)$ contains any remaining phase unrelated to motion, including spurious phases due to B_0 inhomogeneity. With peak-combination HARP, $P^-(x)$ is subtracted from $P^+(x)$:

$$P^{+}(x) - P^{-}(x) = 2\varphi(x)\,, \qquad [1.4]$$

thus eliminating any phase contribution originating from B_0 inhomogeneities. Additionally, since the motion encoded phase from both harmonic peaks is included equally in the calculation, the SNR of the displacement measurement increases by a factor of $\sqrt{2}$. However,

the number of phase wraps in the final peak-combined HARP image is doubled due to the factor 2 in equation [1.4] (Figure 1.5).
The elimination of artifacts in the HARP images and the increased SNR yields overall improved accuracy and reproducibility with peak-combination HARP relative to conventional HARP (30).

1.4 Considerations on the Design of Tagging Sequences

The use of HARP for data post-processing has several implications on the parameters of the applied tagging sequence.
Since only the first order harmonic peaks carry the fundamental mode of motion and are extracted in data post-processing, tagging sequences can be optimized such that only these signal parts are actually acquired and that all additional unwanted signal contributions are efficiently suppressed. In order to concentrate as much signal as possible in the first harmonic peaks, conventional 1-1 sinusodial SPAMM tagging is preferable over higher order tagging techniques (22) as these distribute the signal content among a greater number of harmonic peaks. CSPAMM is considered beneficial over SPAMM as it suppresses the untagged signal peak, thereby improving peak separation and reducing artifacts resulting from peak overlap. Moreover, CSPAMM can be combined with slice following, and thus eliminates through-plane motion effects (section 1.2).
Basically, the HARP method only requires data from a single harmonic peak. An acquisition procedure called FastHARP (31) was therefore developed to save scan time by only reading out one component of the conjugate pair of harmonic peaks resulting from SPAMM tagging. However, as described in section 1.3, valuable additional information can be gained by acquiring both conjugate peaks. Artifacts such as phase shifts due to B_0 inhomogeneity are suppressed and the SNR of displacement encoding is improved. Since tagging data are often acquired with an echo-planar imaging (EPI) sequence (23), a slightly longer acquisition along the primary read-out direction to acquire both harmonic peaks will not degrade acquisition performance significantly. Therefore, the acquisition of both conjugate harmonic peaks in combination with peak-combination HARP provides an efficient strategy to obtain artifact-free motion data with high SNR. On the other hand, FastHARP can be used for data acquisitions within a limited amount of time (e.g. real-time imaging, (31)).

Since only two harmonic peaks are required for post-processing with peak-combination HARP, only the fraction of *k*-space around the two peaks needs to be sampled during data acquisition (Figure 1.5, dashed lines). In order to fully sample both conjugate harmonic peaks in measurement direction, the maximum spatial encoding frequency $k^m_{\max}$ needs to be at least two times as great as the tagging encoding frequency k_{enc}:

$$k^m_{\max} \geq 2k_{enc}\,. \qquad [1.5]$$

In phase encoding direction, however, data can be acquired with a lower spatial resolution in order to save scan time. To obtain similar spatial resolution in phase encoding direction as in measurement direction, the spatial encoding frequency $k^p_{\max}$ needs to be equal or greater than k_{enc}:

$$k^p_{\max} \geq k_{enc}\,. \qquad [1.6]$$

Thus, the required *k*-space data can be acquired efficiently by employing an EPI sequence and aligning the read-out direction with the tagging encoding direction.

Due to the magnitude operation in creating intensity images, the tag distance d_{tag} is defined as half the cycle length of the tagging modulation:

$$d_{tag} = \frac{\pi}{k_{enc}}\,. \qquad [1.7]$$

To avoid HARP tracking errors due to phase aliasing, tissue displacement between consecutive time frames should not exceed $2 \cdot d_{tag}$ ($1 \cdot d_{tag}$ with peak-combination HARP). Tag distance and temporal resolution should therefore be adjusted accordingly in order to ensure reliable motion tracking.

The maximal radius of the HARP bandpass filter that can be applied to CSPAMM data equals the distance between the center of *k*-space and the first harmonic peak. This filter size corresponds to a spatial resolution of the measured displacement data that is identical to the tag distance. In practice, the radius of the HARP filter is usually chosen smaller due to the presence of residual DC signal and noise. Hence, for tagging studies applying CSPAMM the final spatial resolution of displacement parameters is usually less than the tag distance.

In order to improve the spatial resolution of the displacement data, a shorter tag distance (i.e. a higher k_{enc}) needs to be applied. As a consequence, data have to be acquired with a higher spatial resolution in order to fulfill equations [1.5] and [1.6], leading to a reduction in SNR. Since with a shorter tag distance more wraps occur in the harmonic phase, temporal resolution also needs to be improved to prevent HARP aliasing during tracking. Thus, smaller flip angles

per heart phase have to be applied (23), compromising the SNR additionally. In conclusion, spatial and temporal resolutions have to be adjusted carefully in tagging acquisitions, in order to ensure sufficient SNR and reliable HARP tracking.

A fundamental constraint, that needs to be considered additionally when planning tagging scans, is given by the limited time available to perform the measurements. Typically, the acquisition of a tagged slice should fit within the limited time of one breath-hold to suppress artifacts due to breathing motion.

1.5 Displacement Encoding with Stimulated Echoes (DENSE)

Displacement Encoding with Stimulated Echoes (DENSE) was developed by Aletras et al. (32) as an alternative method to assess cardiac motion with MRI. Tissue displacement, as measured with DENSE, is directly modulated into the phase of the acquired images.

The preparation sequence employed by DENSE immediately after detection of the ECG R-wave is identical as the one used for tagging (section 1.2). The longitudinal magnetization established within the body is sine-modulated prior to image acquisition, and the resulting signal consists of three harmonic peaks in k-space, the DC peak due to T1 relaxation, the displacement-encoded echo signal and its complex conjugate one. The separation of the peaks is proportional to the displacement encoding frequency k_{enc}. As with HARP, only the echo signals containing motion information, namely the displacement-encoded echo signal and its complex conjugate one are of interest for displacement imaging with DENSE. In contrast to tagging sequences, an additional demodulation gradient is applied with DENSE that shifts one of the displacement-encoded echo signals to the center of k-space prior to data read-out. Data are acquired such that only the motion encoded peak is actually sampled. In order to 'cut out' this central motion encoded echo by the acquisition window, the spatial encoding frequency $k^m_{\max}$ has to be less than the motion encoding frequency k_{enc}, if the DC peak is suppressed using the CSPAMM method:

$$k^m_{\max} \leq k_{enc} \,. \qquad [1.8]$$

The choice of k_{enc} is additionally determined by the peak displacement, as the resulting displacement encoded phase is proportional to k_{enc} and the actual displacement value. Phase wraps in DENSE images can be resolved up to a certain degree using unwrapping

algorithms (33). A bandpass filter and/or sophisticated echo-elimination schemes (27,34) can be applied to completely suppress residual signals of unwanted echoes.

1.6 Tagging / HARP vs. DENSE

With SPAMM and DENSE identical tagging preparation sequences are employed before data acquisition. Thus, no differences in motion encoding exist between the two techniques. However, with DENSE the motion encoded signal is demodulated and only the fraction of k-space around the harmonic peak is sampled. With HARP on the other side, a band-pass filter is applied during post-processing, to extract the same fraction of k-space around the first harmonic peak. While the first harmonic peak appears at its original position in k-space for a tagging acquisition, the peak is shifted to the center of k-space with DENSE. According to the Fourier shift theorem the peaks in k-space can be shifted by adding a linear phase in image-space:

$$F(k_x - a) \quad \xrightarrow{FT^{-1}} \quad f(x)e^{iax}, \qquad [1.9]$$

where a denotes the frequency shift, k_x the spatial frequency and x the spatial location. Thus, HARP and DENSE images only differ by a linear phase shift along the encoding direction and can be transformed into each other retrospectively by simple calculations (Figure 1.6).
The only difference in the image acquisition sequence is the presence of an additional decoding gradient before the DENSE read-out, which shifts the read-out train to the first harmonic peak in k-space. Due to their close relationship, both techniques show very similar properties (35). Basically, all concepts described in sections 1.2 and 1.3, such as suppression of harmonic peaks, slice following and peak-combination, can be transferred to the DENSE method in a straightforward fashion (27,36,37). Similarly, motion tracking and calculation of strain maps can be performed with data acquired by both techniques. The general considerations on data acquisition described in section 1.4 also apply for DENSE acquisitions. However, since only one harmonic peak is sampled with DENSE compared to two peaks with tagging, equation [1.8] for DENSE is different from equation [1.5] that applies for tagging acquisitions. The need to choose a smaller $k^m_{\max}$ for a given k_{enc} has practical consequences. In order to apply peak-combination, two data sets have to be acquired per encoding direction with DENSE compared to only one with tagging. While the total number of k-space samples is still the same for both techniques, the acquisition of only one data set in total can be

performed more efficiently when using EPI for data read-out. On the other hand, DENSE is better suited for spiral imaging. For applications with small displacements, such as the measurement of pulsatile brain motion (38), strong encoding gradients are needed resulting in tagging acquisitions with high spatial resolution (equation [1.5]). To maintain sufficient SNR, DENSE allows for an acquisition with a larger voxel size (equation [1.8]) and is therefore better suited for this kind of applications. For heart motion measurements, both techniques can equivalently be used depending on the read-out sequence.

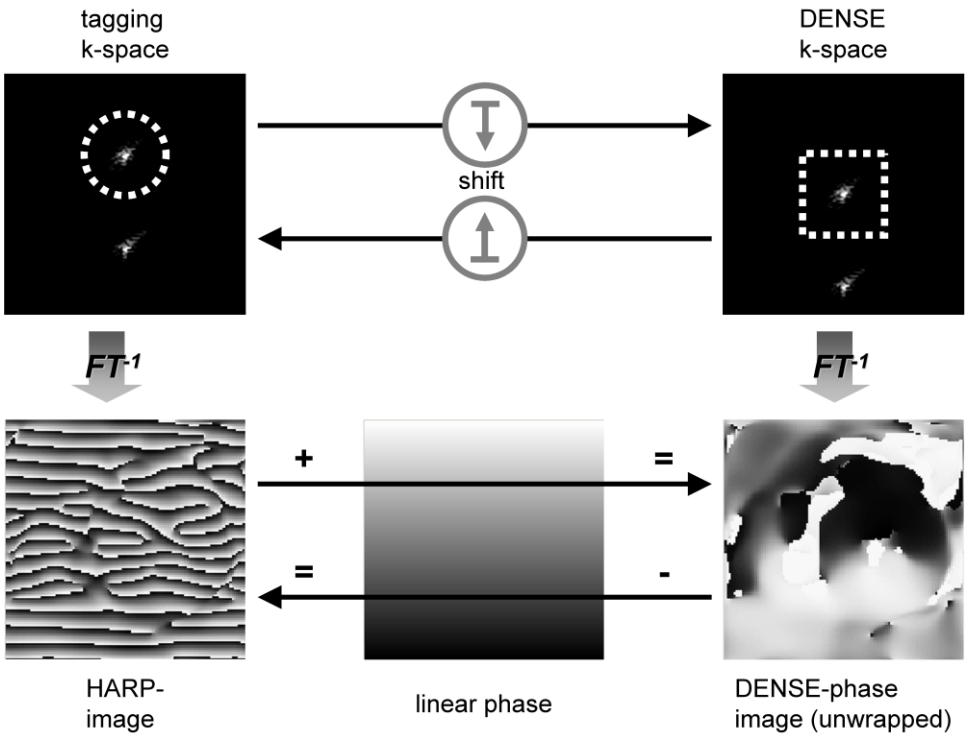

Figure 1.6: *Transformations from HARP images into DENSE phase images and vice versa in k-space (through frequency shift operation) and image space (by adding a linear phase). Dashed lines in k-space illustrate the applied HARP filter for the tagging data and the sampled k-space fraction for the DENSE data (a squared HARP filter or spirals for DENSE read-out could be used alternatively to obtain exactly corresponding data sets). The DENSE phase was unwrapped for better visualization.*

1.7 Analysis of Mechanical Deformation (Strain)

In order to pump blood through the circulatory system of the human body, significant deformation of the myocardium is necessary during contraction and relaxation of the heart. Deformation infers that parts of the muscle change in size and in shape. The geometrical deformation can be described by a strain tensor, which is independent of any rigid body translation or rotation (39). The strain tensor quantitatively relates the actual state of deformation to an 'undeformed' reference state. Even though the heart is always subjected to varying blood pressure, end-diastole is usually defined as the reference state.

Figure 1.7 illustrates different representations of strain. The one-dimensional strain ε is defined as the relative change in length of a vector from the undeformed into the deformed state (Figure 1.7a):

$$\varepsilon = \frac{a' - a}{a}, \qquad [1.10]$$

where a denotes the original undeformed length of the vector, and a' the deformed length. From equation [1.10] follows, that strain is a dimensionless quantity; it is usually expressed as a decimal fraction or a percentage.

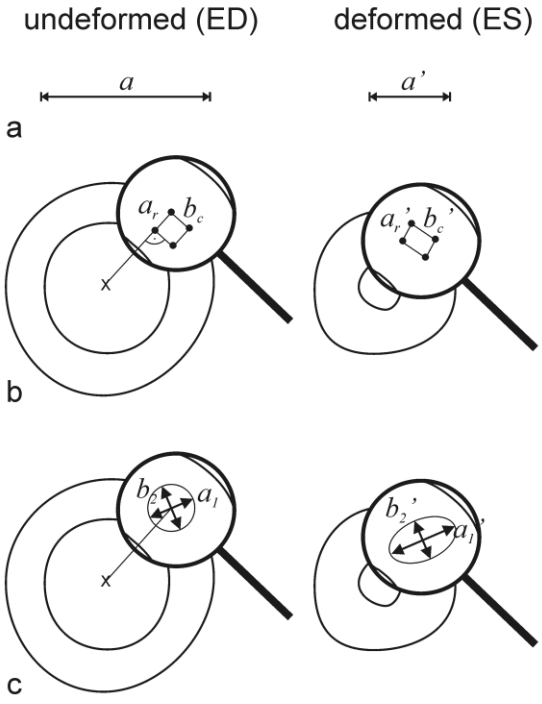

Figure 1.7: *Illustration of strains between the undeformed state at end-diastole (ED) and the deformed state at end-systole (ES). a) One-dimensional strain quantifies the relative change in length of a line segment. b,c) Two-dimensional strains in sketched short-axis slices. Radial and circumferential strains (b) as well as principal strains (c) are illustrated.*

Two-dimensional strains are described by two of these vectors. The deformation of two infinitesimal vectors inside the myocardium can be observed as illustrated in Figure 1.7b. If these vectors are aligned with the radial and the circumferential directions at end-diastole, changes in the length of the vectors and the change in angle between the two vectors ('shear angle') completely describe myocardial deformation in the proximal area. The radial strain ε_r and the circumferential strain ε_c are therefore defined as:

$$\varepsilon_r = \frac{a_r' - a_r}{a_r}, \varepsilon_c = \frac{b_c' - b_c}{b_c}. \quad [1.11]$$

Alternatively, two-dimensional strain can be represented by principal strains. The deformation of an infinitesimal circle at end-diastole into an ellipse at end-systole is given by the relative length changes of the long-axis vector a_1' and of the short-axis vector a_2' of the ellipse (and the angle of a_1 relative to the radial direction) (Figure 1.7c). These vectors also correspond to the eigenvectors of the strain tensor. The principal strains ε_1 and ε_2 are defined as:

$$\varepsilon_1 = \frac{a_1' - a_1}{a_1}, \varepsilon_2 = \frac{b_2' - b_2}{b_2}. \quad [1.12]$$

The principal strains ε_1 and ε_2 can also be obtained by calculating the eigenvalues of the strain tensor.

Chapter 2:

Accelerated 3D Whole-Heart Tagging

2.1 Introduction

To capture the complex three-dimensional (3D) motion of the heart, multiple two-dimensional tagged slices are typically acquired in short-axis and long-axis orientations (40-43). This approach is, however, associated with long acquisition times and prone to slice misregistration. Considerable patient cooperation is required during data acquisition. In addition, the measured data are either affected by through-plane motion or, when applying a slice-following technique (15), contain only two-dimensional projections of cardiac deformation. Sophisticated and computationally demanding algorithms have to be employed to correctly combine the information of all acquired slices and to reconstruct the 3D motion pattern (44,45). To address this problem, displacement in slice encoding direction was additionally encoded in recent studies (46,47). However, the acquisition of multiple slices is still necessary with these techniques.

While two-dimensional techniques are widely used, there is only little experience with true 3D tagging measurements. A 3D Complementary Spatial Modulation of Magnetization (CSPAMM) whole-heart tagging technique for the assessment of myocardial tissue motion was proposed in (18). By applying the tagging preparation in three spatial directions and using a 3D gradient echo sequence for read-out, a 3D motion encoded data set of the whole heart could be acquired. Long net acquisition times of around 16 min and the need to split the scan into multiple breath-holds have, however, prevented the application of 3D tagging in larger study populations. In successive work, shorter acquisition times were achieved by sampling the signal in *k*-space within narrow regions of the harmonic peaks (48). This approach, however, led to reduced spatial resolution in the data and scan times still too long for the technique to be applicable in patients.

For conventional two-dimensional motion encoding, tagging preparation is usually applied as a one-dimensional line pattern (13), and two orthogonally encoded data sets are sequentially acquired in order to obtain two-dimensional motion information (Figure 2.1). The two images can be multiplied for visualization purposes, resulting in an image with a two-dimensional tagging grid. Alternatively, a two-dimensional grid (22) can be created directly during tagging preparation. Similarly, with 3D CSPAMM, either direct lattice tagging as in (18), or one-dimensional line tagging can be applied. With line tagging for 3D motion estimation, three separate orthogonally encoded data sets need to be acquired. In *k*-space, when applying line

tagging in either two or three dimensions, two harmonic peaks at conjugate locations of the modulation frequency are observed for each orthogonally encoded data set. Grid tagging preparation results in four harmonic peaks in *k*-space, lattice tagging in eight peaks.

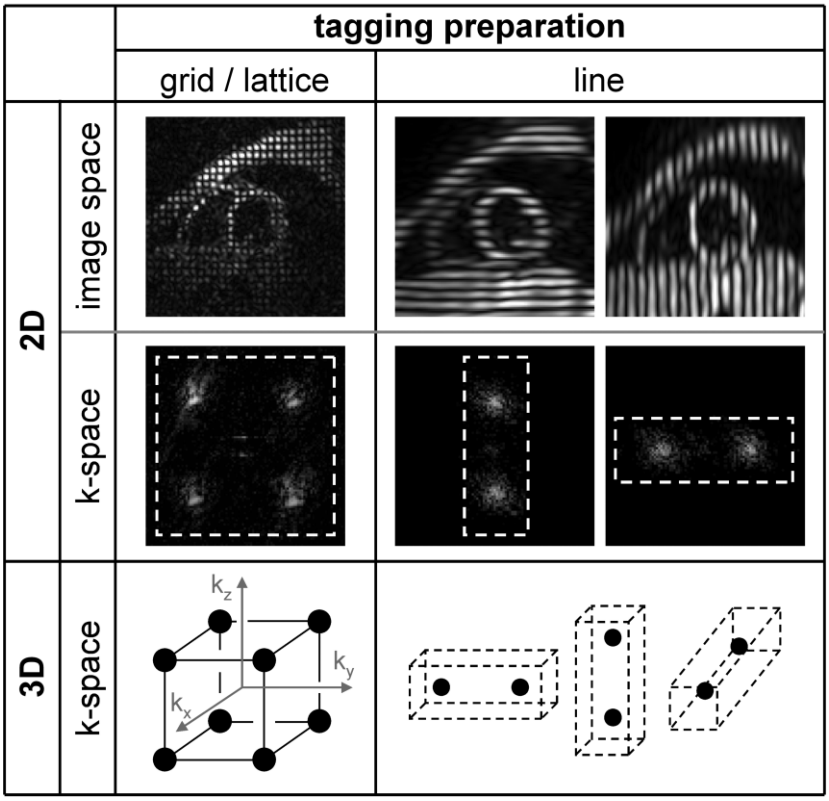

Figure 2.1: *Tagging preparation. In two-dimensional line tagging, two orthogonally encoded data sets have to be acquired, but overall measurement time is shorter relative to grid tagging if only a fraction of k-space around the harmonic peaks is sampled (dashed lines). Location of harmonic peaks after 3D tagging preparation is illustrated in the lower row. Eight harmonic peaks occur with lattice tagging, two per orthogonally encoded data set with line tagging.*

In data post-processing, the Harmonic Phase (HARP) (16) method facilitates automated motion tracking of tissue points through all acquired time frames with minimal user interaction. The filter radius of the HARP bandpass filter is typically chosen to be less than the tagging frequency in order to exclude any residual signal from incomplete subtraction of the DC signal components arising from T1 relaxation. Therefore, with line tagging preparation, less than 50% of *k*-space lines are required in each phase encoding direction to

acquire all data needed for HARP analysis. Accordingly, reduced *k*-space coverage orthogonal to the tagging modulation direction can be afforded (Figure 2.1, acquired *k*-space indicated with dashed lines). By aligning the read-out direction with the tagging preparation direction, an overall shorter scan time is achieved compared to an equivalent grid/lattice tagging examination with full *k*-space sampling (15). For 3D peak-combination HARP analysis a total of six harmonic peaks is required. By using three orthogonal sets of line tagged data, those six peaks can be effectively acquired. Relative to lattice preparation generating eight harmonic peaks, scan time is therefore inherently reduced by 25%. In addition to reduced acquisition time, there are further advantages of the line tagging method. Given the shorter line tag preparation time relative to grid/lattice tag preparation, reduced signal T2* decay and less tissue motion occur during tagging preparation. Since the signal is divided across only two harmonic peaks with line tagging compared to four or eight peaks with grid or lattice tagging, respectively, the signal-to-noise ratio of each acquired peak is higher. Furthermore, by applying peak-combination HARP analysis, image artifacts caused by magnetic field inhomogeneities can be suppressed more effectively with line tagging data (30). With grid or lattice tagged data, the time between the read-out of two conjugate harmonic peaks is prolonged and time-dependent phase errors can not be eliminated by the peak-combination HARP method anymore.

In this work, a fast method for acquiring 3D CSPAMM data sets is proposed that allows to measure myocardial deformation of the entire left ventricle in three short breath-holds. The acceleration is achieved by splitting the acquisition into three orthogonally motion-encoded 3D measurements and by applying a localized tagging preparation in combination with a hybrid multi-shot, segmented Echo-Planar Imaging (EPI) sequence. Five healthy volunteers and five patients with myocardial infarction were examined using accelerated whole-heart 3D CSPAMM. Data were analyzed using a 3D extension of peak-combination HARP. In patients, hypokinetic regions were compared with scarred areas on late gadolinium-enhanced images.

2.2 Methods

Data acquisition

Three-dimensional CSPAMM was implemented using three volumetric data sets with line tagging preparation in three orthogonal directions on a 1.5 T MRI scanner (Achieva, Philips Medical Systems, Best, The Netherlands). For data acquisition, a modified hybrid multi-shot,

segmented EPI sequence was employed, with ramped flip angles to prevent tag fading during the cardiac cycle (14,23,49) (Figure 2.2).

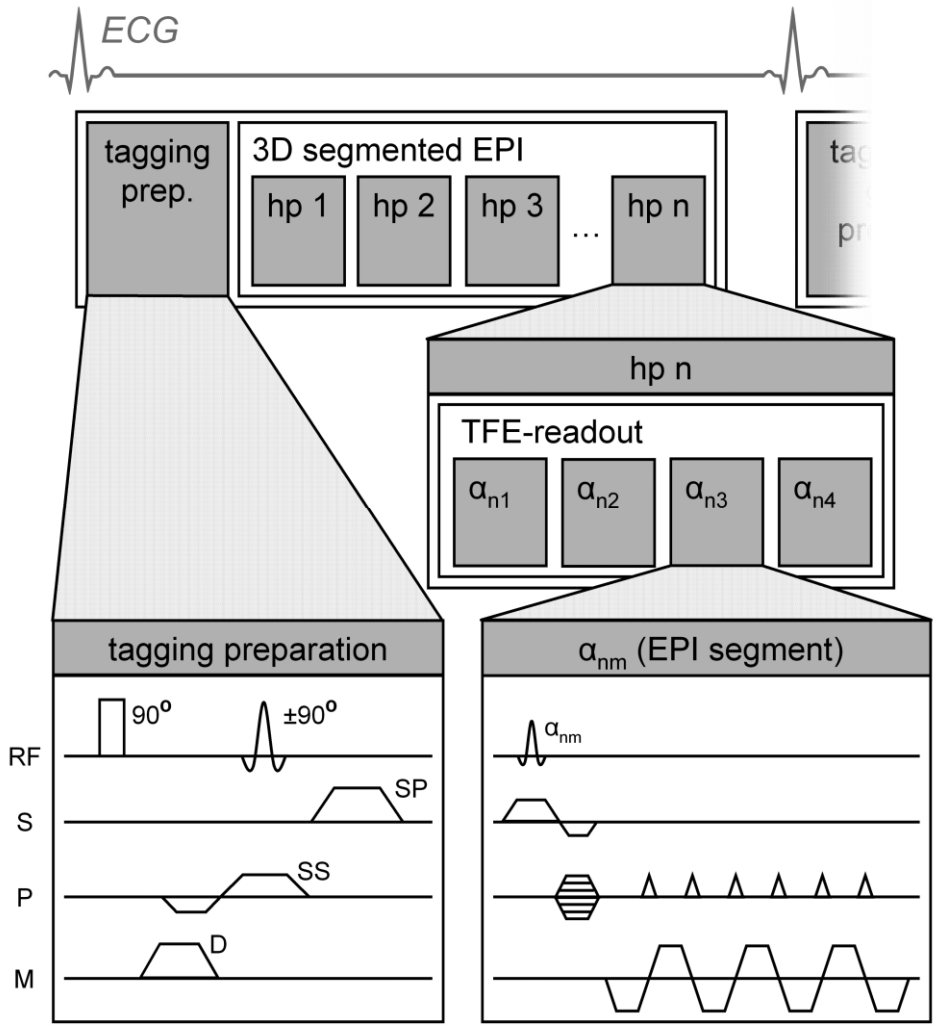

Figure 2.2: *Tagging sequence. The tagging preparation sequence is followed by a 3D hybrid multi-shot, segmented EPI read-out. By implementing the second RF pulse of the tagging preparation slice selectively, signal from outside a region of interest is suppressed after CSPAMM subtraction. The modified hybrid multi-shot, segmented EPI acquisition includes ramped flip angles α_{nm} to obtain a constant tagging contrast for each heart phase (hp) throughout the cardiac cycle (D: dephasing gradient; SP: spoiling gradient; SS: slice selective gradient; M: measurement direction; P: phase-encoding direction; S: slice-encoding direction).*

Further scan time reduction was achieved by incorporating a reduced field-of-view (FOV) method using localized tagging preparation (15). By implementing the second RF pulse of the tagging preparation selectively in the phase-encoding direction (Figure 2.2), only the magnetization within a region of interest is spatially modulated. Magnetization outside this region is equal for both CSPAMM measurements and is therefore suppressed after subtraction of the two complementary data sets. This allows reducing the FOV to the dimensions of the heart, in order to accelerate data acquisition without getting fold-over artifacts. For the second RF pulse of the tagging preparation, a sinc-gaussian RF pulse with a duration of 2.44ms and a bandwidth of 3.9 kHz was selectively applied in phase-encoding direction.

Imaging parameters of the hybrid multi-shot, segmented EPI sequence were as follows: FOV = 108x108x108mm^3, matrix size = 28x14x16, receiver bandwidth = 220 Hz/pixel, number of profiles per EPI segment = 7, number of excitations per heart phase = 4, echo time = 3.3ms. After Fourier transformation, 14 of 16 encoded slices were retained. A tag distance of 7mm was used, and the acquired voxel size in each of the three data sets with orthogonal tagging direction was 3.9x7.7x7.7mm^3. The read-out direction was aligned along the tagging direction in each of three measurements and the sequence was therefore rotated by 90° after each measurement. Accordingly, the highest resolution was achieved perpendicular to the tagging planes. Acquisition time per heart phase was 26.7ms. Depending on the heart rate, 19 to 25 time frames were recorded with a temporal resolution of 27ms to 37ms and a final flip angle of 19º to 25º. The first time frame was acquired 17ms after the R-wave of the ECG. For signal reception, a phased array coil consisting of five elements (two on the chest, three on the back) was used. Three breath-holds of 18 RR-intervals duration each were performed to acquire the data. To ensure comparable diaphragm position at the beginning of each breath-hold, a navigator echo located on the diaphragm was acquired before the acquisition of each data set. Data acquisition of the second and third tagging direction was only performed if the diaphragm position was within the same window of 4mm as at the beginning of the first acquisition (50). Enough time for recovery was admitted between consecutive breath-holds. The first two RR-intervals of each breath-hold were used to acquire the EPI reference data for phase correction. All data were zero-filled to a reconstructed voxel size of 0.96x1.93x1.93mm^3.

In order to compare motion patterns with areas of scar tissue in the infarct patients, late gadolinium-enhanced short-axis images were additionally acquired in all patients. A bolus of 0.25mmol/kg bodyweight of Gd-DTPA-BMA (Gadovist, Bayer Schering Pharma, Germany) was injected intravenously, and late gadolinium-enhancement short-axis images were

acquired after 10 minutes at the apical, the equatorial and the basal cardiac levels using an inversion recovery segmented gradient echo sequence with inversion time set to null normal myocardium (FOV = 350×350mm^2, pixel size = 1.5×1.5mm^2, repetition time = 7.4ms, echo time = 4.4ms, slice thickness = 8mm).

Study population

Five healthy volunteers (3 male / 2 female, 28.6 ± 5.5 years old) and five patients with myocardial infarction were examined. Clinical information on the patients is compiled in Table 2.1. Written informed consent from all study participants and institutional review board approval were obtained.

	Sex	Age [y]	HR [bpm]	EF [%]	MI location	MI date [days ago]
Patient A	female	83	65	43	anterior	30
Patient B	male	53	53	45	inferior	5
Patient C	male	59	73	50	inferior	2
Patient D	male	57	64	45	anterior	2
Patient E	male	59	73	56	anterior	8

Table 2.1: *Patient characteristics. For each patient, sex, age, heart rate (HR), ejection fraction (EF), location of myocardial infarction (MI) and time since MI are listed.*

Data analysis

For data post-processing of 3D tagging data a software tool designed for the analysis of two-dimensional tagging data (TagTrack, GyroTools Ltd., Zurich, Switzerland) was extended. To correct for phase errors from magnetic field inhomogeneities and to increase HARP accuracy, the peak-combination HARP method (30) was adapted to three dimensions and applied for contour tracking. A 3D spherical bandpass filter with smoothed boundaries was applied in *k*-space to obtain the HARP images. The spatial resolution after HARP filtering was 10x10x10mm^3, determining the spatial blurring of the displacement data (29). Eight to eleven midwall contours, consisting of multiple landmark points arranged in steps of about 5º, were defined on different short-axis slices regularly distributed over the left ventricle (C1-C10,

Figure 2.3). A time frame with good blood-myocardium contrast was chosen for contour definition. The contours were subsequently HARP tracked (16) in 3D space through all time frames.

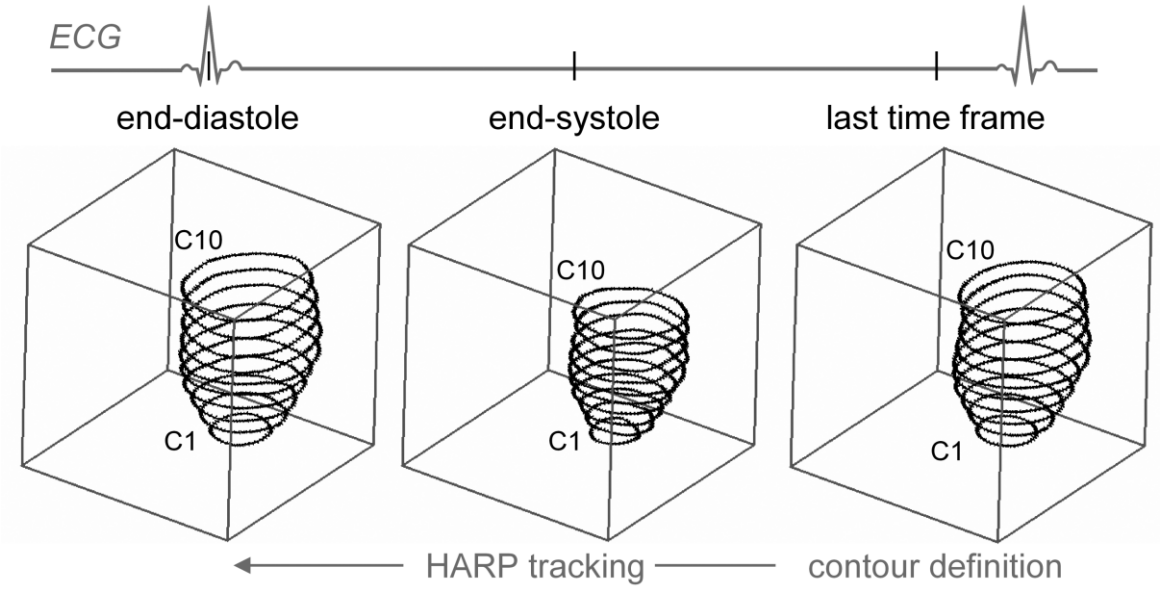

Figure 2.3: *Results from 3D peak-combination HARP tracking in a healthy volunteer. Ten midwall contours were defined regularly distributed over the left ventricle in a time frame with good blood-myocardium contrast. Tracking results are shown at end-diastole and end-systole. The contours were consecutively numbered from the apical (C1) to the basal (C10) cardiac level.*

The phase subtraction scheme employed in peak-combination HARP causes a doubling of the phase change per unit length. Similar as with tagging data acquired in long-axis view, tracking of landmark points becomes prone to phase aliasing due to fast movement in the long-axis direction during the rapid filling phase. Aliasing of the harmonic phase occurs when tissue motion between consecutive time frames becomes larger than the distance of two HARP wraps. Therefore, contour tracking was performed in two steps. In a first step, all contours were tracked using the conventional HARP method. In a second step, the peak-combined HARP image was used to re-adjust each landmark point to its corresponding (peak-combined) phase.

Circumferential shortening (*csh* in %) at each time frame was defined as the relative length change of a midwall contour with respect to the original length at end-diastole (first time

frame). For a more detailed analysis of *csh*, each midwall contour was divided into six sectors (S1-S6). S1 was defined in the septal wall; subsequent sectors were numbered consecutively in clockwise direction as viewed from the apex.

The time to maximum *csh* (T_{max}) was determined for the six sectors in all tracked contours. The standard deviation of T_{max} over all segments of the entire heart was calculated to reflect the degree of systolic dyssynchrony in patients.

For the obtained *csh* values of the healthy volunteers, average values over all subjects were calculated. In order to correct for different heart rates, temporal resolution and number of frames, the *csh* curves of all healthy volunteers were resampled and temporally normalized to end-systole. End-systole was defined as the moment of maximum *csh* averaged over the contours on all cardiac levels.

Statistics

The extracted myocardial motion parameters of the healthy volunteers, i.e. *csh* on different cardiac levels and in multiple sectors, were plotted as mean over time. Differences in the values at end-systole between different cardiac levels were compared with an analysis of variance (ANOVA) for repeated measurements followed by post-hoc testing for a linear trend (InStat, 3.01, Graph-Pad Software Inc., San Diego, USA). Differences in the standard deviations of T_{max} between patients and controls were compared using a two-tailed unpaired t test. P values < 0.05 were considered statistically significant.

2.3 Results

The 3D tagging measurements were successfully accomplished in all healthy volunteers and patients, and the breath-hold duration was well tolerated by all subjects. Selected time frames are shown in Figure 2.4 for a single slice out of each orthogonally line tagged 3D data set. At end-systole, tagline deformation due to myocardial contraction and rotation (first and second row) as well as a decreased tag distance due to longitudinal shortening of the left ventricle (lower row) can be observed. No fold-over artifacts are visible throughout the cardiac cycle despite the limited FOV.

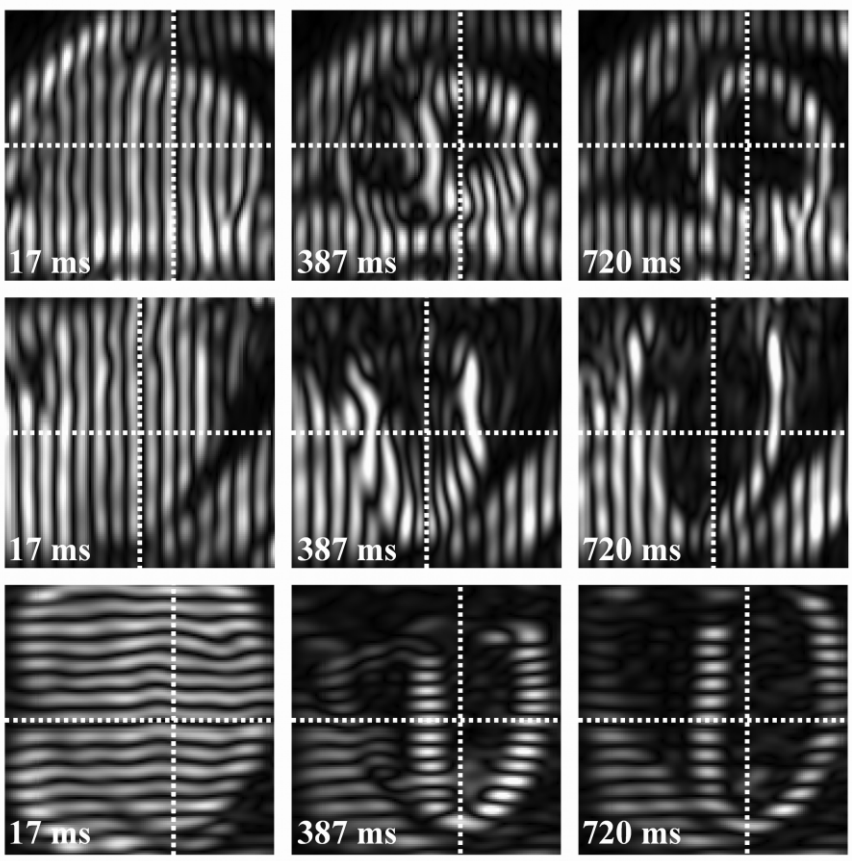

Figure 2.4: *Exemplary slices of tagged myocardium of a healthy volunteer for the three data sets with orthogonal tagging directions. The first (at end-diastole), the 11th (at end-systole) and the 20st (last) acquired time frame are shown. Cut through planes are indicated with dashed lines. The full FOV is shown.*

Three-dimensional isosurface representations, composed from the same three line tag prepared 3D data sets acquired in a healthy volunteer, are shown in Figure 2.5. The whole left ventricle is shown in contracted and relaxed state, i.e. at end-systole and at end-diastole. To improve visualization, cardiac levels were encoded on a color scale from red (base) to blue (apex). Circumferential contraction, longitudinal shortening and slight torsion between base and apex can be observed at end-systole when comparing the two 3D isosurface representations in Figure 2.5.

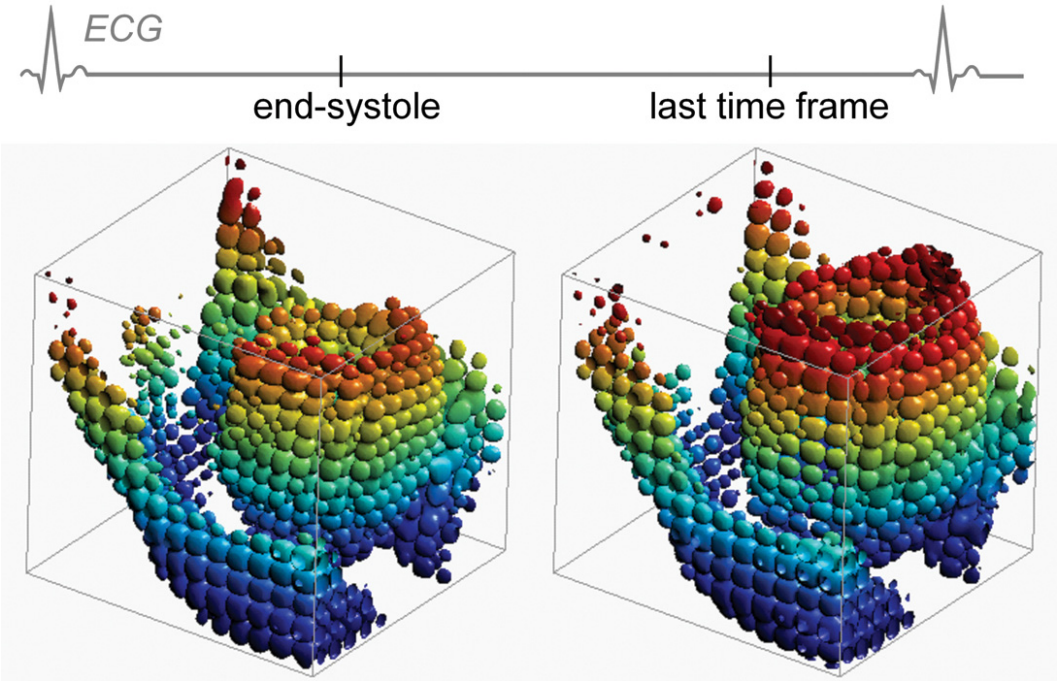

Figure 2.5: *3D isosurface representations of tagging data composed from three line tag 3D data sets showing the left ventricle of a healthy volunteer. Two selected time frames are shown: 387 ms (end-systole) and 720 ms (last acquired time frame) after the ECG R-wave. Color encoding corresponds to cardiac level.*

In all measured subjects, contours could be tracked throughout the cardiac cycle using the modified peak-combination HARP tracking method (Figure 2.3). No tracking errors due to HARP aliasing were observed visually in volunteers or patients. Figure 2.6a shows the time course of *csh* over the cardiac cycle for different cardiac levels of the left ventricle, averaged over all volunteers. Peak *csh* is most pronounced at the apex and decreases towards the base of the left ventricle. A fast relaxation during the rapid filling phase can be observed for all contours. Statistical analysis at end-systole resulted in little scattering of *csh* values on the same cardiac level among healthy subjects (standard deviations ranging from 0.94% to 2.70%). A highly significant variance in *csh* could be observed between different cardiac levels ($P<0.0001$), with a significant linear trend ranging from 14.1% at the base to 20.1% at the apex ($P<0.0001$). The contraction of different sectors (S1-S6) occurs simultaneously and with similar peak values of *csh* along the circumference of the left ventricle in healthy volunteers (Figure 2.6b). A tendency to higher c*sh* values in the free wall than in the septal wall could be observed.

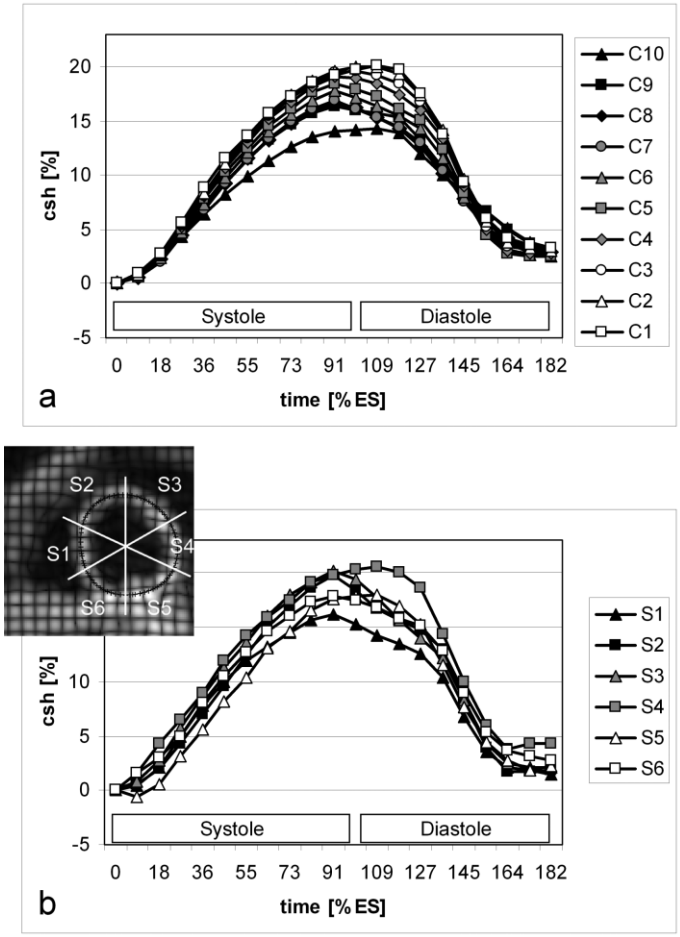

Figure 2.6: *Time curves of circumferential shortening (csh) averaged over all healthy volunteers. a) Csh for different cardiac levels (C1: apex, C10: base); b) Csh for six different sectors on the equatorial level (C5). Sector definition is given in the upper left corner. All data are normalized to end-systole (ES).*

Csh in a representative patient (patient C) with acute myocardial infarction after occlusion of the right coronary artery is reduced for the whole left ventricle (Figure 2.7a). Diastolic relaxation is prolonged compared to normal volunteer data. A highly heterogeneous contraction pattern is observed for different sectors at the level of infarction (Figure 2.7b). *Csh* is clearly reduced in sectors corresponding to the region of inferior myocardial infarction (S1 & S6). In sectors without infarction, myocardial contraction is not impaired and the *csh* values are similar to the ones measured in healthy volunteers. Peak *csh* occurs delayed in the cardiac cycle for sectors with infarcted tissue (Figure 2.7b, arrow).

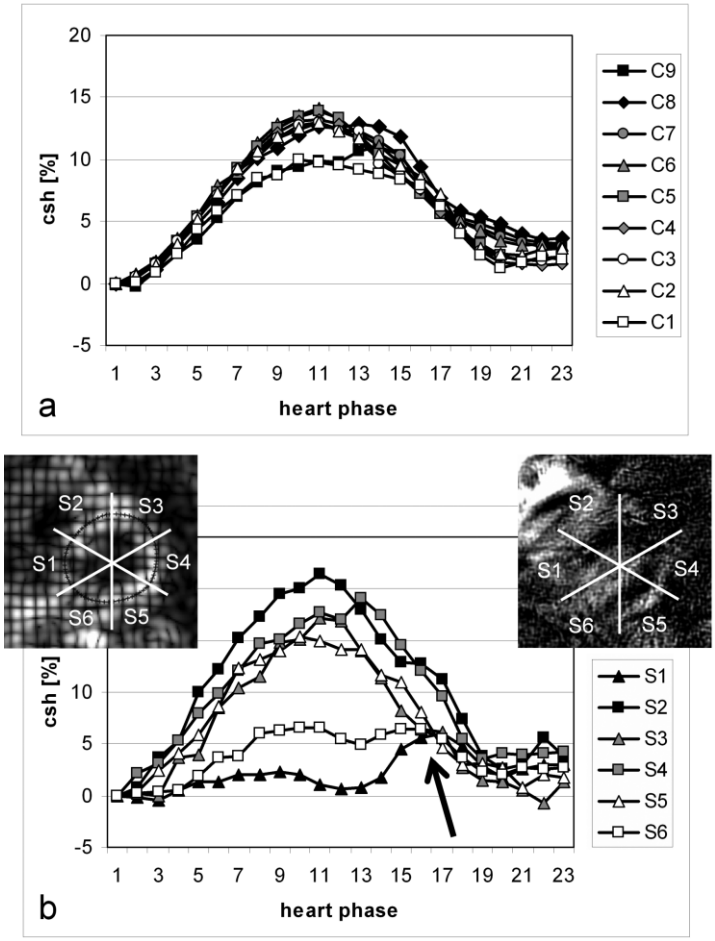

Figure 2.7: *Representative time curves of circumferential shortening (csh) for patient C. a) Csh for different cardiac levels (C1: apex, C9: base); b) Csh for six different sectors on the apical level (C2). Sector definition is given in the upper left corner. The corresponding late gadolinium-enhanced image of the same cardiac level is shown in the upper right corner. Sectors 1 and 6 demonstrate late and reduced csh. Post-systolic shortening can be observed for S1 (arrow).*

Figure 2.8 shows the late gadolinium-enhanced images of all five patients at the basal, the equatorial and the apical cardiac levels. For comparison of hyperenhanced areas with hypokinetic regions, bull's eye plots are shown for each patient representing *csh* at end-systole for the same cardiac levels. The apical cardiac level is located in the middle of each plot, the basal level at the periphery.

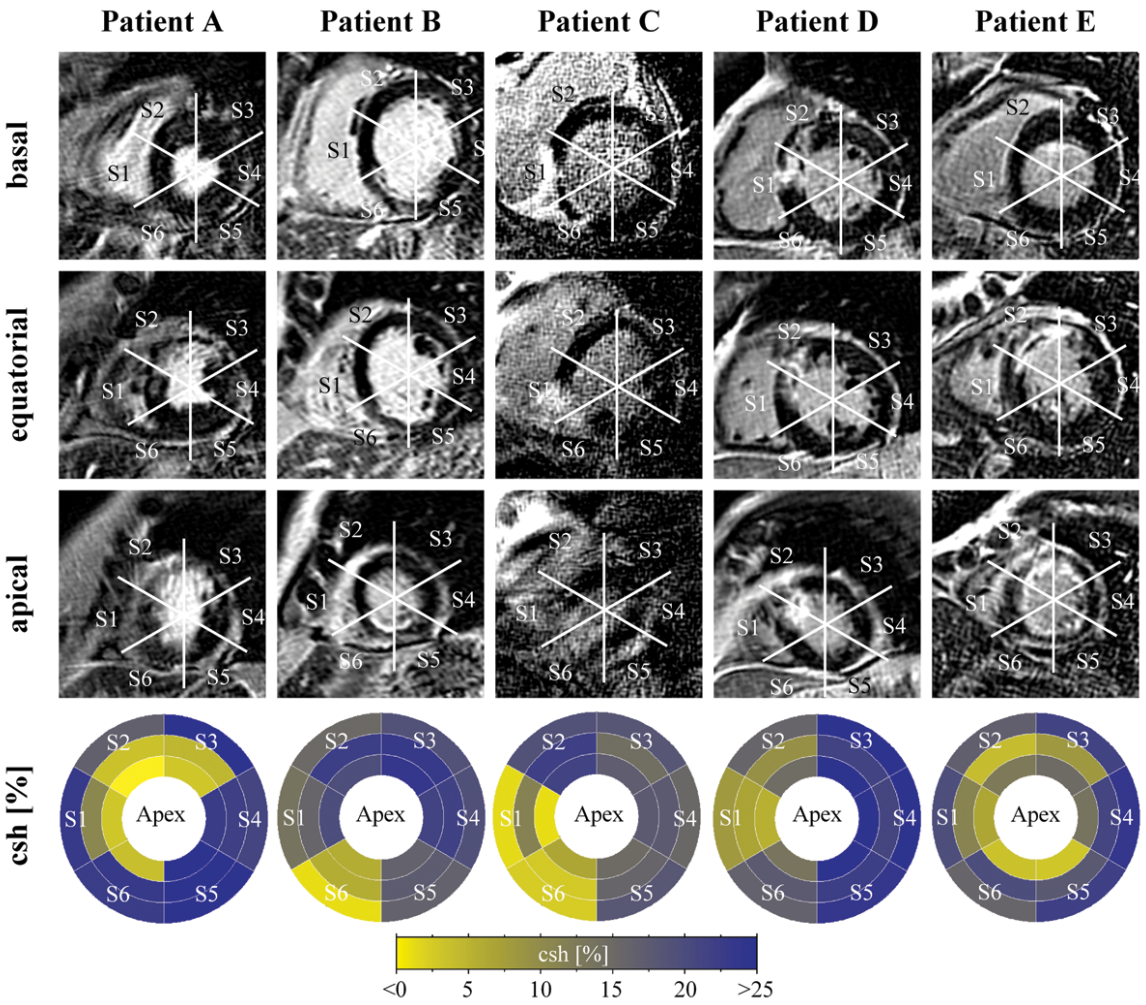

Figure 2.8: *Late enhancement images of each patient acquired 10 min after contrast injection on the apical, equatorial and basal cardiac levels. To compare regions exhibiting hyperenhancement with hypokinetic regions, a bull's eye plot of the circumferential shortening (csh) at end-systole is shown for each patient. The cardiac levels represented in the bull's eye plots (apex in the middle, base at the periphery) correspond to the slice levels of the late enhancement images. Sectors are defined from S1 to S6.*

Csh at end-systole is represented for each analyzed cardiac level in Figure 2.9. Bull's eye views are shown for one representative volunteer and for each patient. For the healthy volunteer myocardial contraction shows homogenously distributed values at end-systole for all cardiac levels and all sectors over the entire left ventricle. In all segments an end-systolic *csh* of more than 10% can be detected. The hypokinetic regions in the patients with

myocardial infarction correspond well with the locations of the infarctions (Table 2.1) and with regions exhibiting hyperenhancement (Figure 2.8).

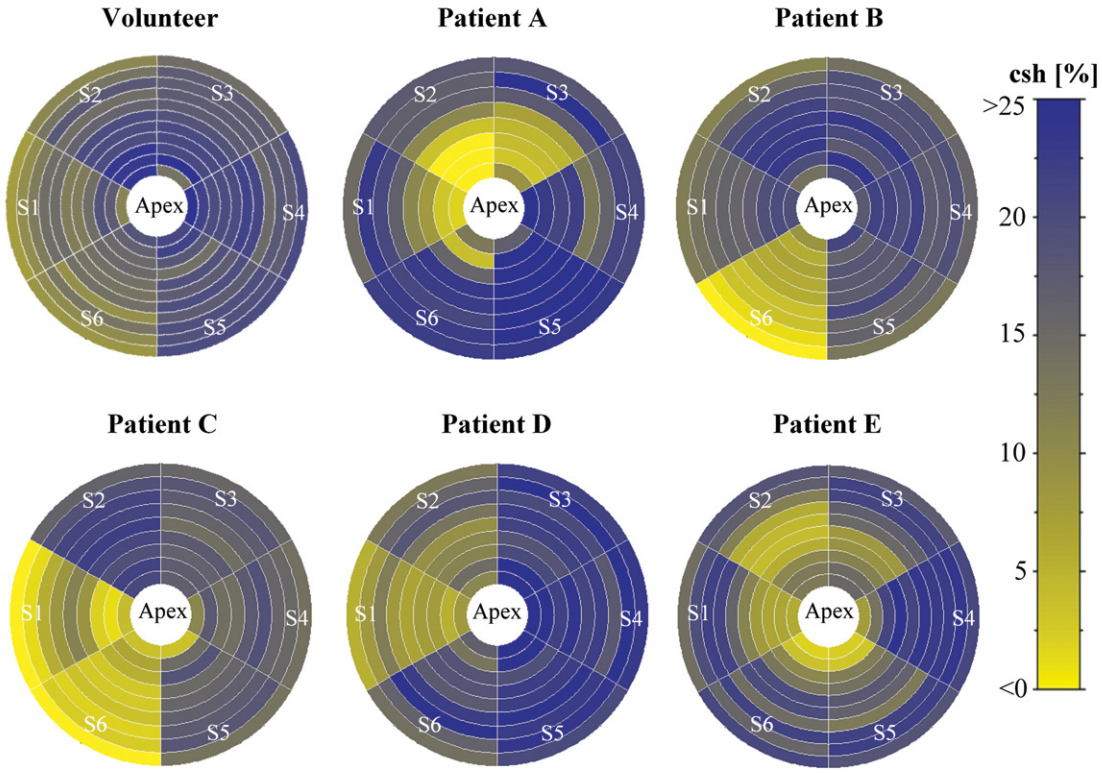

Figure 2.9: *Bull's eye plots showing the circumferential shortening (csh) at end-systole for one representative healthy volunteer and for each patient. The apical cardiac level is located in the middle of each plot, the basal level at the periphery. Sector definitions for patients are given in Figure 2.8, for the volunteer in Figure 2.6b.*

The time to maximum *csh* (T_{max}) averaged over all segments of the whole left ventricle was not different between patients (359.0 ± 15.8ms) and volunteers (354.8 ± 39.1ms). However, the standard deviation of T_{max}, assumed a measure of left ventricular dyssynchrony, was significantly ($P<0.01$) higher for patients (77.8 ± 11.4ms) than for controls (43.7 ± 5.6ms).

2.4 Discussion

In this work, an accelerated approach to true 3D motion tracking has been proposed. Increased scan efficiency relative to previous methods was achieved by sequentially acquiring

three volumetric data sets with orthogonal line tagging preparation rather than a single lattice tagged volume and by incorporating reduced field-of-view imaging and a fast hybrid multi-shot, segmented EPI read-out. As a result, 3D CSPAMM data could be acquired in three breath-holds of 18 heartbeats duration each. The procedure was well tolerated by healthy volunteers and by patients with recent myocardial infarction. By applying a modified tracking method, robust tracking results could be achieved with peak-combined HARP data even in regions with fast motion.

Applying the proposed method, 3D CSPAMM data with comparable spatiotemporal resolution and coverage can be acquired approximately four times faster than with previous methods (48). Since only six instead of eight harmonic peaks are acquired with the proposed method, scan time is inherently reduced by 25%. The use of the localized tagging preparation sequence allows reducing the FOV to the dimensions of the heart without getting fold-over artifacts. Thereby, scan time is further reduced by approximately 60%, depending on the size of the heart relative to body dimensions. By prolonging the acquisition time per heart phase employing a hybrid multi-shot, segmented EPI read-out, another 25% reduction in scan time is achieved compared to a segmented EPI read-out as used in (48). In total, measurement time was reduced to $0.75 \times 0.4 \times 0.75 \times 100\% = 22.5\%$ relative to the previous 3D tagging approach (48). Since the first two heartbeats of each breath-hold were used to acquire EPI reference data, the actual reduction of scan time was slightly lower than 22.5% in practice. Therefore, an overall acceleration of a factor of four was achieved using the proposed acquisition scheme compared to the previous method (48).

The presented technique exhibits limitations when assessing motion of very thin structures such as the right ventricle or remodeled post-infarct scar tissue. This is related to the limited spatial resolution leading to partial volume effects and differences in EPI related image distortions between the three line tag encoded data sets. Additionally, signal in fast moving regions of the heart might be blurred due to motion during the multishot, segmented EPI read-out. These effects can lead to tracking errors and signal cancellations when applying thresholds or rendering isosurface plots. For example, by the application of a global threshold in Figure 2.5, optimal isosurface plots are generated for the left ventricle, whereas the right ventricle is hardly visible. The problem could be addressed by applying a higher spatial resolution and a shorter EPI echo-train, at the cost of a longer scan time resulting in more breath-holds. The longer measurement time may, however, cause image artifacts if changes in heart rate or patient movement occur during the prolonged data acquisition.

By aligning the measurement direction with the tagging modulation direction during the acquisition of each orthogonally encoded data set, errors in determining the center frequency f_0 might affect the sequence, leading to mutual spatial shifts of the acquired volumes. To prevent such spatial mismatches between the three data sets, the line tagged volumes could be manually shifted during post-processing. With the data presented in this work, misregistration of the line tagged volumes was of negligible magnitude and no shifting was necessary.

With a tag distance of 7mm and HARP filtering, the spatial resolution of the displacement data obtained in this study was 10x10x10mm^3. In HARP analysis of CSPAMM data, the maximum possible radius of the band pass filter equals the distance between the center of *k*-space and the first harmonic peak. This filter size would result in a spatial resolution of the measured displacement data that is identical to the tag distance. Due to the presence of residual DC signal and noise, the radius of the HARP filter is usually chosen smaller than the theoretically largest radius. Hence, for tagging studies applying CSPAMM, the final spatial resolution of derived displacement parameters is usually less than the tag distance. When SPAMM is used, the filter radius has to be chosen even smaller given the presence of a strong DC signal in later heart phases as a result of T1 relaxation. In this study, spatial resolution in the displacement data was similar as in previous two-dimensional tagging methods applying a tag distance of around 8mm (51-53). To improve the spatial resolution of the displacement data, a smaller tag distance combined with a higher spatial resolution of the acquired data would have to be applied. As more wraps would occur in the harmonic phase, temporal resolution would also have to be improved to prevent HARP aliasing. Thus, in addition to a smaller voxel size, decreased flip angles per heart phase would have to be applied, compromising signal-to-noise ratio additionally.

Comparable diaphragm positions in each of the three breath-holds were ensured by the use of a navigator shot at the beginning of each line tagging acquisition (50). In some patients several breath-hold attempts were necessary due to inconsistent end-expiratory levels. In future work, the acceptance rate may be increased by widening the navigator acceptance window and shifting the acquisition volume by a certain distance at the same time. Drifts in breath-hold position during data acquisition are not corrected for using this method and image artifacts occur if CSPAMM subtraction fails using two non-corresponding data sets. Along the same line, fold-over artifacts may arise when applying localized tagging preparation.

In this study, significant differences of end-systolic *csh* were detected between different cardiac levels in healthy volunteers. *Csh* was greatest apically and less towards the base. Additionally, *csh* calculations for controls tended to result in greater peak values in the lateral

wall than in the septum. These results are consistent with findings from previous studies applying two-dimensional tagging (54,55).

In patients with myocardial infarction, hypokinetic regions could be well localized and correlated with scar tissue, i.e. regions exhibiting late hyperenhancement. Analysis of time to peak *csh* resulted in more scattering among heart segments in patients than in healthy volunteers. This finding indicates left ventricular dyssynchrony for patients due to post-systolic shortening of infarcted tissue (51,56). Together with MR derived viability information, this approach shows potential to quantify dyssynchrony of the entire left ventricle and to predict individual responsiveness to cardiac resynchronization therapy. In order to capture cardiac regions with possible deformation impairments using two-dimensional tagging techniques, multiple slices covering the entire left ventricle need to be acquired, if no prior information concerning the location(s) of diseased cardiac tissue is available. Applying the proposed 3D CSPAMM acquisition method, this lengthy procedure can be shortened considerably and problems due to slice misregistration are avoided.

A large variety of parameters describing cardiac deformations can be extracted from the acquired 3D tagging data sets. *Csh* and time to maximal *csh* were examined in this initial study. Examples of other parameters that proved to be important in previous studies (17,57-59) are rotation, left ventricular torsion, longitudinal shortening as well as their derivatives describing velocities.

2.5 Conclusions

An accelerated 3D tagging acquisition method has been proposed enabling assessment of 3D motion information with whole heart coverage in three short breath-holds. Compared to previous 3D methods requiring multiple extended breath-holds and considerable cooperation, the present approach is well tolerated by patients. A large variety of information can be extracted from the acquired motion encoded volumes to describe cardiac deformation in healthy and diseased hearts. The technique promises applicability in larger studies and in patients allowing further insight into cardiac mechanics of various diseases.

Chapter 3:

Cardiac Motion in Patients with Fabry Disease

3.1 Introduction

Fabry disease is an X-linked inherited deficiency of the lysosomal enzyme α-galactosidase. This deficiency leads to progressive intracellular accumulation of glycosphingolipids in various tissues. Left ventricular (LV) hypertrophy (LVH) is the hallmark of cardiac manifestations in affected patients, worsening with age and sometimes leading to death (60).
Before the availability of enzyme replacement therapy (ERT) myocardial involvement of Fabry disease was monitored by ultrasound using functional (ejection fraction, EF) and volumetric (hypertrophy) parameters. Echocardiography based on Doppler imaging has shown changes in regional motion patterns such as reduced myocardial contraction and relaxation velocities in Fabry patients with LVH (61,62). Similar regional motion abnormalities were found to a lesser extent in non-hypertrophic hearts of Fabry patients (62). Echocardiographic measurements, however, have several limitations. A poor acoustic window and through-plane motion (up to 2 cm at the basal level in healthy volunteers (63)) due to systolic shortening, can significantly compromise the measured results.
Previous Cardiac Magnetic Resonance (CMR) tagging studies have shown that parameters such as LV rotation and torsion are important for the characterization of cardiac motion in patients with LV hypertrophy in hypertensive heart disease (17,64). Since volumetric and functional changes occur late in the natural course of Fabry disease and do not change rapidly under ERT, a sensitive imaging modality is needed to capture subtle changes in cardiac motion. CMR imaging with myocardial tagging was therefore thought to be a valuable and feasible alternative imaging method. The purpose of the present study was to prospectively test the hypothesis that CMR imaging can detect abnormal myocardial motion not only in Fabry patients with severe LV hypertrophy but also in patients without macroscopic cardiac involvement, i.e. in patients with a normal LV mass.

3.2 Methods

Study population

Twenty-nine patients with Fabry disease underwent CMR imaging as part of their routine diagnostic work-up. For comparison, twenty-nine age and sex matched healthy volunteers

underwent the same imaging procedure. Written informed consent from all subjects and institutional review board approval were obtained.

The study population consisting of 29 subjects (17 male, 12 female) with genetically confirmed Fabry disease (FD) was grouped as follows: 16 patients with normal LV mass (FD_{normal}) and 13 patients with LV hypertrophy (FD_{LVH}). The cutoff for LVH was defined gender dependently by increased LV mass normalized to body surface area, as described in (65). The mean age of all Fabry patients was 37.6 years with a standard deviation (SD) of 12.8 years. All patients except six females without LVH and two males with LVH received ERT at the time of the measurement. More detailed characteristics of the patient groups are given in Table 3.1.

	FD_{normal}	FD_{LVH}
men/women	6/10	11/2
age [years]	32.3 ± 11.6	44.2 ± 11.3
weight [kg]	61.1 ± 10.2	66.8 ± 9.6
heart rate [bpm]	61.8 ± 8.9	61.7 ± 10.0
LV mass [g]	94.1 ± 19.7	180.5 ± 52.5
LV mass / BSA [g/m^2]	55.3 ± 9.6	100.5 ± 24.3
SV [ml]	79.3 ± 16.9	110.9 ± 31.6
EF [%]	63.6 ± 7.7	70.4 ± 7.2
ERT	10	11
ERT duration [yrs]	2.1 ± 0.8	1.9 ± 0.8

Table 3.1: *Characteristics of Fabry patients. For each group of patients, the following characteristics are given: number of measured male and female individuals, age, weight, heart rate, left ventricular (LV) mass, LV mass normalized to body surface area (BSA), LV stroke volume (SV), ejection fraction (EF), number of subjects that underwent enzyme replacement therapy (ERT) at time of measurement and duration of ERT. All values are given as mean ± 1 SD.*

A control population of 29 age and sex matched healthy volunteers (17 male, 12 female) was examined for comparison and grouped corresponding to each group of Fabry patients with (Vol_{c_LVH}) and without LVH (Vol_{c_normal}). None of the volunteers showed LVH or had a known history or signs of cardiovascular disease. The mean age of all control subjects was 37.5 with a SD of 12.5 years (32.3 ± 11.1 years for Vol_{c_normal} and 43.9 ± 11.8 years for Vol_{c_LVH}).

Data acquisition

For planning purposes and to determine the timing of mitral valve opening, a four-chamber view was acquired with a steady state free precession (SSFP) sequence (25 cardiac phases and a temporal resolution of about 30ms depending on the heart rate).

To assess LV mass in patients with Fabry disease, multi-slice short-axis SSFP datasets covering the entire left ventricle were acquired as described in (65), with 25 heart phases per cardiac cycle.

For the quantification of LV circumferential shortening, rotation and torsion, short-axis Complementary Spatial Modulation of Magnetization (CSPAMM) (14) images were acquired in all subjects on apical, midventricular and basal cardiac levels. The exact slice level locations were determined by dividing the distance between the level of the mitral annulus and the epicardial contour of the apex into four equal segments on the four-chamber SSFP scan. Three parallel CSPAMM slices were then positioned orthogonally to each of the three inner segment borders. In order to compensate for through-plane motion, a slice following technique (15) was applied, and an optimized ramped flip angle approach was used to prevent tag fading during the cardiac cycle (14,23). Two tagged cine image series with orthogonal one-dimensional stripe patterns and 8mm tag distance were acquired in one breath-hold on a 1.5 T MRI scanner (Gyroscan Intera, Philips Medical Systems, Best, The Netherlands). The imaging parameters of the EPI sequence were as follows: slice thickness: 8mm, EPI factor: 11, FOV: 330x264mm^2, matrix: 128x33. Depending on the heart rate, approximately 20 frames were recorded with a temporal resolution of 25-35ms and a final flip angle of around 20º. For signal reception, a phased array coil consisting of five coil elements (two on the chest, three on the back) was used.

LV long-axis shortening during the cardiac cycle was assessed in a subset of 20 patients with Fabry disease vs. the same number of age and sex matched healthy volunteers. Six patients exhibited LVH (4 males) and 14 had normal LV mass (5 males). CSPAMM images were acquired in four-chamber view orientation with identical scan parameters as above.

Additionally, late gadolinium enhanced images with inversion time set to null healthy myocardium were acquired 10 min after contrast injection in all patients.

Data analysis

All data were analyzed with Harmonic Phase analysis (HARP) (16) using an in-house software tool (TagTrack, GyroTools Ltd., Zurich, Switzerland). To compensate for phase

errors due to patient induced magnetic field inhomogeneities and to increase HARP accuracy, peak-combination HARP (30) was applied. Since phase errors additive to both harmonic peaks are eliminated by peak-combination HARP, phase contributions originating from different coil locations are inherently compensated for as well. Hence, peak-combined HARP images of different coil elements could be combined in a straightforward fashion during post-processing to achieve a more homogeneous quality of the HARP images across the field of view. With a tag distance of 8mm and HARP filtering, the spatial resolution of the obtained displacement data was approximately 13x13mm^2 (29).

The endo- and epicardial borders were semi-automatically determined in a time frame without visible artifacts and with good blood-myocardium contrast, i.e. at later heart phases, as described in (49). A centerline consisting of 72 regularly distributed landmark points was calculated (Figure 3.1A). The centerline was subsequently HARP tracked through all time frames. Circumferential shortening (CSh in %) at each time frame was defined as the relative length change of the centerline with respect to the original length at end-diastole (first time frame).

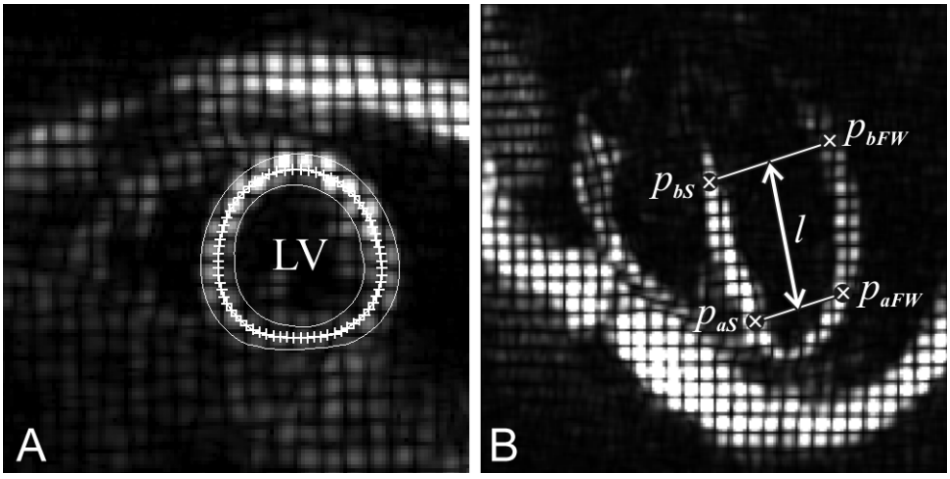

Figure 3.1: *Definition of landmark points for HARP tracking on CSPAMM images of a healthy volunteer: A) LV short-axis image with a midwall contour centered between the semi-automatically identified myocardial borders (thin lines). B) Measurement of LV long-axis shortening on a four-chamber view image. For each of the base and the apex, landmark points on the septum (p_{bS}, p_{aS}) and the free wall (p_{bFW}, p_{aFW}) were identified for tracking. From their actual locations, l was calculated in order to determine LV long-axis shortening.*

The rotation angle of the centerline was calculated for each acquired heart phase by determining the average difference between the actual angles of all points on the centerline and the corresponding original angles at end-diastole. Both the circumferential shortening and the rotation angle were calculated according to the detailed descriptions given in (51).

Furthermore, the relative global torsion ϕ (in deg/cm) of the left ventricle was determined for each heart phase *hp* by subtracting the rotation angle φ of the centerline at the basal slice from the rotation angle at the apical slice. The result was then divided by the distance *d* (in cm) between the two acquired slices for normalization purposes:

$$\phi(hp) = \frac{\varphi_{apex}(hp) - \varphi_{base}(hp)}{d} \qquad [1.13]$$

The maximal diastolic untwisting velocity of the apex and the maximal torsional recoil velocity of the left ventricle during diastole were determined by calculating the temporal derivatives of the rotation angle and the torsion.

For the analysis of LV long-axis shortening (LAS, in %), HARP tracking was applied to landmark points located at the apical and the basal level of the septum (p_{aS}, p_{bS}) and the free wall (p_{aFW}, p_{bFW}) (Figure 3.1B). The apical and the basal levels used were identical to the levels at which the tagged short-axis images were acquired. From the locations of the four landmark points, LAS was calculated as the relative length change of *l* (Figure 3.1B) with respect to the length at the end-diastolic time frame:

$$l(hp) = \sqrt{\left(\frac{x(p_{bS},hp)+x(p_{bFW},hp)}{2} - \frac{x(p_{aS},hp)+x(p_{aFW},hp)}{2}\right)^2 + \left(\frac{y(p_{bS},hp)+y(p_{bFW},hp)}{2} - \frac{y(p_{aS},hp)+y(p_{aFW},hp)}{2}\right)^2} \qquad [1.14]$$

$$LAS(hp) = \left(1 - \frac{l(hp)}{l(hp=0)}\right)\cdot 100\% \qquad [1.15]$$

In order to correct for different heart rates, temporal resolution and number of frames, all circumferential shortening, rotation, torsion and LAS curves were resampled and temporally normalized to end-systole (ES). Due to irregular time courses of LV contraction in some of the patients, end-systole was defined relative to the moment of mitral valve opening determined on the SSFP four-chamber images.

Statistics

The extracted myocardial motion parameters were plotted as mean ± SD. Differences in the peak values of the measured motion parameters between each group of patients with Fabry disease (FD_{normal}, FD_{LVH}) and the corresponding group of volunteers (Vol_{c_normal}, Vol_{c_LVH}) were compared with an analysis of variance (ANOVA) followed by Bonferroni post-hoc testing (InStat, 3.01, GraphPad Software Inc., San Diego, USA). Rotation values at the basal and the midventricular levels were assessed at peak apical rotation. Additionally, to test motion parameters for dependencies on LV mass normalized to body surface area, linear regressions were calculated. P-values <0.05 were considered statistically significant.

3.3 Results

The time interval between the R-wave (ECG) and the opening of the mitral valve (as determined on the SSFP four-chamber view images) was 420.2±36.5ms for Fabry patients without LVH and 448.7±30.3ms for patients with LVH. In the volunteers values were 455.9±38.6ms for the group corresponding to patients without LVH (Vol_{c_normal}) and 430.1±49.8ms for the group corresponding to patients with LVH (Vol_{c_LVH}). By calculating the average moment of peak LV contraction in the volunteers, end-systole was defined as 83% of the time interval between the R-wave of the ECG (end-diastole) and mitral valve opening.

Table 3.2 lists the maximum deformation parameters for each examined group of patients and volunteers. Due to inaccurate planning of the basal slice in two patients with LVH, the statistical data of the corresponding results (basal circumferential shortening, basal rotation, torsion) are reduced by two subjects. None of the patients except one female with LVH exhibited late gadolinium enhancement. In this patient, the scarred region amounted to only 1.4% of the total LV myocardial volume, and no regional motion abnormalities could be observed in the affected area as compared to regions with healthy tissue.

	FD_{normal}	FD_{LVH}	Vol_{c_normal}	Vol_{c_LVH}
LAS [%]	19.3 ± 1.8	12.5 ± 2.5***	19.8 ± 1.8	18.7 ± 1.1
apical CSh [%]	24.9 ± 2.3	19.9 ± 4.6*	23.5 ± 2.2	22.9 ± 2.0
equatorial CSh [%]	22.9 ± 2.0	19.7 ± 2.5	21.3 ± 2.1	21.5 ± 1.7
basal CSh [%]	21.2 ± 2.0*	18.0 ± 2.6	19.3 ± 1.9	19.6 ± 1.6
apical rot [deg]	12.9 ± 2.6**	13.3 ± 3.0**	9.8 ± 2.2	10.1 ± 3.2
equatorial rot † [deg]	5.4 ± 2.0	4.1 ± 1.8	4.3 ± 1.8	5.1 ± 2.7
basal rot † [deg]	-0.2 ± 3.0	-1.8 ± 2.3	-0.4 ± 2.6	0.5 ± 2.2
torsion [deg/cm]	3.3 ± 0.6***	3.2 ± 0.8*	2.3 ± 0.5	2.5 ± 0.5

Table 3.2: *Maximum LV deformation values for Fabry patients and volunteers. Maximum values of long-axis shortening (LAS), circumferential shortening (CSh), rotation (rot) and torsion are listed for the left ventricle. All values are indicated as mean ± 1 SD. † For the equatorial and the basal cardiac levels, rotation at maximum apical rotation was compared. * P<0.05, ** P<0.01, *** P<0.001 vs. corresponding group of volunteers.*

The time courses of LV long-axis shortening and apical circumferential shortening averaged over each group of patients and volunteers are displayed in Figure 3.2 (error bars represent 1 SD in all figures). Fabry patients without LVH did not exhibit changes in LV long-axis shortening (Figure 3.2A). In contrast, peak long-axis shortening was impaired in the group of Fabry patients with marked LVH with high significance (P<0.001, Figure 3.2B) when compared to healthy volunteers. While the circumferential shortening of the left ventricle showed an increased mean peak value at the basal cardiac level for patients prior to developing LVH (P<0.05, Figure 3.2C), LV contraction was significantly impaired at the apical level (P<0.05) for patients with LVH compared to the healthy controls (Figure 3.2D).

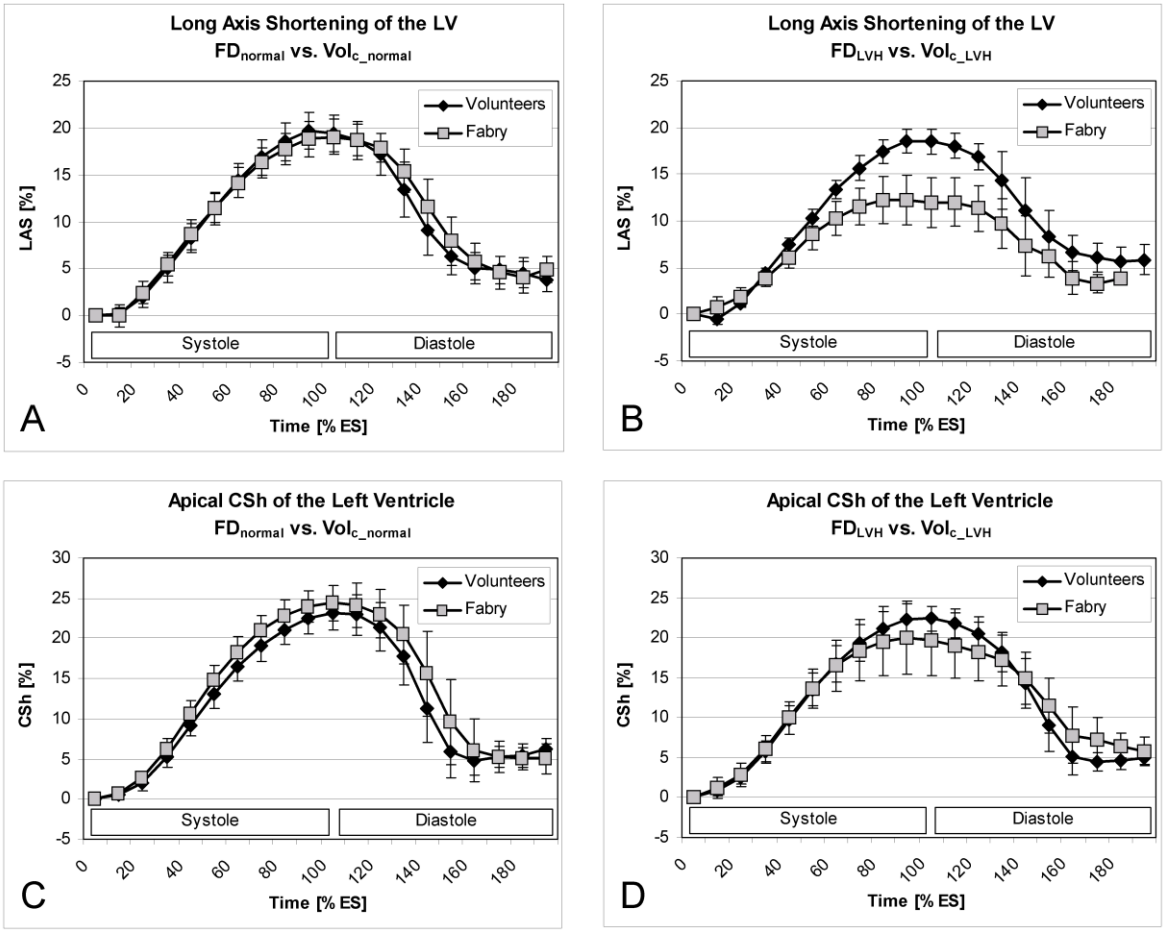

Figure 3.2: *Time curves of LV long-axis shortening (LAS) and circumferential shortening (CSh) over the cardiac cycle normalized to end-systole (ES). Patients with Fabry disease are compared with the corresponding group of volunteers: A, B) LV LAS; C, D) LV apical CSh. While no changes can be observed for patients without LV hypertrophy, significant differences are noticeable around ES for patients with LV hypertrophy. Error bars represent 1 SD in all figures.*

Linear regression analysis of peak LV long-axis shortening in all Fabry patients against LV mass normalized to body surface area resulted in a significant decrease of LV long-axis shortening with increasing LV mass, as shown in Figure 3.3 (slope significantly different from zero ($P<0.001$) and $R^2 = 0.5885$). Furthermore, Figure 3.4 shows a significant linear dependency in Fabry patients between decreasing LV circumferential shortening and increasing LV mass normalized to body surface area (slope different from zero with $P<0.001$, 0.01, 0.05 and $R^2 = 0.3372$, 0.2956, 0.2019 for the apical, equatorial and basal level, respectively).

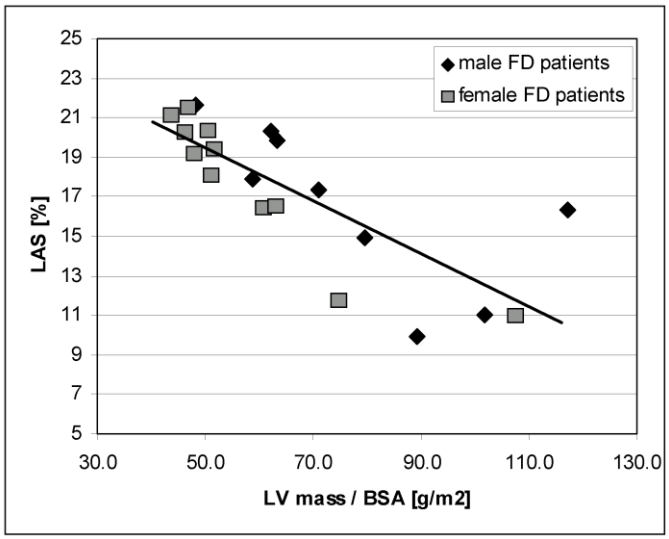

Figure 3.3: *Peak LV long-axis shortening (LAS) against LV mass normalized to body surface area (BSA) in all patients with Fabry disease. LV LAS is reduced for increasing LV mass / BSA with* $y = -0.1345x + 26.207$ *and* $R^2 = 0.6203$.

In Figure 3.5, apical rotation and LV torsion normalized to ES and averaged over all group subjects are represented over time. Maximum rotation of the left ventricle was significantly increased at the apical level of the Fabry hearts with normal LV mass ($P<0.001$, Figure 3.5A). Similarly, in Fabry patients with LVH, the differences in rotation values at the apex were more pronounced when compared with the controls ($P<0.001$, Figure 3.5B). Altered peak values for the relative global torsion of the left ventricle were found in both groups of patients. Compared to healthy volunteers, highly significant differences were obtained with $P<0.001$ for patients without LVH and $P<0.05$ for patients with LVH (Figure 3.5C, D). Linear regression resulted in no significant dependencies of rotation or LV torsion on LV mass normalized to body surface area. In Fabry patients with normal LV mass who did not receive ERT, apical rotation was 13.6 ± 1.9 deg, compared to 12.4 ± 2.9 deg in patients without LVH under ERT (non-significant difference). In contrast, LV torsion was significantly reduced in patients without LVH under ERT compared to patients with normal LV mass who did not receive ERT ($P<0.05$, 3.0 ± 0.6 deg/cm and 3.7 ± 0.4 deg/cm, respectively).

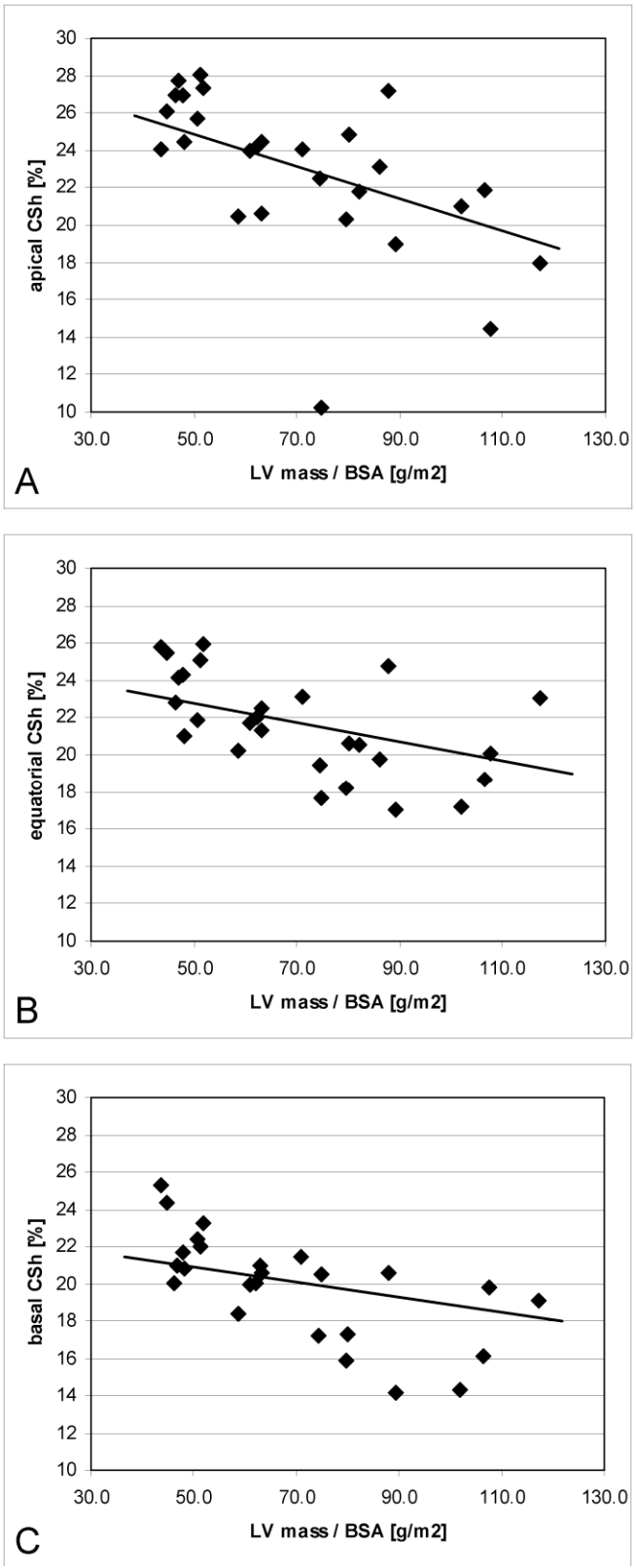

Figure 3.4: *Circumferential shortening (CSh) against LV mass normalized to body surface area (BSA) in all patients with Fabry disease. CSh is reduced for increasing LV mass / BSA. A) Apical cardiac level. y = -0.0861x + 29.142, R^2 = 0.3372. B) Equatorial cardiac level. y = -0.0516x + 25.377, R^2 = 0.2956. C) Basal cardiac level. y = -0.0416x + 23.022, R^2 = 0.2019.*

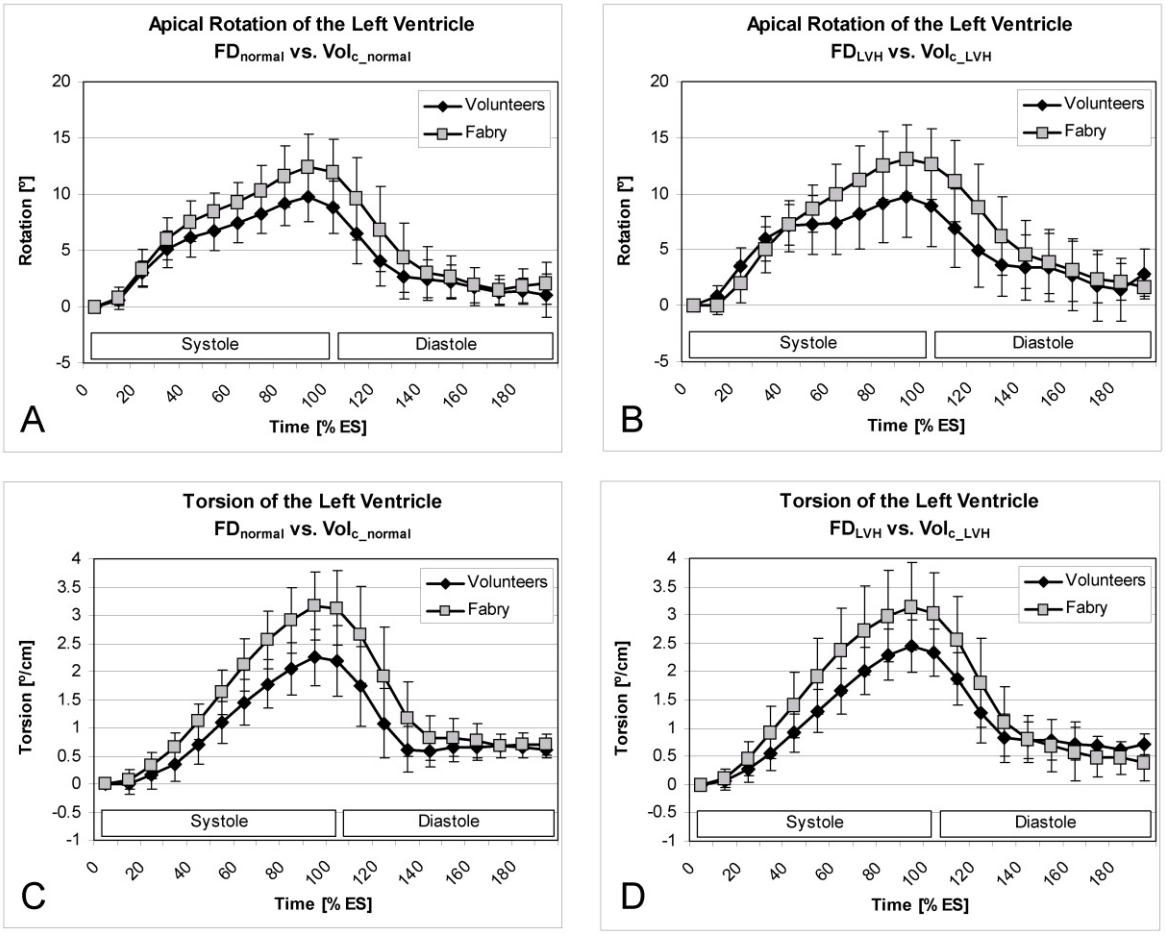

Figure 3.5: *Time curves of LV apical rotation and relative global torsion over the cardiac cycle normalized to end-systole (ES). Patients with Fabry disease are compared with the corresponding group of volunteers: A, B) LV apical rotation; C, D) LV torsion. Significant changes can be noticed not only in Fabry patients with LV hypertrophy but also in patients without LV hypertrophy. Error bars represent 1 SD in all figures.*

Table 3.3 compares the maximum absolute temporal derivatives of the measured rotation and torsion values during diastolic untwisting. Maximum LV rotation velocity at the apex was significantly ($P<0.01$) increased during diastole in the group of Fabry patients with normal LV mass. Similarly, statistical analysis resulted in a significantly faster LV unwinding velocity during the rapid filling phase for patients without LVH compared to healthy controls ($P<0.001$). A trend towards higher diastolic untwisting velocities could also be observed for Fabry patients with increased LV mass.

	FD_{normal}	FD_{LVH}	Vol_{c_normal}	Vol_{c_LVH}
apical rot [deg/s]	105.8 ± 42.5**	85.8 ± 13.9	75.1 ± 16.3	75.0 ± 21.5
torsion [deg/cm·s]	28.4 ± 8.4***	24.2 ± 2.2	19.5 ± 5.3	19.1 ± 4.6

Table 3.3: *Maximum LV untwisting velocities during diastole. Peak diastolic untwisting velocities are listed for the rotation (rot) of the apex and LV torsion. All values are indicated as mean ± 1 SD. * $p < 0.05$, ** $p < 0.01$, *** $p < 0.001$ vs. corresponding group of controls.*

3.4 Discussion

The accuracy of echocardiographic techniques such as tissue Doppler imaging or speckle tracking echocardiography is adversely affected by through-plane motion effects, most pronounced at the basal level of the heart (7). This limitation is effectively eliminated with slice-following CSPAMM. The technique also avoids the problems arising from poor acoustic windows and the difficulties relating to the reproducibility of ultrasound scan plane selection.
Using CSPAMM and peak-combination HARP, a variety of myocardial deformation parameters can be quantified rapidly and with minimal user interaction. Recently introduced techniques such as peak-combination HARP and semi-automatic definition of landmark points allow for a more accurate and faster assessment of myocardial motion patterns and increase the reproducibility of the examined parameters (30,49). Since midwall myocardial fibers are oriented mainly in the circumferential direction (66,67), the shortening of the HARP tracked centerline approximates well the shortening of the underlying myocardial fibers.
In Fabry patients with LVH, significant functional changes were detected for LV shortening and contraction, which is consistent with results from echocardiographic studies (62,68). In addition, LV rotation and torsion were examined in this study and significantly altered values were also found for these parameters in the Fabry patients with LVH. The consequence of the increased peak values in rotation and torsion is a faster untwisting of the left ventricle during diastole. Similar results were found in CMR studies where patients with LV pressure overload hypertrophy due to aortic stenosis were examined (17,57). In these studies, the differences in relative torsion were explained to arise from the complicated LV muscle fiber arrangement combined with an equal sarcomere shortening. Myocardial sarcomeres form a helical

structure with varying orientation angle between the endo- and the epicardium, causing substantial torsional deformation in order to maintain transmural homogeneity in sarcomere shortening. Along those lines, Ashikaga et al. concluded in their study of mongrel dog hearts, that the LV mechanics during early relaxation involve substantial deformation of fiber and sheet structures with significant transmural heterogeneity (64). Consequently, global torsional recoil, which is caused by a predominant epicardial stretch along myofibers during isovolumetric relaxation, supports early diastolic filling.

The data of this work suggest that changes of cardiac motion can be detected in patients with Fabry disease before they develop LVH. Changes in LV rotation and torsion appear to precede the occurrence of morphological changes. The high sensitivity of these parameters in regard to the detection of an altered myocardial function was also reported in previous studies (57,69,70). Other than in patients with LV hypertrophy due to pressure overload (17), these reduced values of LV rotation and torsion are already visible before development of LVH and seem to be independent of any increase in LV mass. Rearrangement of myocardial fibers and myocardial fibrosis (71,72) might occur prior to the onset of LVH. This assumption is supported by recent work (73), where the cause for the increase of LV mass in Fabry patients is attributed to a circulating growth-promoting factor rather than to high blood pressure or an accumulation of lysosomal storage bodies in the myocardium. However, values of LV rotation and torsion in Fabry patients without LVH need to be correlated with results from histological examinations to fully confirm this hypothesis. The faster LV untwisting velocities during the rapid filling phase are a direct consequence of the increased values of the rotation and torsion parameters at end-systole.

While rotation parameters seem to be more sensitive for the detection of functional changes in myocardial motion compared to LV contraction and shortening measurements, it has to be considered that rotation values obtained by HARP are less reliable regarding reproducibility compared to circumferential shortening values, as described in (49). This reduced reproducibility of rotation parameters can be explained by their high dependency on the cardiac level between apex and base, meaning that small differences in slice position can alter the measured rotation values significantly. However, this effect is minimized in the torsion values due to the subtraction of the rotation values of two slices and the subsequent normalization on the distance between the acquired slices.

In conclusion, CMR imaging with CSPAMM for myocardial tagging and peak-combination HARP is a sensitive tool to detect alterations of myocardial motion among different groups of patients and controls. The acquired data showed that an increase of LV mass in patients with

Fabry disease is accompanied by impaired LV shortening and contraction. By measuring additional cardiac motion parameters such as LV rotation and torsion, early cardiomyopathy in patients with Fabry disease could be detected already before the development of LVH. Further investigation is required to examine early structural changes within the myocardium and the influence of ERT on the assessed motion parameters.

Chapter 4:

Cardiac Motion in Patients with Left Bundle Branch Block and after Myocardial Infarction

4.1 Introduction

Both left bundle branch block (LBBB) or scar formation in ischemic heart disease can result in regional wall motion abnormalities, left ventricular (LV) dyssynchrony, and further impairment of LV function. Conduction disturbances as well as ischemia or scar in the LV myocardium have been shown in animals and humans to cause dyssynchrony and intraventricular unloading phenomena (51,74-76). Congestive heart failure patients with features of dyssynchrony are therefore considered candidates for cardiac resynchronization therapy (CRT). CRT has proved successful in large patient populations, but around 20-30% of patients do not appear to benefit from CRT (5) applying current patient selection criteria which mainly consider symptoms, global LV ejection fraction (LVEF), and QRS duration (77). In addition, more sophisticated approaches using echocardiography to quantify LV dyssynchrony yielded contradictive results (78-80). Therefore, a better understanding of the mechanisms involved in the various forms of intraventricular dyssynchrony is needed.

Cardiac magnetic resonance (CMR) offers the possibility to acquire motion encoded data sets with high temporal resolution using sophisticated tagging techniques, which can differentiate local tissue deformation from bulk cardiac motion or tethering (81-83). While conventional, two-dimensional techniques are limited in practical use by long scan times and slice registration problems, a novel method was recently introduced (84) that allows measuring three-dimensional (3D), tagged volumes covering the entire LV in less than two minutes examination time. Moreover, CMR can provide accurate viability information in the entire LV (85,86).

A large variety of different mechanical (87,88) and temporal (75,82) CMR tagging parameters has been suggested to describe dyssynchrony and several parameters have been validated in animal models (83). A most promising parameter, the circumferential uniformity ratio estimate (CURE) (83,87,89) (also called TUS: temporal uniformity of strain) readily predicted the responsiveness to CRT in dog experiments. However, this approach utilizing the CURE index is hampered by the fact, that dyssynchrony is lumped into one value (1= perfect synchrony; 0= complete dyssynchrony), while the information of location of dyssynchrony in the LV is no longer available. This might be relevant, if one considers the fact, that the absence of scar tissue is crucial for prediction of CRT success (90).

Accordingly, the aims of this study were: 1) to transfer the tagging approach proved successful in canine experiments into humans, 2) to explore its usefulness to describe dyssynchrony in patients with LBBB and in addition in patients with ischemic heart disease and scarring, 3) to further improve the assessment of dyssynchrony allowing for integrating viability information into the 3D data sets, and finally, 4) in order to be clinically applicable, assessment of inter-study and inter-observer reproducibility for these measurements was tested in the various groups of patients.

4.2 Methods

Study Population

The study population consisted of 15 patients with LBBB (without a history of myocardial infarction (MI) or valve disease; $Pats_{LBBB}$) and 25 patients after MI ($Pats_{MI}$). $Pats_{MI}$ were studied by CMR 9.4±8 days after their first acute MI, which was treated in all patients by percutaneous coronary intervention (PCI) and stenting of the infarct-related coronary artery. Additionally, 15 age-matched healthy volunteers served as control group (Controls). None of the Controls had a known history or signs of cardiac disease. More detailed demographic and cardiac characteristics of each study group are listed in Table 4.1. The study protocol was approved by the institutional review board and written informed consent was obtained from all study participants prior to study entry.

	Controls	$Pats_{LBBB}$	$Pats_{MI}$
n	15	25	15
Male, n(%)	11 (73%)	8 (53%)	21 (84%)
Age [years]	53.3 (±9.7)	62.9 (±10.1)	60.5 (±10.4)
Body mass index [kg/m^2]	24.9 (±2.3)	27.6 (±6.7)	26.7 (±3.7)
Heart rate [bpm]	67.5 (±12.4)	68.7 (±12.2)	69.4 (±12.1)
QRS-width [ms]	-	144.9 (±12.1)	90.4 (±11.7)
LVEDV [ml]	135.7 (±36.1)	152.6 (±48.7)	137.0 (±32.2)
LVESV [ml]	53.3 (±13.6)	77.1 (±33.3)	89.3 (±29.9)***
LVEF [%]	60.4 (±3.5)	50.9 (±8.4)**	37.1 (±9.8)***

Table 4.1: *Demographic and cardiac characteristics of each study group are listed. LVEDV = LV end-diastolic volume, LVESV = LV end-systolic volume, LVEF = LV ejection fraction. All values are indicated as mean ± SD. * P<0.05, ** P<0.01, *** P<0.001 for controls vs. corresponding group of patients.*

Data Acquisition

The complete imaging protocol is shown schematically in Figure 4.1. All measurements were performed on a 1.5T MRI scanner (Achieva, Philips Healthcare, Best, the Netherlands). After acquiring survey images and calibration data, short-axis images covering the entire LV were acquired using a balanced steady state free precession (SSFP) sequence (cardiac phases = 20, temporal resolution = 45ms, slice thickness = 8mm, 13-16 contiguous slices during repetitive breath-holds) to assess global LV function. An additional SSFP measurement with higher temporal resolution (cardiac phases = 50, temporal resolution = 17.6ms, slice thickness = 8mm) was performed through the aortic valve to determine timing of aortic valve closure (AVC).

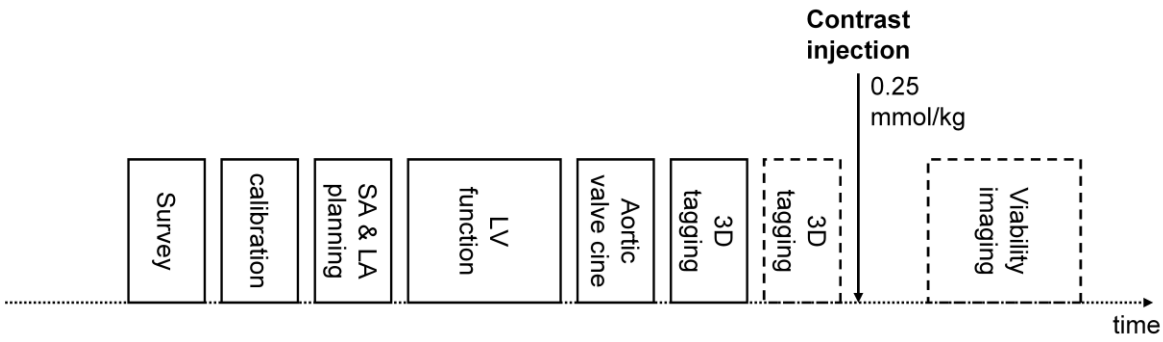

Figure 4.1: *Imaging protocol. SA = short-axis cardiac views; LA = long-axis cardiac views. For inter-study reproducibility assessment a second 3D tagging data set was acquired in five controls and ten LBBB patients. Viability imaging was only performed in MI patients (dashed boxes).*

For the 3D tagging data acquisition a novel, accelerated acquisition scheme with Complementary Spatial Modulation of Magnetization (CSPAMM) was applied (84) requiring three breath-holds of 18 RR-intervals duration each to cover the entire LV. For read-out, a modified hybrid multi-shot, segmented EPI sequence was employed and ramped flip angles were used to prevent tag fading during the cardiac cycle (14,23) (FOV = 108x108x108mm^3, voxel size per encoding direction = 3.9x7.7x7.7mm^3, echo time = 3.3ms, tag distance = 7mm). The first time frame was acquired 17ms after the ECG R-wave and, depending on the heart rate, 19 to 25 time frames were recorded with a temporal resolution of 27ms to 37ms and a final flip angle of 18º to 25º. To allow for tagging data registration, right diaphragm position at the beginning of each breath-hold was controlled using a navigator echo (91). Acquisition of the second and third data set was only started, if the diaphragm position was within the predefined window of 15mm of the first breath-hold (50) and any difference within this 15mm-window was additionally corrected for.

For the assessment of inter-study reproducibility, the 3D tagging acquisition was repeated in 5 Controls and 10 Pats$_{LBBB}$. To assess inter-observer reproducibility, data from 5 Pats$_{MI}$ were post-processed by a second observer.

Late gadolinium-enhanced (LGE) short-axis images covering the entire LV were additionally acquired in all Pats$_{MI}$ 15 minutes after administration of a bolus of 0.25mmol/kg body weight of Gadobutrolum (Gadovist, Bayer-Schering Pharma, Germany) using an inversion recovery segmented gradient echo sequence with inversion time set in order to null normal

myocardium (FOV = 350×350mm^2, pixel size = 1.5×1.5mm^2, repetition time = 7.4ms, echo time = 4.4ms, slice thickness = 8mm, no slice gap).

Data Analysis

The 3D tagging data were post-processed with HARP (16,30) using an in-house software tool extended for the analysis of 3D tagging data. Eight to eleven short-axis midwall contours, consisting of multiple material points arranged in steps of about 5°, were defined on slices covering the entire LV. The contours were subsequently HARP-tracked (16,30) in 3D space through all time frames. To correct for phase errors from magnetic field inhomogeneities and to increase HARP accuracy, peak-combination HARP (30) was applied. The spatial resolution resulting from the 3D bandpass filtering in k-space was 9x9x9mm^3, characterizing the spatial blurring of the final displacement data. Midwall circumferential shortening (*csh*(*t*), in %) was defined as the length change of a contour at time *t* relative to the original length at end-diastole (first heart phase). For a detailed analysis of *csh*(*t*) in 48-66 segments of each LV, each midwall contour was divided into sectors of 60° starting at the anterior epicardial junction of the right and the left ventricle on the equatorial level and numbered consecutively from S1 to S6 in clockwise direction as viewed from the apex. For the segment-wise calculation of the average *csh* at time of aortic valve closure (AVC) in Controls, $Pats_{LBBB}$, and $Pats_{MI}$ the obtained *csh*(AVC) data were resampled at ten cardiac levels, in order to equalize the number of slices.

The time to maximum *csh*, T_{max}, was automatically determined for each segment. To eliminate unreliable values of T_{max} due to akinesia or tracking artifacts, segments in which T_{max} was detected in the first three or in the last acquired time frame were inspected by an observer and corrected manually if necessary (56). As a measure of mechanical LV dyssynchrony the standard deviation (SD) of T_{max} over the LV was calculated (89) as well as the CURE-index, as described in (87): *Csh* was plotted versus spatial position for each slice and in each time frame. The plots were subjected to Fourier analysis, and CURE was calculated as follows: $CURE = (A_0^2/[A_0^2+2A_1^2])^{1/2}$, where A_0^2 and A_1^2 are the sums over space and time of the zero and first order power terms, respectively. Thus, CURE represents a measure for the amount of oscillation in the plots of *csh* versus spatial position. CURE ranged from 0 (pure dyssynchrony) to 1 (synchronous).

In order to obtain localized information about regional dyssynchronous motion as well as a global dyssynchrony estimate for the entire LV, a new parameter, the systolic dyssynchrony

index (SDI), was calculated. The regional estimate in each segment (SDI_{segm}) was defined as the area under curve of *csh*(t) from t=1/3·AVC to t=AVC:

$$SDI_{segm} = \int_{1/3\,AVC}^{AVC} csh(t)dt \qquad [1.16]$$

The SD of the obtained values of all segments over the LV divided by the LV mean value defined SDI for global measurement of LV dyssynchrony:

$$SDI = \frac{SD(SDI_{segm})}{mean(SDI_{segm})} \qquad [1.17]$$

Thus, SDI is sensitive for heterogeneous contractions towards the end of systole. High values will therefore recognize late contracting segments, which would benefit from early pacing. Measuring the area under curve is less susceptible to noise than analyzing a single time point during contraction only.

It was assumed that sectors with altered contraction and >50% scar would not recover contraction even when perfectly synchronized. These sectors were therefore excluded from SDI calculation yielding SDI_{viable}.

The performance of HARP tracking was assessed by determining the number of tracking errors during HARP post processing of each data set. A tracking error of a material point from one time frame to the next could be caused by the following reasons (16): 1. Non-convergence of the HARP algorithm. 2. The displacement exceeded the tagging distance. 3. The displacement of neighboring points was significantly different. Tracking errors were detected automatically and corrected by the software based on the motion of correctly identified neighboring points.

For validation of the 3D tagging method, the ability of the method to detect regions with motion impairment due to the presence of scar tissue was tested in $Pats_{MI}$. Regional deformation patterns were correlated with the presence of scar tissue. LGE data sets were manually post-processed using a dedicated software tool (GTVolume, GyroTools Ltd., Zurich, Switzerland) and late-enhanced areas inside the myocardium were considered to represent scar tissue. For each patient with MI, *csh*(AVC) was averaged for all segments without scar as well as for all segments with 1-25% scar, 26-50% scar, 51-75% scar, and 76-100% scar.

Statistics

Results between study groups were compared with an analysis of variance (ANOVA) followed by Bonferroni post-hoc testing (InStat, 3.01, GraphPad Software Inc., San Diego, California, USA). Differences in *csh* between segments with varying amounts of late enhancement in MI patients were tested applying an ANOVA for repeated measurements followed by Bonferroni post-hoc testing. For the data in Figure 4.7, two patients with MI were discarded for the calculation of P values because none of the segments exhibited more than 75% of scar tissue. P values <0.05 were considered statically significant. Inter-study and inter-observer reproducibility was evaluated by means of Bland-Altmann plots (92).

4.3 Results

Demographics

Demographics and cardiac characteristics of each study group are given in Table 4.1. The $Pats_{MI}$ group consisted of 25 patients, 14 of them with 1-vessel disease, 8 with 2-vessel disease, and 3 with 3-vessel disease. The infarct-related artery was the left anterior descending coronary artery (LAD) in 23 patients and the right coronary artery (RCA) in 2 patients. Peak CK-MB in the 25 patients was 462.6±298.4 U/l and peak troponin T was 11.8±13.0 µg/l. Scar mass in the 25 patients was 24.2±10.2% of the total LV mass.

Dyssynchrony in Controls, $Pats_{LBBB}$, and $Pats_{MI}$

Global LVEF was lowest in the $Pats_{MI}$ with 37.1±9.8% (P<0.001 vs. Controls), while in $Pats_{LBBB}$ LVEF was only slightly reduced to 50.9±8.4% (P<0.01 vs. Controls, Table 4.1 and Figure 4.2). Despite this pattern of reduced LV function, dyssynchrony as assessed by the CURE index was lowest (most severe dyssynchrony) in $Pats_{LBBB}$ as shown in Figure 4.2. The proposed systolic dyssynchrony index (SDI) shows a similar pattern. The variance of T_{max} over all LV segments calculated by the SD was significantly greater in $Pats_{LBBB}$ and $Pats_{MI}$ (P<0.001) compared to controls, but did not demonstrate a difference between patient groups. In accordance with LVEF results, significantly reduced mean *csh*(AVC) over the entire LV could be detected in both $Pats_{LBBB}$ and $Pats_{MI}$ compared to Controls (P<0. 05 and P<0. 001, respectively; Figure 4.2). T_{max} mean (time to peak *csh*) was similar in Controls and $Pats_{MI}$, but occurred delayed in $Pats_{LBBB}$ (P<0.001, Figure 4.2).

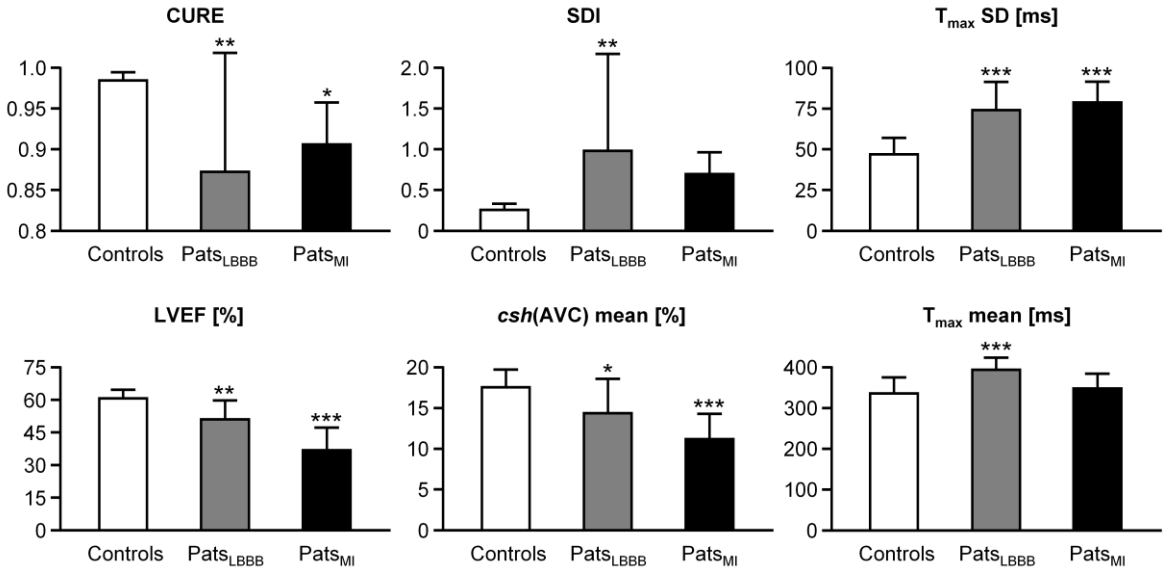

Figure 4.2: *Dyssynchrony and LV (global) mechanical parameters are shown in the top and bottom row, respectively, for controls (n=15), LBBB patients (n=15), and MI patients (n=25). All values are given as mean ± SD. * P<0.05, ** P<0.01, *** P<0.001 vs. controls.*

An excellent correlation was found between the CURE and the SDI parameters (linear regression: R=0.96, Figure 4.3). Moreover, LV scar mass and CURE correlated similarly as LV scar mass and SDI (Figure 4.4) in $Pats_{MI}$.

Correlation of QRS duration with dyssynchrony parameters (CURE, SDI, T_{max} SD) acquired in each group of patients yielded no significant results.

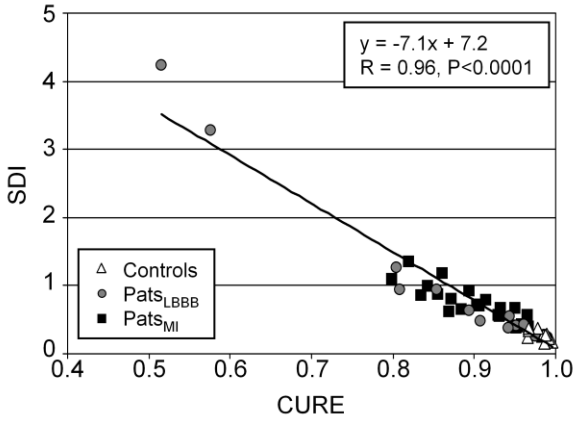

Figure 4.3: *A high correlation was found between the CURE and the SDI parameter.*

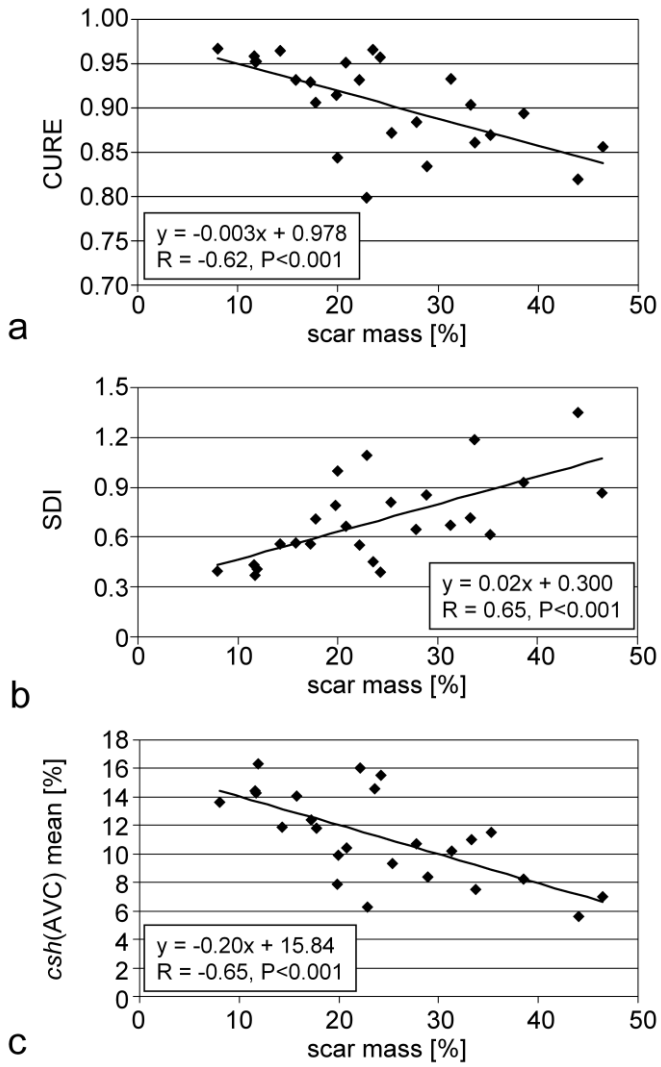

Figure 4.4: *Linear regressions between scar mass as measured by the LGE technique and different dyssynchrony and deformation parameters obtained from 3D tagging data sets of MI patients: a) CURE. b) SDI. c) Mean csh(AVC) of the entire LV.*

Results of one representative subject out of each study group (Controls, $Pats_{LBBB}$, and $Pats_{MI}$) are given in Figure 4.5. A patient after antero-septal infarction is shown to demonstrate the similarity with the LBBB dyssynchrony pattern. Both patients show increased SDI values (0.71 and 1.26, respectively) compared to the control (0.27). In the patient after MI, the infarcted segments show severely reduced (or absent) shortening during systole (Figure 4.5g). After AVC pronounced post-systolic shortening of the infarcted segments begins immediately with relaxation of the non-infarcted (lateral) segments. The patient with LBBB shows a similar pattern with the septum (segment S6 in Figure 4.5d) being even lengthened, i.e. stretched due to simultaneous contractions in the lateral wall. As in the MI patient, the septum of the LBBB patient begins to "contract" in early diastole exactly at the time point when contraction in the lateral wall (segment S3 in Figure 4.5d) terminates.

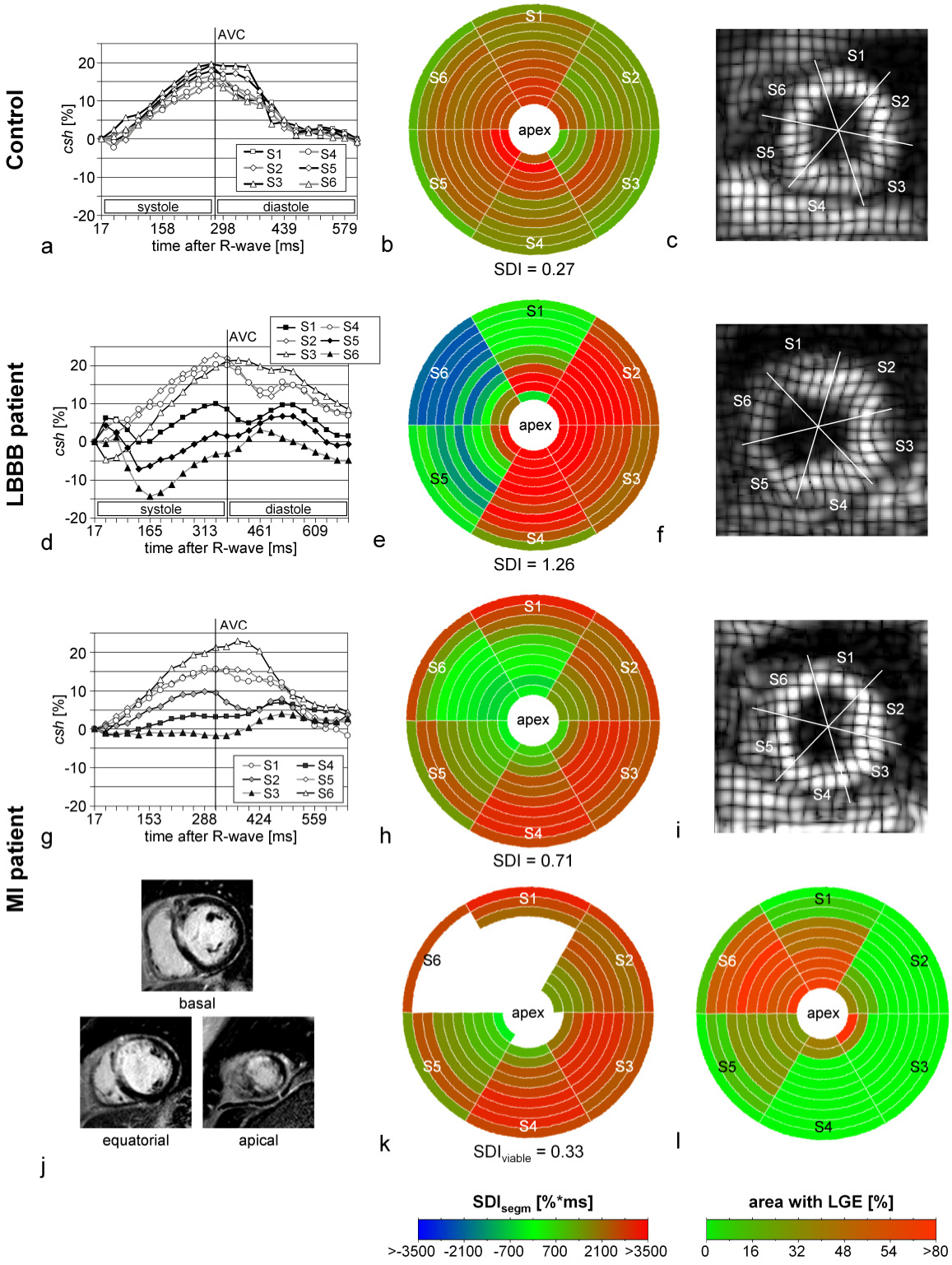

Figure 4.5: *Representative 3D tagging results from a control (a-c), a LBBB patient (d-f) and a MI patient (g-l). a,d,g) Csh(t) for 6 segments on an equatorial level. b,e,h) Bull's eye plots of SDI_{segm}. c,f,i) Short-axis slice at AVC with sector definitions. j) Three representative slices of LGE images out of 10 acquired slices are shown. k) Bull's eye plot for SDI_{viable} is shown, where segments with scar mass ≥50% are excluded. l) Bull's eye plot of viability as derived from LGE data.*

In Figure 4.6, all Controls, all $Pats_{LBBB}$, and 9 $Pats_{MI}$ were averaged and are represented in the bull's eye plots. For the $Pats_{MI}$ group, only patients with an antero-septal MI of 15-25% of the LV mass were selected to allow for meaningful averaging. A similar dyssynchrony pattern within the LV is observed for $Pats_{LBBB}$ and $Pats_{MI}$ in agreement with the bar graphs and the examples of Figure 4.2 and Figure 4.5, respectively.

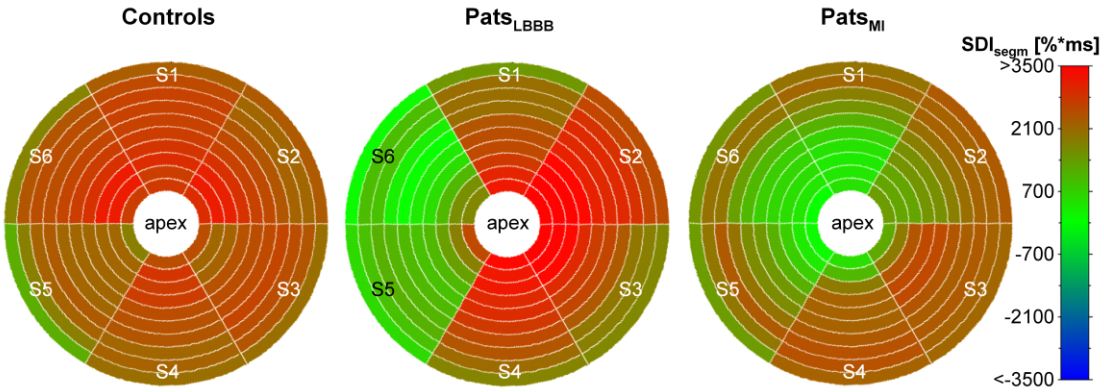

Figure 4.6: *Bull's eye plots of SDI averaged over each study group: controls (n=25), LBBB patients (n=15), and MI patients (n=9).*

Incorporation of viability information into dyssynchrony assessment

While the dyssynchrony pattern for $Pats_{LBBB}$ and $Pats_{MI}$ with antero-septal MI was similar (Figure 4.6), the expected maximum improvement in shortening with CRT in an individual sector would change, if one considers the viability information as represented in the bull's eye plot in Figure 4.5l. If a ≥50% transmurality of scar is assumed to prevent contraction in a given segment, even if full synchronization would be achieved, such sectors would not contribute to improvement of overall LV function. Consequently, such segments were excluded for the SDI calculation yielding SDI_{viable}. In the MI patient, the resulting SDI_{viable} yielded a value of 0.33 close to that of 0.27 in the control. For the LBBB patient SDI_{viable} was 1.26 indicating a much larger potential gain in sectorial contractions. A value of 0.27 in the control would indicate no possible change. Mean SDI_{viable} for the Controls was 0.26±0.07 (95% confidence interval: 0.22-0.29).

Method performance and reproducibility of results

Dependency of regional *csh*(AVC) on the amount of scar tissue in $Pats_{MI}$ is illustrated in Figure 4.7 confirming the influence of scar on regional function.

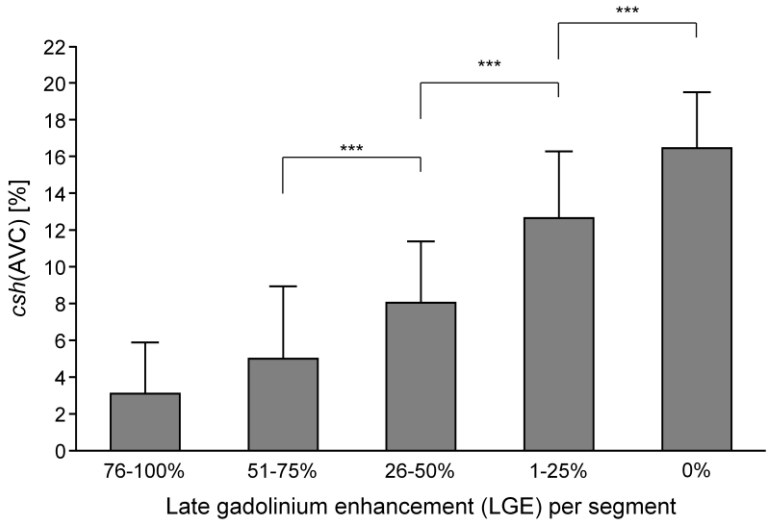

***Figure 4.7**: Csh(AVC) depending on the amount of LGE per segment in $Pats_{MI}$. Increasing amount of scar reduces segmental contractile function. Mean values and standard deviations over all patients are given. *** P<0.001.*

The inter-study reproducibility for CURE was high as demonstrated in the Bland-Altman plots in Figure 4.8, while an intermediate reproducibility resulted for the SDI and T_{max} SD. Similar results were obtained for the inter-observer reproducibility.

The average tracking error percentages of the HARP analyses were 5.3±2.0% for controls, 9.5±3.9% for $Pats_{LBBB}$, and 6.7±3.5% for $Pats_{MI}$. Thus, tracking performance was similar in all patient groups and a bias in analysis leading to differences among study groups is unlikely.

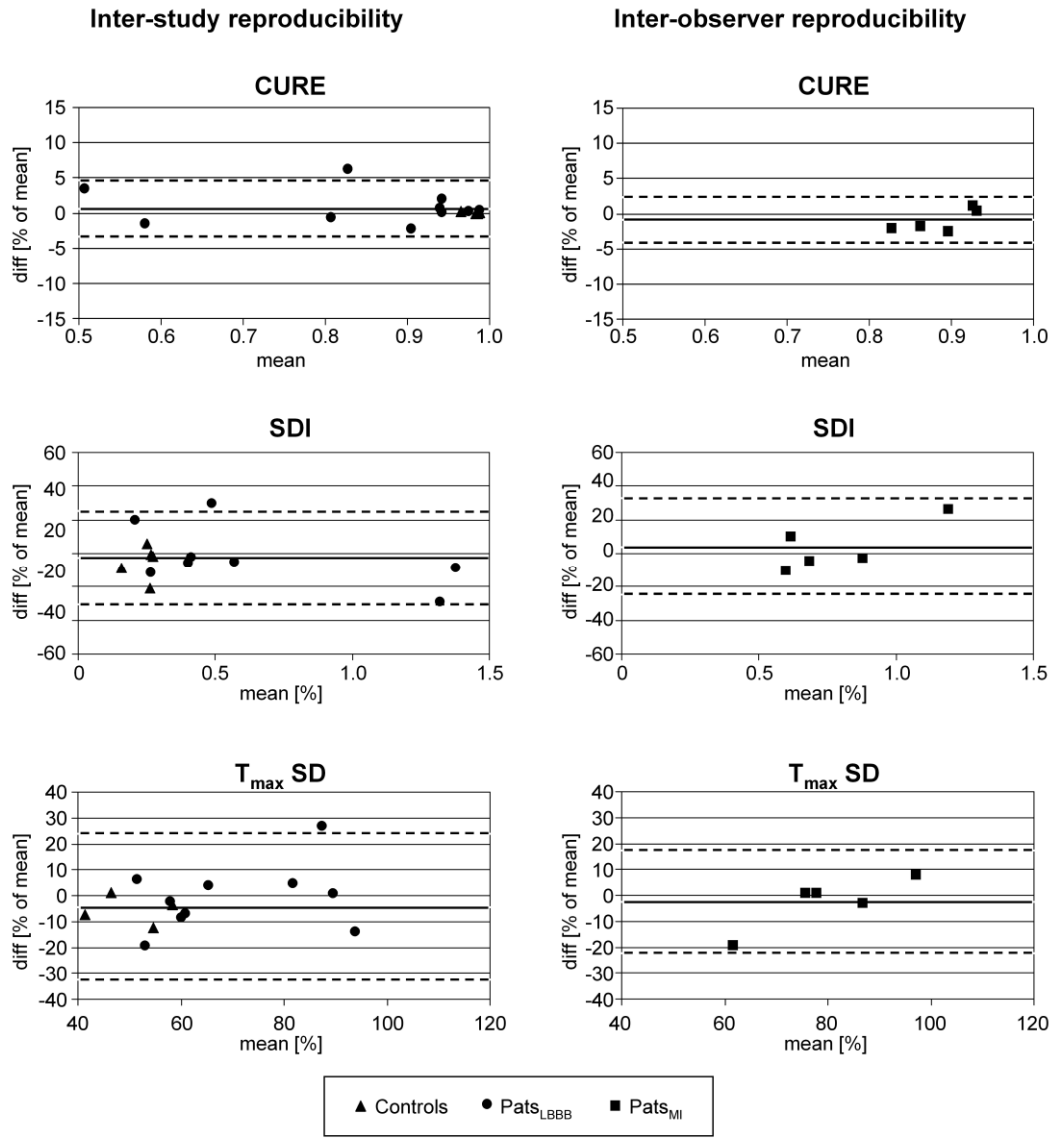

Figure 4.8: *Inter-study (left) and inter-observer reproducibility (right) of parameters measuring LV dyssynchrony represented as Bland-Altman plots. SDI, CURE, and T_{max} SD are shown. Dashed horizontal lines indicate ±95% confidence intervals, bold lines represent mean differences (=bias).*

4.4 Discussion

The main findings of the study are as follows: 1) The assessment of intraventricular dyssynchrony validated in earlier animal studies with LBBB could be transferred successfully into humans including patients with various underlying disease pathologies. 2) Despite

different underlying diseases, i.e. LBBB and ischemic heart disease with infarctions, the observed patterns of dyssynchrony were similar between LBBB and antero-septal MI. 3) By utilization of a segmental based dyssynchrony parameter, viability information could be easily integrated to yield a comprehensive approach for dyssynchrony and viability assessment in ischemic heart disease, and 4) a sufficiently high reproducibility for these dyssynchrony parameters in patients was demonstrated.

Transfer of a dyssynchrony CMR technique into patients

Current state-of-the-art imaging technology opens a wide spectrum of potential parameters to describe intraventricular dyssynchrony. The circumferential uniformity ratio estimate (CURE) was evaluated in several animal studies with LBBB to estimate LV dyssynchrony in longitudinal and circumferential directions (83). CURE proved superior to other tagging parameters to identify the synchronizing effect of various pacing modes (83,93). As a 3D data set would ideally provide the basis for such analyses, a novel 3D tagging strategy opened new perspectives by transferring the technique into humans. While other tagging techniques required approximately 45 minutes to cover the entire LV (94), the present technique acquires the complete data set in less than two minutes examination time. Three breath-holds of 18 heartbeats duration each are required for complete data acquisition. The technique produced adequate data quality for analysis in all cases. Furthermore, the HARP approach (53), modified to increase signal-to-noise ratio (30) and thus to increase robustness of the analysis, produced results in a few minutes, which is an important aspect of imaging techniques, if applications in clinical practice are anticipated. The short acquisition time of three breath-holds and a fourth for evaluation of AVC is also relevant with regard to a clinical application, as examination time directly translates into costs.

Moreover, reproducibility of a test is of paramount importance in the setting of clinical research. To better understand the mechanisms of action, e.g. of CRT, accurate methods are required to detect small differences in contraction patterns, provoked e.g. by different CRT strategies. Reproducibility is also important, as small effects of CRT might be detectable in larger study populations only. In this context, it is noteworthy that in the PROSPECT trial (80), a large multicenter echo-based CRT trial, relevant conclusions were difficult to draw, since the imaging parameters used to assess the effect of CRT were compromised by low reproducibility. Thus, for successful larger clinical trials reliable methods to objectify the effect of interventions are needed. In this respect, the presented 3D tagging CMR approach

fulfills several requirements such as short acquisition times, adequate robustness to be performed in patients, fast semi-automatic analysis, and adequate reproducibility.

Patterns of dyssynchrony in LBBB and ischemic heart disease

Several dyssynchrony parameters such as the CURE parameter were validated primarily in animals and often the presence of an LBBB was used as the model mimicking dyssynchrony in patients (87,89). While most dyssynchrony parameters are aimed at "condensing" the dyssynchrony information into a single quantitative measure, this approach is inherently limited by eliminating some information on the local distribution of dyssynchrony. Therefore, in addition to the CURE index, a dyssynchrony parameter was proposed, which measures systolic performance in each LV segment to preserve spatial information, and then allows "condensing" it into a single value by considering the statistical variability of the performance in the various segments. The resulting SDI showed a similar pattern for dyssynchrony as the CURE index (Figure 4.2), with highest dyssynchrony in the LBBB patients and a dependency of dyssynchrony on the amount of scar tissue in MI patients (Figure 4.4). The high variability of both SDI and CURE in $Pats_{LBBB}$ could indeed reflect differences in dyssynchrony among patients with LBBB. Animal studies in LBBB demonstrated substantial differences in adaptive remodeling of hearts subjected to LBBB (75), which could also cause differences in dyssynchrony evoked by LBBB.

Relationship between QRS and CMR dyssynchrony parameters

QRS duration of ≥120ms is a major criterion among others to select patients for CRT combining into a class I indication (77). None of the dyssynchrony parameters acquired (CURE, SDI, SD T_{max}) correlated with QRS duration in $Pats_{LBBB}$ or $Pats_{MI}$. The lack of a correlation between dyssynchrony parameters and QRS duration in LBBB is in line with experimental studies which demonstrated a variable response to LBBB induction between animals (75).

Integration of tissue viability into an integrative approach to assess dyssynchrony

The similarity of dyssynchrony patterns in LBBB and antero-septal infarcts emphasizes the importance of integrating viability information into maps of dyssynchrony. The proposed SDI as any segmental-based approach to quantify dyssynchrony is ideal to integrate viability information. Assuming that a ≥50% scar transmurality in a given segment would prevent

systolic contractions, such segments can easily be eliminated from the calculation of a global dyssynchrony estimate. For example, in the patient after MI given in Figure 4.5, the SDI_{viable} was 0.33, which is comparable to the SDI_{viable} of 0.27 obtained in the healthy control. Consequently, the SDI_{viable} in this patient after MI indicates no potential improvement in contractile segmental function with pacing.

Limitations

The CURE index is well validated in LBBB in animal models. Therefore, it was used in the present study as the reference for comparisons with other parameters of dyssynchrony such as the SDI. This means, that no other "gold standard" for quantification of dyssynchrony was applied in this study for the LBBB patients. Similarly, for the $Pats_{MI}$, no other measures of reference for dyssynchrony were performed which is mainly explained by the lack of any absolutely established measure to quantify dyssynchrony in these patients.

The 3D nature of the tagging data in the patients would allow for a multi-directional analysis of strain in the LV, i.e. not only in circumferential, but also in longitudinal and radial direction. However, convincing data applying echocardiography (95) and CMR (83) indicate that longitudinal strain might be less sensitive to dyssynchrony than circumferential strain.

4.5 Conclusions

A novel, fast, and reliable 3D tagging technique was successfully applied to humans for calculations of various dyssynchrony parameters. The well established CURE index was successfully derived from these 3D tagging data acquired in patients with LBBB or MI. An alternative dyssynchrony parameter, SDI_{viable}, is proposed which incorporates viability distribution. To assess its usefulness to predict CRT responsiveness in patients, future studies are required assessing heart function before and after therapy.

Discussion and Outlook

Magnetic resonance imaging techniques are increasingly used in clinical cardiology. Due to the tremendous technical development within the last decades, acquisition speed could be increased by several orders of magnitude and image quality drastically improved. Cardiac MRI provides not only information about heart anatomy but also allows for non-invasive assessment of cardiac function. Myocardial tagging represents a unique tool to analyze tissue motion in healthy and diseased state and has emerged as the gold-standard to characterize regional cardiac motion in a preclinical setting. Sophisticated acquisition methods to obtain tagged images with good image quality and without through-plane motion effects as well as the introduction of fast and automatic post-processing techniques such as harmonic phase (HARP) analysis have made the tagging method attractive for use in large patient studies and have brought it closer to clinical routine.

In this dissertation, different techniques to acquire and post-process motion encoded MRI data were discussed. Complementary Spatial Modulation of Magnetization (CSPAMM) in combination with slice-following and peak-combination HARP post-processing proved to be a fast and reliable method to accurately assess cardiac deformation. The technique was applied to assess cardiac motion in patients with Fabry disease, and abnormal motion patterns were found even in patients without macroscopic cardiac involvement. However, as the acquisition of multiple two-dimensional slices covering the entire left ventricle in different orientations leads to long scan times, tagging data from only a few selected locations could be acquired within the limited examination time. Moreover, the obtained data represent only two-dimensional projections of the underlying three-dimensional (3D) motion pattern.

An accelerated acquisition method has been developed in this thesis that allows assessing true 3D left ventricular motion information in acceptable scanning times, enabling its application not only in healthy volunteers but also in patients with cardiac diseases. It could be demonstrated that the technique can be applied in patients after myocardial infarction and left bundle branch block to assess left ventricular dyssynchrony. This is considered an important

step forward with regard to a more efficient selection of patients for cardiac resynchronization therapy.

The acquisition of data containing information about left ventricular mechanics has been optimized in this thesis to achieve short scan times while providing whole heart coverage. In further work, data acquisition could be extended to more breath-holds, in order to improve spatial resolution. Any reduction in voxel size allows a better correlation between the obtained contraction values and the actual shortening of myocardial fibers. A better spatial resolution would also allow assessing right ventricular motion parameters, yielding a more complete characterization of cardiac mechanics of the entire heart. Furthermore, using a smaller voxel size, differences in the contraction of endo- and epicardium could be assessed and detailed strain maps visualized. Detection of smaller changes in myocardial deformation would permit lower necessary sample sizes in clinical studies with potentially earlier and improved diagnosis of cardiac diseases.

Early detection of cardiac motion changes induced by ischemia often requires examination under pharmacological or physical stress (96,97). The measurement of two- or three-dimensional tagging data under these circumstances is challenging, as with the increased cardiac frequency a higher temporal resolution is required and data acquisition needs to be performed within a limited amount of time. In the past, two-dimensional tagged slices were successfully measured under physiological stress by applying a highly accelerated tagging acquisition scheme (49). The acquisition of motion encoded data in 3D and with whole-heart coverage under stress would certainly lead to further insights into cardiac function. Accelerated data acquisition in combination with a coached breathing scheme under navigator control could help to achieve this goal in the future.

In clinical routine, multiple aspects of cardiac function and anatomy are of interest, such as myocardial viability and perfusion, patency of heart valves and coronary arteries, and blood flow. Hence, there is a need to complete each measurement including myocardial deformation determination fast and with a minimum amount of user interaction. In this dissertation modifications and new tools have been described to assess overall left ventricular motion in a comprehensive and fast fashion. The feasibility to obtain accurate and reproducible information about whole-heart mechanics within a reasonable amount of time could be demonstrated in patient studies. In the future, continuous improvement in scanner hardware and the rapid development of new techniques to further accelerate MRI scans will alleviate current trade-offs among spatiotemporal resolution and scan time. The use of higher field strengths will not only increase the image signal-to-noise ratio but should also be beneficial

with tagging due to prolonged T1 relaxation. However, it will be necessary to address new challenges when measuring at a higher B0 field. The speed-up in imaging time will not only improve patient comfort, but also provide improved insights into cardiac function in healthy and diseased state.

In cardiology, the introduction and application of new treatment concepts, such as stem cell therapy, cardiac ablation and cardiac resynchronization therapy will further increase the interest for assessing cardiac mechanical function. Furthermore, measurement of regional cardiac motion will be crucial to study consequences and possible side-effects after heart transplantation and with regard to novel medication strategies. The application of comprehensive and accurate methods to measure cardiac deformation will therefore be of great interest in the future.

References

1. Silbernagl S, Despopoulos A. Taschenatlas der Physiologie. Stuttgart: Thieme; 2001. 436 p.
2. Moore CC, McVeigh ER, Zerhouni EA. Noninvasive measurement of three-dimensional myocardial deformation with tagged magnetic resonance imaging during graded local ischemia. J Cardiovasc Magn Reson 1999;1(3):207-222.
3. Puleo JA, Aranda JM, Weston MW, Cintron G, French M, Clark L, Fontanet HL. Noninvasive detection of allograft rejection in heart transplant recipients by use of Doppler tissue imaging. J Heart Lung Transplant 1998;17(2):176-184.
4. Mollema SA, Liem SS, Suffoletto MS, Bleeker GB, van der Hoeven BL, van de Veire NR, Boersma E, Holman ER, van der Wall EE, Schalij MJ, Gorcsan J, 3rd, Bax JJ. Left ventricular dyssynchrony acutely after myocardial infarction predicts left ventricular remodeling. J Am Coll Cardiol 2007;50(16):1532-1540.
5. Kass DA. Cardiac resynchronization therapy. J Cardiovasc Electrophysiol 2005;16 Suppl 1:S35-41.
6. Garcia MJ, Rodriguez L, Ares M, Griffin BP, Klein AL, Stewart WJ, Thomas JD. Myocardial wall velocity assessment by pulsed Doppler tissue imaging: characteristic findings in normal subjects. Am Heart J 1996;132(3):648-656.
7. Helle-Valle T, Crosby J, Edvardsen T, Lyseggen E, Amundsen BH, Smith HJ, Rosen BD, Lima JA, Torp H, Ihlen H, Smiseth OA. New noninvasive method for assessment of left ventricular rotation: speckle tracking echocardiography. Circulation 2005;112(20):3149-3156.
8. Atkinson DJ, Burstein D, Edelman RR. First-pass cardiac perfusion: evaluation with ultrafast MR imaging. Radiology 1990;174(3 Pt 1):757-762.
9. Poncelet BP, Weisskoff RM, Wedeen VJ, Brady TJ, Kantor H. Time of flight quantification of coronary flow with echo-planar MRI. Magn Reson Med 1993;30(4):447-457.

10. Mahrholdt H, Wagner A, Judd RM, Sechtem U. Assessment of myocardial viability by cardiovascular magnetic resonance imaging. Eur Heart J 2002;23(8):602-619.
11. Kozerke S, Scheidegger MB, Pedersen EM, Boesiger P. Heart motion adapted cine phase-contrast flow measurements through the aortic valve. Magn Reson Med 1999;42(5):970-978.
12. Zerhouni EA, Parish DM, Rogers WJ, Yang A, Shapiro EP. Human heart: tagging with MR imaging--a method for noninvasive assessment of myocardial motion. Radiology 1988;169(1):59-63.
13. Axel L, Dougherty L. MR imaging of motion with spatial modulation of magnetization. Radiology 1989;171(3):841-845.
14. Fischer SE, McKinnon GC, Maier SE, Boesiger P. Improved myocardial tagging contrast. Magn Reson Med 1993;30(2):191-200.
15. Fischer SE, McKinnon GC, Scheidegger MB, Prins W, Meier D, Boesiger P. True myocardial motion tracking. Magn Reson Med 1994;31(4):401-413.
16. Osman NF, Kerwin WS, McVeigh ER, Prince JL. Cardiac motion tracking using CINE harmonic phase (HARP) magnetic resonance imaging. Magn Reson Med 1999;42(6):1048-1060.
17. Stuber M, Scheidegger MB, Fischer SE, Nagel E, Steinemann F, Hess OM, Boesiger P. Alterations in the local myocardial motion pattern in patients suffering from pressure overload due to aortic stenosis. Circulation 1999;100(4):361-368.
18. Ryf S, Spiegel MA, Gerber M, Boesiger P. Myocardial tagging with 3D-CSPAMM. J Magn Reson Imaging 2002;16(3):320-325.
19. van Dijk P. Direct cardiac NMR imaging of heart wall and blood flow velocity. J Comput Assist Tomogr 1984;8(3):429-436.
20. Pelc LR, Sayre J, Yun K, Castro LJ, Herfkens RJ, Miller DC, Pelc NJ. Evaluation of myocardial motion tracking with cine-phase contrast magnetic resonance imaging. Invest Radiol 1994;29(12):1038-1042.
21. Osman NF, Sampath S, Atalar E, Prince JL. Imaging longitudinal cardiac strain on short-axis images using strain-encoded MRI. Magn Reson Med 2001;46(2):324-334.
22. Axel L, Dougherty L. Heart wall motion: improved method of spatial modulation of magnetization for MR imaging. Radiology 1989;172(2):349-350.
23. Stuber M, Spiegel MA, Fischer SE, Scheidegger MB, Danias PG, Pedersen EM, Boesiger P. Single breath-hold slice-following CSPAMM myocardial tagging. Magma 1999;9(1-2):85-91.

24. Tsao J, Laurent D. N-SPAMM for efficient displacement-encoded acquisition in myocardial tagging. In Proc 13th Annual Meeting ISMRM, Miami, 2005. p. 273.
25. Rutz AK, Tsao J, Ryf S, Soellinger M, Kozerke S, Boesiger P. Implementation of 3-SPAMM for Myocardial Motion Analysis with HARP. In Proc 13th Annual Meeting ISMRM, Miami, 2005. p. 774.
26. Fischer SE, Stuber M, Scheidegger MB, Boesiger P. Limitations of stimulated echo acquisition mode (STEAM) techniques in cardiac applications. Magn Reson Med 1995;34(1):80-91.
27. Epstein FH, Gilson WD. Displacement-encoded cardiac MRI using cosine and sine modulation to eliminate (CANSEL) artifact-generating echoes. Magn Reson Med 2004;52(4):774-781.
28. Stuber M, Fischer SE, Scheidegger MB, Boesiger P. Toward high-resolution myocardial tagging. Magn Reson Med 1999;41(3):639-643.
29. Kuijer JP, Jansen E, Marcus JT, van Rossum AC, Heethaar RM. Improved harmonic phase myocardial strain maps. Magn Reson Med 2001;46(5):993-999.
30. Ryf S, Tsao J, Schwitter J, Stuessi A, Boesiger P. Peak-combination HARP: a method to correct for phase errors in HARP. J Magn Reson Imaging 2004;20(5):874-880.
31. Sampath S, Derbyshire JA, Atalar E, Osman NF, Prince JL. Real-time imaging of two-dimensional cardiac strain using a harmonic phase magnetic resonance imaging (HARP-MRI) pulse sequence. Magn Reson Med 2003;50(1):154-163.
32. Aletras AH, Ding S, Balaban RS, Wen H. DENSE: displacement encoding with stimulated echoes in cardiac functional MRI. J Magn Reson 1999;137(1):247-252.
33. Spottiswoode BS, Zhong X, Hess AT, Kramer CM, Meintjes EM, Mayosi BM, Epstein FH. Tracking myocardial motion from cine DENSE images using spatiotemporal phase unwrapping and temporal fitting. IEEE Trans Med Imaging 2007;26(1):15-30.
34. Aletras AH, Wen H. Mixed echo train acquisition displacement encoding with stimulated echoes: an optimized DENSE method for in vivo functional imaging of the human heart. Magn Reson Med 2001;46(3):523-534.
35. Kuijer JP, Hofman MB, Zwanenburg JJ, Marcus JT, van Rossum AC, Heethaar RM. DENSE and HARP: two views on the same technique of phase-based strain imaging. J Magn Reson Imaging 2006;24(6):1432-1438.
36. Kim D, Epstein FH, Gilson WD, Axel L. Increasing the signal-to-noise ratio in DENSE MRI by combining displacement-encoded echoes. Magn Reson Med 2004;52(1):188-192.

37. Spottiswoode BS, Zhong X, Lorenz CH, Mayosi BM, Meintjes EM, Epstein FH. 3D myocardial tissue tracking with slice followed cine DENSE MRI. J Magn Reson Imaging 2008;27(5):1019-1027.
38. Soellinger M, Rutz AK, Kozerke S, Boesiger P. Time-resolved, three-dimensional brain motion measurements using 3D-DENSE. In Proceedings of the 16th Annual Meeting of ISMRM, Berlin, Germany, 2007. p. 3005.
39. Kuijer JPA. Myocardial deformation measured with magnetic resonance tagging [PhD thesis]. Amsterdam: Vrije Universiteit; 2000.
40. Young AA, Cowan BR, Occleshaw CJ, Oxenham HC, Gentles TL. Temporal evolution of left ventricular strain late after repair of coarctation of the aorta using 3D MR tissue tagging. J Cardiovasc Magn Reson 2002;4(2):233-243.
41. van Dockum WG, Kuijer JP, Gotte MJ, Ten Cate FJ, Ten Berg JM, Beek AM, Twisk JW, Marcus JT, Visser CA, van Rossum AC. Septal ablation in hypertrophic obstructive cardiomyopathy improves systolic myocardial function in the lateral (free) wall: a follow-up study using CMR tissue tagging and 3D strain analysis. Eur Heart J 2006;27(23):2833-2839.
42. Bree D, Wollmuth JR, Cupps BP, Krock MD, Howells A, Rogers J, Moazami N, Pasque MK. Low-dose dobutamine tissue-tagged magnetic resonance imaging with 3-dimensional strain analysis allows assessment of myocardial viability in patients with ischemic cardiomyopathy. Circulation 2006;114(1 Suppl):I33-36.
43. Kuijer JP, Marcus JT, Gotte MJ, van Rossum AC, Heethaar RM. Three-dimensional myocardial strain analysis based on short- and long-axis magnetic resonance tagged images using a 1D displacement field. Magn Reson Imaging 2000;18(5):553-564.
44. Declerck J, Denney TS, Ozturk C, O'Dell W, McVeigh ER. Left ventricular motion reconstruction from planar tagged MR images: a comparison. Phys Med Biol 2000;45(6):1611-1632.
45. Pan L, Prince JL, Lima JA, Osman NF. Fast tracking of cardiac motion using 3D-HARP. IEEE Trans Biomed Eng 2005;52(8):1425-1435.
46. Gilson WD, Yang Z, French BA, Epstein FH. Measurement of myocardial mechanics in mice before and after infarction using multislice displacement-encoded MRI with 3D motion encoding. Am J Physiol Heart Circ Physiol 2005;288(3):H1491-1497.
47. Abd-Elmoniem KZ, Stuber M, Osman NF, Prince JL. ZHARP: Three-Dimensional Motion Tracking from a Single Image Plane. In Proceedings of Information Processing in Medical Imaging, Glenwood Springs, CO, USA, 2005. p. 639-651.

48. Ryf S, Baltes C, Boesiger P. High Speed 3D CSPAMM. In Proceedings of the 12th Annual Meeting of ISMRM, Kyoto, Japan, 2004. p. 657.
49. Ryf S, Schwitter J, Spiegel MA, Rutz AK, Luechinger R, Crelier GR, Boesiger P. Accelerated tagging for the assessment of left ventricular myocardial contraction under physical stress. J Cardiovasc Magn Reson 2005;7(4):693-703.
50. Liu YL, Riederer SJ, Rossman PJ, Grimm RC, Debbins JP, Ehman RL. A monitoring, feedback, and triggering system for reproducible breath-hold MR imaging. Magn Reson Med 1993;30(4):507-511.
51. Ryf S, Rutz AK, Boesiger P, Schwitter J. Is post-systolic shortening a reliable indicator of myocardial viability? An MR tagging and late-enhancement study. J Cardiovasc Magn Reson 2006;8(3):445-451.
52. Castillo E, Osman NF, Rosen BD, El-Shehaby I, Pan L, Jerosch-Herold M, Lai S, Bluemke DA, Lima JA. Quantitative assessment of regional myocardial function with MR-tagging in a multi-center study: interobserver and intraobserver agreement of fast strain analysis with Harmonic Phase (HARP) MRI. J Cardiovasc Magn Reson 2005;7(5):783-791.
53. Garot J, Bluemke DA, Osman NF, Rochitte CE, McVeigh ER, Zerhouni EA, Prince JL, Lima JA. Fast determination of regional myocardial strain fields from tagged cardiac images using harmonic phase MRI. Circulation 2000;101(9):981-988.
54. Moore CC, Lugo-Olivieri CH, McVeigh ER, Zerhouni EA. Three-dimensional systolic strain patterns in the normal human left ventricle: characterization with tagged MR imaging. Radiology 2000;214(2):453-466.
55. Kramer CM, Rogers WJ, Theobald TM, Power TP, Petruolo S, Reichek N. Remote noninfarcted region dysfunction soon after first anterior myocardial infarction. A magnetic resonance tagging study. Circulation 1996;94(4):660-666.
56. Zwanenburg JJ, Gotte MJ, Marcus JT, Kuijer JP, Knaapen P, Heethaar RM, van Rossum AC. Propagation of onset and peak time of myocardial shortening in time of myocardial shortening in ischemic versus nonischemic cardiomyopathy: assessment by magnetic resonance imaging myocardial tagging. J Am Coll Cardiol 2005;46(12):2215-2222.
57. Nagel E, Stuber M, Burkhard B, Fischer SE, Scheidegger MB, Boesiger P, Hess OM. Cardiac rotation and relaxation in patients with aortic valve stenosis. Eur Heart J 2000;21(7):582-589.

58. Paetsch I, Foll D, Kaluza A, Luechinger R, Stuber M, Bornstedt A, Wahl A, Fleck E, Nagel E. Magnetic resonance stress tagging in ischemic heart disease. Am J Physiol Heart Circ Physiol 2005;288(6):H2708-2714.

59. Rosen BD, Gerber BL, Edvardsen T, Castillo E, Amado LC, Nasir K, Kraitchman DL, Osman NF, Bluemke DA, Lima JA. Late systolic onset of regional LV relaxation demonstrated in three-dimensional space by MRI tissue tagging. Am J Physiol Heart Circ Physiol 2004;287(4):H1740-1746.

60. Desnick RJ, Ioannou YA, Eng CM. α-Galactosidase A deficiency: Fabry disease. In: Scriver CR, Beaudet AL, Sly WS, Valle D, editors. The Metabolic and Molecular Bases of Inherited Disease. 8th ed. Volume 3. New York: McGraw-Hill; 2001. p 3733-3774.

61. Weidemann F, Breunig F, Beer M, Sandstede J, Turschner O, Voelker W, Ertl G, Knoll A, Wanner C, Strotmann JM. Improvement of cardiac function during enzyme replacement therapy in patients with Fabry disease: a prospective strain rate imaging study. Circulation 2003;108(11):1299-1301.

62. Pieroni M, Chimenti C, Ricci R, Sale P, Russo MA, Frustaci A. Early detection of Fabry cardiomyopathy by tissue Doppler imaging. Circulation 2003;107(15):1978-1984.

63. Rogers WJ, Jr., Shapiro EP, Weiss JL, Buchalter MB, Rademakers FE, Weisfeldt ML, Zerhouni EA. Quantification of and correction for left ventricular systolic long-axis shortening by magnetic resonance tissue tagging and slice isolation. Circulation 1991;84(2):721-731.

64. Ashikaga H, Criscione JC, Omens JH, Covell JW, Ingels NB, Jr. Transmural left ventricular mechanics underlying torsional recoil during relaxation. Am J Physiol Heart Circ Physiol 2004;286(2):H640-647.

65. Alfakih K, Plein S, Thiele H, Jones T, Ridgway JP, Sivananthan MU. Normal human left and right ventricular dimensions for MRI as assessed by turbo gradient echo and steady-state free precession imaging sequences. J Magn Reson Imaging 2003;17(3):323-329.

66. Streeter DD, Jr., Spotnitz HM, Patel DP, Ross J, Jr., Sonnenblick EH. Fiber orientation in the canine left ventricle during diastole and systole. Circ Res 1969;24(3):339-347.

67. Reese TG, Weisskoff RM, Smith RN, Rosen BR, Dinsmore RE, Wedeen VJ. Imaging myocardial fiber architecture in vivo with magnetic resonance. Magn Reson Med 1995;34(6):786-791.

68. Weidemann F, Breunig F, Beer M, Sandstede J, Stork S, Voelker W, Ertl G, Knoll A, Wanner C, Strotmann JM. The variation of morphological and functional cardiac manifestation in Fabry disease: potential implications for the time course of the disease. Eur Heart J 2005;26(12):1221-1227.
69. Delhaas T, Kotte J, van der Toorn A, Snoep G, Prinzen FW, Arts T. Increase in left ventricular torsion-to-shortening ratio in children with valvular aortic stenosis. Magn Reson Med 2004;51(1):135-139.
70. Oxenham HC, Young AA, Cowan BR, Gentles TL, Occleshaw CJ, Fonseca CG, Doughty RN, Sharpe N. Age-related changes in myocardial relaxation using three-dimensional tagged magnetic resonance imaging. J Cardiovasc Magn Reson 2003;5(3):421-430.
71. Moon JC, Sheppard M, Reed E, Lee P, Elliott PM, Pennell DJ. The histological basis of late gadolinium enhancement cardiovascular magnetic resonance in a patient with Anderson-Fabry disease. J Cardiovasc Magn Reson 2006;8(3):479-482.
72. Moon JC, Sachdev B, Elkington AG, McKenna WJ, Mehta A, Pennell DJ, Leed PJ, Elliott PM. Gadolinium enhanced cardiovascular magnetic resonance in Anderson-Fabry disease. Evidence for a disease specific abnormality of the myocardial interstitium. Eur Heart J 2003;24(23):2151-2155.
73. Barbey F, Brakch N, Linhart A, Rosenblatt-Velin N, Jeanrenaud X, Qanadli S, Steinmann B, Burnier M, Palecek T, Bultas J, Hayoz D. Cardiac and vascular hypertrophy in Fabry disease: evidence for a new mechanism independent of blood pressure and glycosphingolipid deposition. Arterioscler Thromb Vasc Biol 2006;26(4):839-844.
74. Smalling RW, Ekas RD, Felli PR, Binion L, Desmond J. Reciprocal functional interaction of adjacent myocardial segments during regional ischemia: an intraventricular loading phenomenon affecting apparent regional contractile function in the intact heart. J Am Coll Cardiol 1986;7(6):1335-1346.
75. Vernooy K, Verbeek XA, Peschar M, Crijns HJ, Arts T, Cornelussen RN, Prinzen FW. Left bundle branch block induces ventricular remodelling and functional septal hypoperfusion. Eur Heart J 2005;26(1):91-98.
76. Rosenbush S, Ruggie N, Turner D, von Behren P, Denes P, Fordham E, Groch M, Messer J. Sequence and timing of ventricular wall motion in patients with bundle branch block. Circulation 19882;66:1113-1119.

77. Vardas P, Auricchio A, Blanc J, Daubert J, Drexler H, Ector H, Gasparini M, Linde C, Bello F, Oto A, Sutton R, Trusz-Gluza M. Guidelines for cardiac pating and cardiac resynchronization therapy of the European Society of Cardiology. Europace 2007;9:959-998.

78. Bax JJ, Bleeker GB, Marwick TH, Molhoek SG, Boersma E, Steendijk P, van der Wall EE, Schalij MJ. Left ventricular dyssynchrony predicts response and prognosis after cardiac resynchronization therapy. J Am Coll Cardiol 2004;44(9):1834-1840.

79. Sogaard P, Egeblad H, Kim WY, Jensen HK, Pedersen AK, Kristensen BO, Mortensen PT. Tissue Doppler imaging predicts improved systolic performance and reversed left ventricular remodeling during long-term cardiac resynchronization therapy. J Am Coll Cardiol 2002;40(4):723-730.

80. Chung ES, Leon AR, Tavazzi L, Sun JP, Nihoyannopoulos P, Merlino J, Abraham WT, Ghio S, Leclercq C, Bax JJ, Yu CM, Gorcsan J, 3rd, St John Sutton M, De Sutter J, Murillo J. Results of the Predictors of Response to CRT (PROSPECT) trial. Circulation 2008;117(20):2608-2616.

81. Tecelao SR, Zwanenburg JJ, Kuijer JP, de Cock CC, Germans T, van Rossum AC, Marcus JT. Quantitative comparison of 2D and 3D circumferential strain using MRI tagging in normal and LBBB hearts. Magn Reson Med 2007;57(3):485-493.

82. Nelson GS, Curry CW, Wyman BT, Kramer A, Declerck J, Talbot M, Douglas MR, Berger RD, McVeigh ER, Kass DA. Predictors of systolic augmentation from left ventricular preexcitation in patients with dilated cardiomyopathy and intraventricular conduction delay. Circulation 2000;101(23):2703-2709.

83. Helm RH, Leclercq C, Faris OP, Ozturk C, McVeigh E, Lardo AC, Kass DA. Cardiac dyssynchrony analysis using circumferential versus longitudinal strain: implications for assessing cardiac resynchronization. Circulation 2005;111(21):2760-2767.

84. Rutz AK, Ryf S, Plein S, Boesiger P, Kozerke S. Accelerated whole-heart 3D CSPAMM for myocardial motion quantification. Magn Reson Med 2008;59(4):755-763.

85. Kim RJ, Wu E, Rafael A, Chen EL, Parker MA, Simonetti O, Klocke FJ, Bonow RO, Judd RM. The use of contrast-enhanced magnetic resonance imaging to identify reversible myocardial dysfunction. N Engl J Med 2000;343(20):1445-1453.

86. Knuesel PR, Nanz D, Wyss C, Buechi M, Kaufmann PA, von Schulthess GK, Luscher TF, Schwitter J. Characterization of dysfunctional myocardium by positron emission

tomography and magnetic resonance: relation to functional outcome after revascularization. Circulation 2003;108(9):1095-1100.

87. Leclercq C, Faris O, Tunin R, Johnson J, Kato R, Evans F, Spinelli J, Halperin H, McVeigh E, Kass DA. Systolic improvement and mechanical resynchronization does not require electrical synchrony in the dilated failing heart with left bundle-branch block. Circulation 2002;106(14):1760-1763.
88. Russel IK, Zwanenburg JJ, Germans T, Marcus JT, Allaart CP, de Cock CC, Gotte MJ, van Rossum AC. Mechanical dyssynchrony or myocardial shortening as MRI predictor of response to biventricular pacing? J Magn Reson Imaging 2007;26(6):1452-1460.
89. Byrne MJ, Helm RH, Daya S, Osman NF, Halperin HR, Berger RD, Kass DA, Lardo AC. Diminished left ventricular dyssynchrony and impact of resynchronization in failing hearts with right versus left bundle branch block. J Am Coll Cardiol 2007;50(15):1484-1490.
90. Ypenburg C, Schalij MJ, Bleeker GB, Steendijk P, Boersma E, Dibbets-Schneider P, Stokkel MP, van der Wall EE, Bax JJ. Extent of viability to predict response to cardiac resynchronization therapy in ischemic heart failure patients. J Nucl Med 2006;47(10):1565-1570.
91. Wang Y, Rossman PJ, Grimm RC, Riederer SJ, Ehman RL. Navigator-echo-based real-time respiratory gating and triggering for reduction of respiration effects in three-dimensional coronary MR angiography. Radiology 1996;198(1):55-60.
92. Bland JM, Altman DG. Statistical methods for assessing agreement between two methods of clinical measurement. Lancet 1986;1(8476):307-310.
93. Helm RH, Byrne M, Helm PA, Daya SK, Osman NF, Tunin R, Halperin HR, Berger RD, Kass DA, Lardo AC. Three-dimensional mapping of optimal left ventricular pacing site for cardiac resynchronization. Circulation 2007;115(8):953-961.
94. Wyman BT, Hunter WC, Prinzen FW, Faris OP, McVeigh ER. Effects of single- and biventricular pacing on temporal and spatial dynamics of ventricular contraction. Am J Physiol Heart Circ Physiol 2002;282(1):H372-379.
95. Kawaguchi M, Murabayashi T, Fetics BJ, Nelson GS, Samejima H, Nevo E, Kass DA. Quantitation of basal dyssynchrony and acute resynchronization from left or biventricular pacing by novel echo-contrast variability imaging. J Am Coll Cardiol 2002;39(12):2052-2058.
96. van Rugge FP, van der Wall EE, Spanjersberg SJ, de Roos A, Matheijssen NA, Zwinderman AH, van Dijkman PR, Reiber JH, Bruschke AV. Magnetic resonance

imaging during dobutamine stress for detection and localization of coronary artery disease. Quantitative wall motion analysis using a modification of the centerline method. Circulation 1994;90(1):127-138.

97. de Roos A, van der Wall EE, Bruschke AV, van Voorthuisen AE. Magnetic resonance imaging in the diagnosis and evaluation of myocardial infarction. Magn Reson Q 1991;7(3):191-207.

Danke

Die vorliegende Arbeit ist das Ergebnis von fast fünf Jahren Forschung und wissenschaftlicher Zusammenarbeit am Institut für Biomedizinische Technik der Universität und der ETH Zürich. Ich möchte allen herzlich danken, die zum Gelingen dieser Arbeit beigetragen haben. Ein spezielles Dankeschön für die tolle Zusammenarbeit und die gute Zeit geht an:

- Prof. P. Bösiger, der mir die Arbeit in diesem inspirierenden und effizienten Arbeitsumfeld ermöglicht hat. Sein Vertrauen sowie das optimale Arbeitsklima in der MR-Gruppe bildeten die Grundlagen dieser Arbeit.

- Prof. M. Stuber, für das Korreferat.

- Sebastian Kozerke, dem Chef vom Kardiokreisli, für die Betreuung meiner Doktorarbeit. Seine Antworten auf fast alle Fragen sowie seine Hilfe zu jeder Tages- und Nachtzeit haben wesentlich zum Gelingen dieser Arbeit beigetragen.

- Salome Ryf, die mich in die Geheimnisse des Taggings eingeweiht hat und von der ich einiges übernehmen konnte, was ich sonst mühsam selber hätte erarbeiten müssen.

- Gérard Crelier, den Vater von TagTrack, für seine Auswerteprogramme, geschrieben in von mir nie erreichtem Programmierstil.

- Michaela Soellinger und Christof Baltes, für die vielen Diskussionen über MR-Sequenzen und die gute gemeinsame Zeit im Büro.

- Roger Lüchinger, für alles, aber vor allem für seine sportliche Begeisterung.

- Dieter Meier, für den Support im MR-Zentrum.

- Marco Piccirelli, für die interessanten Augen-Tagging Projekte und für Picci-Pasta.

- Jürg Schwitter, Robert Manka, Sven Plein und Christoph Juli, für ihre Offenheit für neue Tagging-Methoden und die Unterstützung bei den Patientenstudien.

- Die Kardiogruppe, für die Lösung vieler Probleme und die angenehme Zeit bei und neben der Arbeit. Herz-lichen Dank an: Carsten Schirra, Jochen von Spiczak, Martin Bührer, Mike Schär, Rudolf Fischer, Urs Gamper und Viton Vitanis.

- Die gesamte MR-Gruppe, für die gute und motivierende Arbeitsatmosphäre und die jederzeit gute Stimmung, welche meine Doktoratszeit nicht nur während der Arbeit angenehm machte.

- Franziska, für ihre Geduld und Unterstützung, sowie die wunderbare Zeit neben der Arbeit.

- Meine Eltern, für ihre bedingungslose Unterstützung während meiner gesamten Ausbildungszeit.

Curriculum Vitae

I was born on March 14th 1977 as son of Irène and Peter Rutz. I grew up in St.Gallen and Zufikon AG, where I attended primary school. In summer 1997 I graduated from the Kantonsschule Wohlen with Matura type B.

In 1997 I started my studies in Electrical Engineering at the *Swiss Federal Institute of Technology* (ETH) in Zurich with specialization in Biomedical Engineering and Signal Processing. As part of my studies, I did an internship at *Kontron Medical* in Basel and at *Pacific E.N.G.* in Bangkok, Thailand. In spring 2003 I graduated after having completed my diploma thesis entitled "*Transcutaneous Signal and Energy Transmission for an Implantable Hearing Aid System*" carried out at *Chalmers University of Technology* in Gothenburg, Sweden.

Since August 2003 I am working as a teaching and research assistant at the *Institute for Biomedical Engineering* of the *University and ETH Zürich* in the Biophysics group of Prof. P. Bösiger. My research was focused on cardiac magnetic resonance imaging.